Spectro-astrometry as a Tool for Detecting Planets in Transitional Disks

by

Eoin Cahill

Faculty of Science and Engineering
Department of Experimental Physics

Head of Department:
Prof. Anthony Murphy

Research Supervisor:
Dr. Emma Whelan

May 2019

Declaration of Authorship

I, Eoin Cahill, declare that this thesis titled, 'Spectro-astrometry as a Tool for Detecting Planets in Transitional Disks' and the work presented in it are my own. I confirm that:

- This work was done wholly or mainly while in candidature for a research degree at this University.

- Where any part of this thesis has previously been submitted for a degree or any other qualification at this University or any other institution, this has been clearly stated.

- Where I have consulted the published work of others, this is always clearly attributed.

- Where I have quoted from the work of others, the source is always given. With the exception of such quotations, this thesis is entirely my own work.

- I have acknowledged all main sources of help.

- Where the thesis is based on work done by myself jointly with others, I have made clear exactly what was done by others and what I have contributed myself.

Signed:

_____

Date:

_____

Summary

The goal of understanding how our solar system formed has been a long standing one. We have already answered the question "is our solar system unique?" by detecting an ever-growing population of extra solar planets orbiting stars of many different sizes and temperatures. It is much easier to detect a large planet that orbits close to its star as opposed to a smaller, more distant one. This led to the discovery of many *Hot-Jupiters* in the initial stages of exoplanet detection, but increased efficiency in both ground and space-based detection techniques expanded the catalogue of exoplanets to include a truly diverse range. In order to understand how these planets are formed we need to investigate planet formation in the earliest stages. Traditional techniques like transit photometry and the RV method are difficult to apply to these objects due to their instability, and direct imaging remains difficult to perform. Here we investigate the possibility of using spectro-astrometry to detect planets around young stars. UVES spectra of T Cha were obtained with a spectro-astrometric study in mind, and the technique is also tested by applying it to UVES spectra of HD 142527, a young Herbig Ae/Be star with a known brown dwarf companion. Chapter 1 covers an introduction into the topic of star and planet formation, and describes the specific type of star this project intends to probe: Transitional disk objects. The main four exoplanet detection techniques currently in use are described, and a discussion of whether they can be used for detection of exoplanets still in formation accompanies each. Chapter 2 then describes the technique of spectro-astrometry as it has been used before. We also look into some of the advantages and disadvantages of using it and how the problem of planet detection around young stars could be overcome via spectro-astrometric analysis. In Chapter 3, details of the instrument used for our observations is provided. A description and discussion of the data reduction process then follows. Several artefacts that were found in the course of this project are also analysed. Chapter 4 covers results of our analysis on the T Tauri variable type star, T Chamaeleontis. The aim of the study is to determine if it is possible to accurately detect the Hα emission from the hypothesised exoplanet T Chamaeleontis b. No detection was proven, but limits are placed on the $\dot{M}_{acc}$ of the exoplanet and the detection limit using spectro-astrometry. In Chapter 5, a bridge between binary detection (of which spectro-astrometry is well established) and exoplanet detection (of which has not been proven) is presented in the analysis of HD 142527. HD 142527 is orbited by a 0.13 M$_\odot$ Very Low-Mass star, which is around 100 times larger than the expected size of T Chamaeleontis b. Evidence for a detection is presented and finally discussed. Chapter 6 summarises all results and conclusions that were found throughout this thesis, and a discussion on the efficacy of spectro-astrometry as a detection technique for exoplanets around YSOs.

Acknowledgements

I would like to begin by thanking everybody in the Experimental Physics department. As a whole it is this type of friendly and helpful environment that makes the long days and late nights bearable, especially towards the end of this thesis. My supervisor, Dr. Emma Whelan, has been indefatigable in her level of patience and assistance, even with a new addition to her family in baby Aoibh. I sincerely thank you for all your support, and for putting up with me for these two years!

I would also like to thank Ms. Grainne Roche for her assistance in pretty much all areas, and the banter we have shared will not be forgotten. I would also like to thank Mr. John Kelly for assistance with all things computer-based, and for hooking me up with the second hard-drive that was so badly needed. As Linux was the main OS used in this project, thanks must be given to Dr. Marcin Gradziel for sharing his seemingly limitless knowledge, and for correcting the many errors that occurred as I began to learn the ins and outs of this operating system. He was also a great man for knowing a good book to read, and pointed me to some of my now favourite series.

Where would a postgraduate be without a group of piers to help share the highs and lows? Thankfully, I have no idea. Whether it be late night D&D sessions, evening pints, a casual cycle to Galway, chess games over lunch or just a cigarette out on the balcony, the Experimental Physics department is blessed in having such a good group of postgraduates, both now and when I started. A special shout out to Rory Sheridan, whose constant bad puns could liven up any situation, no matter how cringeworthy they were. Thanks to Dr. Sharon Rourke and Dr. Eimanté Kalinauskeité for the chats and the smoke breaks respectively. Joe Brennan has also been key in retaining my sanity through constant slagging back and forth, and his knowledge of memes is second to none. David Burke must also get a mention, how one man can love cats so much ill never fully comprehend. Thanks to my roommate Aisling Murphy for discussions on all matters star related, and some good pointers for Rome 2. Also thanks to - Adam Byrne, Mark Deegan, James 'Jimmy' Murphy, Julianne Kealy, Donnacha Gayer, Anthony Donohoe, Melissa Dunne, Mike Brown, Daithi Byrne, Andrew Wilson and Bastien Rouzé.

Finally, but most importantly, thanks to Angela and Noel for firstly questioning and then supporting my decision to leave my job and pursue this project. Regardless of where I go after this, I will have quelled that little voice in my head saying 'what if..?'.

Thanks do not encompass the gratitude I feel to you both, and I was blessed to have two people so supportive.

List of Figures

List of Tables

For friends, family and science

Contents

Chapter 1

An Introduction to Planet Formation around Young Stellar Objects

Since the acceptance of the heliocentric model of our solar system and its place in the known Universe, the question of whether the vast amount of stars visible in the night sky also harbour planets like Earth, and whether these planets could support life, has been ever present in the minds of scientists. This acceptance that the Earth is not *special*, led to the realization that other planets may also have the necessary components for life to flourish. This is compounded by the Italian philosopher Giordano Bruno (1548-1600), who argued that;

"It is shewn clearly that there is no accident here which may not be expected also on those other worlds; just as if we consider well we must recognize that naught there can be seen from here which cannot also be seen here from there."

NASA currently estimate that around half of all stars in the Milky Way contain at least one planetary body, although we are only detecting less than one percent of these. This has been steadily increasing as more detection techniques are perfected, and the efficiency of telescopes both on the ground and in space increases.

The evolution of stars has been well documented since the beginning of the 20th century with the development of the Hertzsprung-Russell (HR) diagram, which shows the link between absolute magnitude and stellar classification, or luminosities and effective temperatures. This was followed by the addition of the Henyey and Hayashi tracks showing the stellar evolution tracks for pre-main sequence (PMS) stars of different masses. However, although exoplanet research has exploded in recent years to be a

major area of study for all fields of natural science (astrochemistry, astrobiology etc.), the mechanics of planet formation itself is still a relatively new field of investigation, with several theories currently vying for acceptance.

The development and validation of these theories, discussed in Section 1.1.3, is dependant on discovering as diverse a sample of exoplanets as possible. This dataset should also contain exoplanets at as early an age as possible in order to constrain the mechanics behind their formation.

This thesis aims to expand on the topic of protoplanetary detection. More specifically, the efficacy of a technique called spectro-astrometry in the detection of a likely protoplanet, T Chamaeleontis b, around the T Tauri Star, T Chamaeleontis (hereafter T Cha). Spectro-astrometry is simply a combination of spectroscopy and astrometry. Instead of measuring only precise positions of the stars centre of mass, measurements of the centre of emission are taken at multiple wavelengths of light, and any offset from this centre can reveal information about unresolved binaries or jets and outflows.

1.1 The formation of planets around Young Stellar Objects

Typically, exoplanet detection techniques are aimed at main sequence stars due to their intrinsic stability and slow rotational velocity. These stars will not cover up the relatively small effects one or multiple exoplanets will impose on the parent star. This lowers the chance of false positives in many current techniques, but also prevents investigation of the earliest stages of planet formation, when the star is still in a state of turbulence. For these reasons detection of exoplanets around Young Stellar Objects (YSOs) has become an increasingly popular area of astronomy.

Until recently, our understanding of planet formation stemmed from the only observable example, our own Solar System. Formation theories had to work backwards from the current distribution of terrestrial and giant planets back to a circumstellar disk where the planets would have been formed. Immanuel Kant (1755) and Pierre-Simon Lapace (1776) are credited with the first papers written about a flat circumstellar disk in which planet formation takes place, and laid the groundwork for the Solar Nebula Disk Model which is still the main theory explaining the formation of the terrestrial planets. The topic itself is regularly compounded in the *Protostars and Planets* books, currently at volume *VI* (Beuther et al. 1985).

In this section we will briefly review the processes behind planet formation and discuss the period of planetary evolution we are trying to observe with spectro-astrometry.

1.1.1 Star formation - Our Current Understanding

The formation of stars is known to take place within clouds of gas and dust spread about the interstellar medium (ISM). These molecular clouds come in both Giant (GMC) and Small (SMC) formations, and are known as *Stellar Nurseries* once star formation is occurring. Generally, most star formation physics is derived for GMCs but is given as a good approximation of SMCs also. When considering astronomical problems relating to molecular clouds, it is useful to assume that they act under the ideal gas law at constant temperature. We can also assume that the constituents of the molecular cloud are at constant temperature and chemical composition. This is known as the isothermal assumption. This gives us an ideal gas law for molecular hydrogen given by

$$\frac{P}{\rho} = \frac{kT}{\mu m_H} = a_0^2 = constant, \tag{1.1}$$

where P is the pressure, ρ is the density, k is the Boltzmann constant, T is the temperature, μ is the mean molecular weight, m_H is the mass of a hydrogen atom and a_0 is the isothermal speed of sound of the gas at temperature T. Further considerations include the fluid dynamics of the molecular cloud. The two types of fluid dynamics considered are the Eulerian and the Lagrangian models. The Eulerian model is a fixed set of coordinates in space through which the molecular cloud is flowing, and the Lagrangian model considers a set of co-moving coordinates fixed around a single particle. When these models are fully derived (see derivations in Ward-Thompson & Whitworth (2011)) and the gravitational field is included, what remains is an offshoot of Euler's equation:

$$\frac{\delta \mathbf{v}}{\delta t} + (\mathbf{v}.\Delta)\mathbf{v} + \frac{\delta P}{\rho} - \mathbf{g} = 0. \tag{1.2}$$

The well-established Jeans length and corresponding mass functions act as a good approximation for a static cloud of uniform composition (Jeans 1902), but in nature this homogeneity is not observed. Molecular clouds often show supersonic motions, and vary in temperature, density and velocity from micro- to macroscopic scales, best seen in the filamentary structures that are seen throughout molecular clouds, shown in Figure 1.1. Within the core of a GMC, the temperature can be taken as ~ 10 K, with
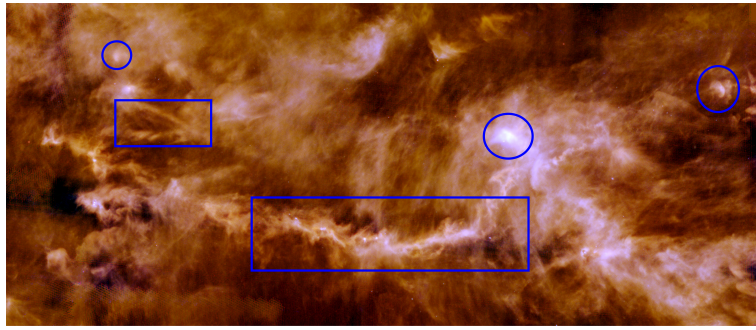
FIGURE 1.1: Image taken from Palmeirim et al. (2013) showing star formation in the Taurus Molecular Cloud. Two instances of filaments and cores are highlighted by rectangles and circles respectively. Images such as these taken from the Herschel space observatory show the ubiquitous nature of filaments in molecular clouds and their role in star formation.

a density ρ of $\sim 3 \times 10^{-17}$ kg m^{-3}. This gives a Jeans mass of ~ 7 M$_\odot$. Typical cores of GMCs can have masses of 10 M$_\odot$, making them gravitationally unstable against collapse.

A more accurate general description for a cloud in equilibrium is given by the Virial Theorem (Clausius 1870; Collins 1978). It states that twice the kinetic energy of the gas particles must equal the gravitational potential energy in order for the cloud to be in equilibrium, which is indeed a condition but not the only factor. The virial theorem also introduces the concept of a virial mass. This is the mass which a cloud must be close to in order to be in equilibrium. If it exceeds the virial mass it will begin core collapse unless supported by some other mechanism. Magnetic fields are also thought to be regulating star formation rates by supporting molecular clouds against collapse. Free-fall lifetimes of cores (100,00 years) are generally one order of magnitude less than statistically inferred values (Mouschovias 1989).

The initial stages of cloud collapse occur approximately isothermally. This increase in density will lower the Jeans mass, allowing smaller clumps of gas and dust to splinter into local cores of smaller masses than the initial cloud. This is known as *hierarchical fragmentation* (Shu et al. 1987) and will continue until the compression heating starts to overtake the radiative cooling rate and the temperature begins to rise. The conservation of angular momentum should prevent full core collapse, but the twisting of the local magnetic field lines and their connection to the Galactic Magnetic Field act as a torsion brake, removing excess angular momentum and allowing the core to begin collapsing, known as a pre-stellar core. Isothermal collapse continues until there is a hydrostatic core at its centre and a gaseous envelope surrounding the now formed *protostar*. Gravitational potential energy is still being freely radiated away providing most of the luminosity, but as the density increases, it becomes less efficient at radiating this
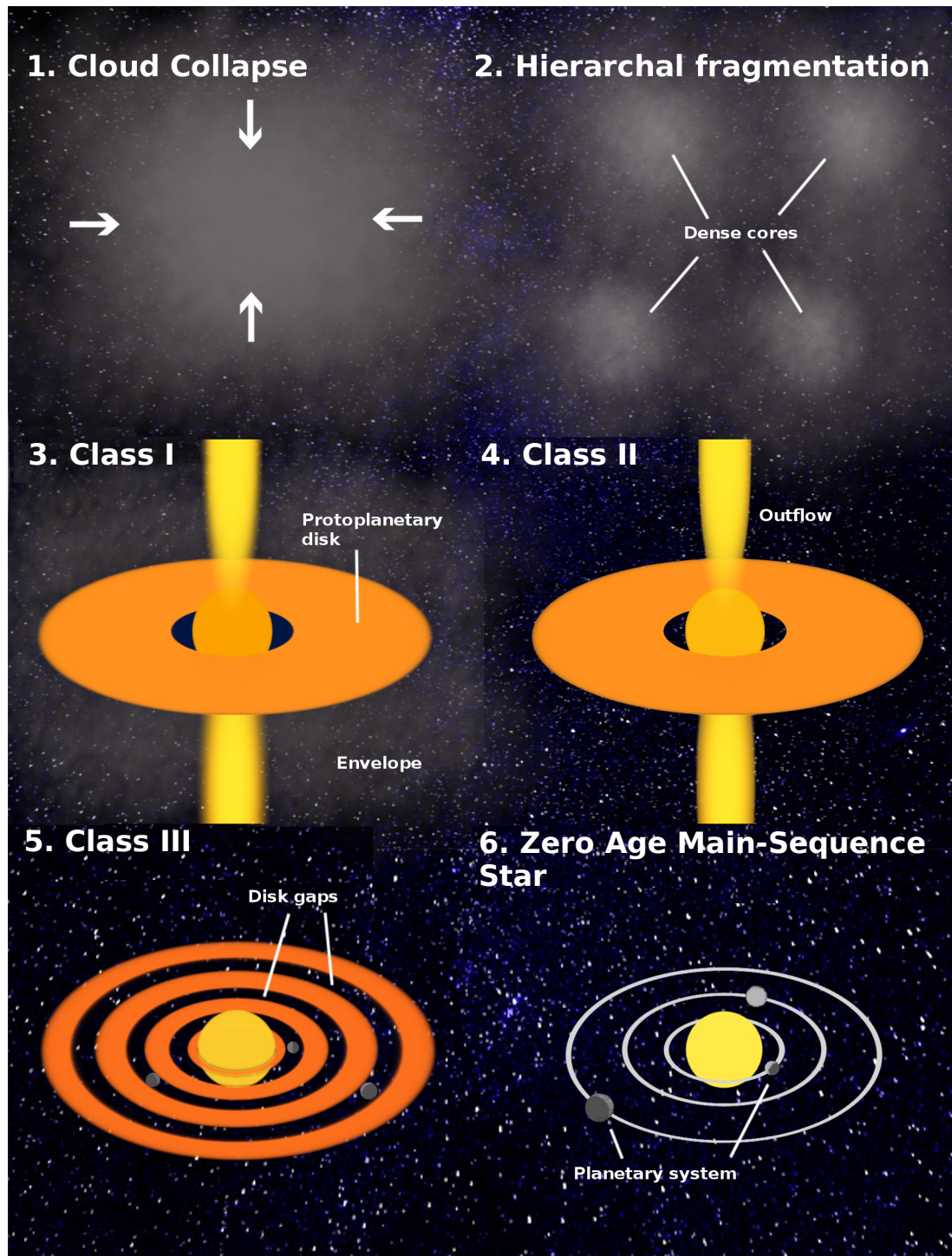
FIGURE 1.2: Diagram showing the different stages of YSO evolution. Class 0 objects are dense hydrostatic cores that form after hierarchal fragmentation.

energy away and the luminosity decreases with the radius. This decrease in luminosity at constant temperature is known as the (*Hayashi Track*), and is represented by a vertical descent along the HR diagram (Hayashi 1961), as shown in Figure 1.3. This process follows the accretion phase, where the star will accumulate most of its final
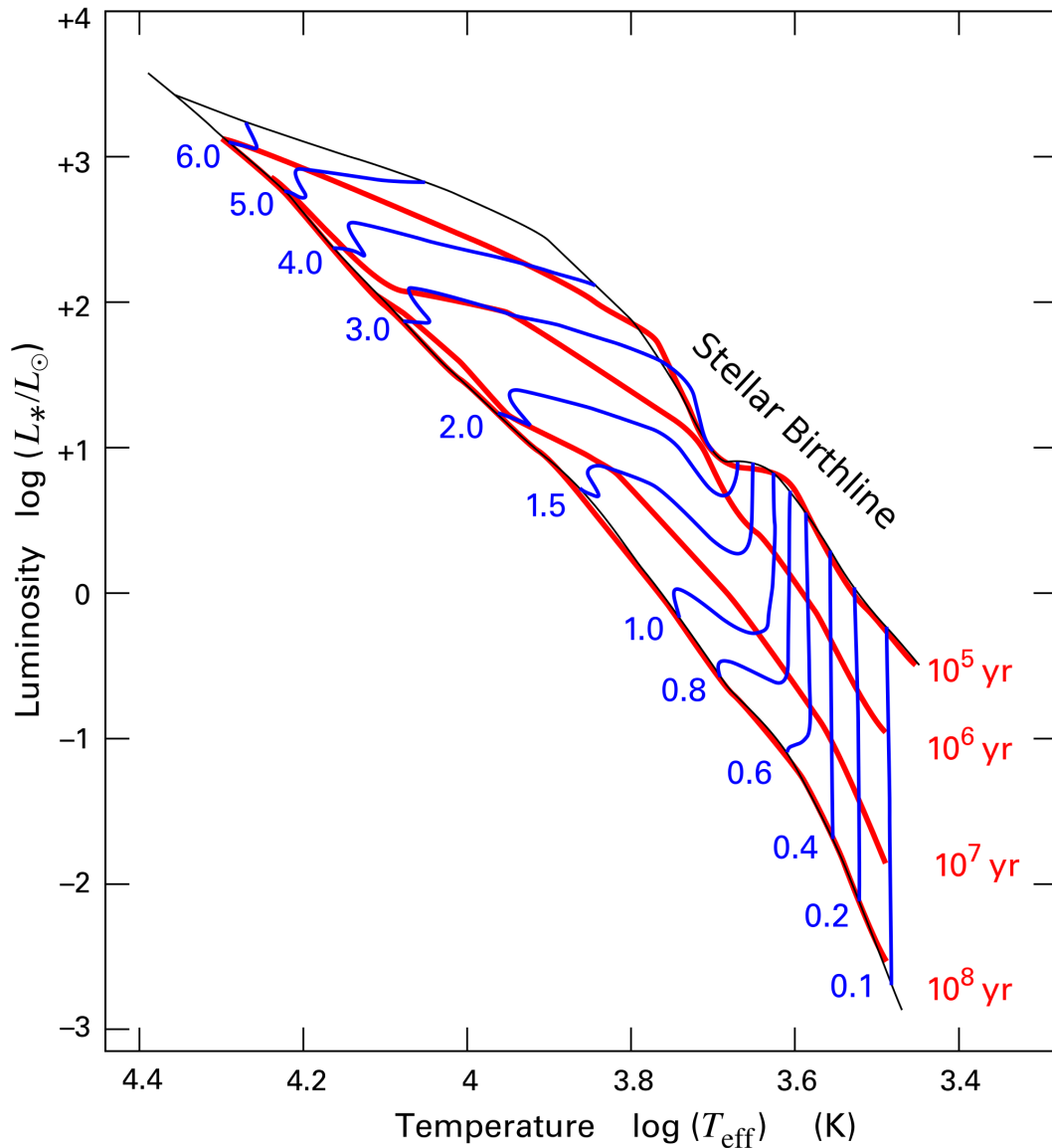
FIGURE 1.3: Diagram showing the evolutionary tracks for PMS stars. The numbers in blue represent the final mass of the star as it reaches the Zero-Age Main-Sequence (ZAMS) in solar masses, and the red numbers are various isochrones (constant age). The stellar birthline represents when a protostar has emerged from its dust envelope and is detectable through observation. Image taken from Palla & Francesco (2012).

mass. The star begins to heat up, and outflows occur to carry away excess angular momentum. Once the temperature has increased sufficiently, the star will switch from radiative to convective heat transfer. The gravitational potential energy is still supplying luminosity for the PMS star, but the luminosity and temperature are now both increasing, causing the star to move horizontally towards the main sequence track of the HR diagram, along the *Henyey Track* (Henyey et al. 1955). Figure 1.2 illustrates the stages described above.

Having described the PMS evolution of stars with a mass of less than 8 $M_\odot$, the classification system of these objects is now described. This was developed by observational properties, characterised by their spectral index, α (Andre & Montmerle 1994; Lada 1987), which is calculated in the wavelength range of 2.2 - 20 μm. The spectral index is given as:

$$\alpha = \frac{\delta log(\lambda * F_\lambda)}{\delta log(\lambda)},\tag{1.3}$$

where λ is wavelength and F_λ is flux density. To date, four classes of YSOs have been defined, and they are as follows:

- Class 0:

  The stars have a hydrostatic core, and are undetectable at $\lambda < 2.2$ - 20 μm. They have a spectral energy distribution (SED) similar to that of a blackbody at a temperature $T \sim 15$ - 30 K. Typical ages are roughly 10^4 yr

- Class I: $\alpha > 0$

  The stars now have a circumstellar disk as well as an envelope, and most of their luminosity stems from accretion. They are thought to have an age of around 1 - 2×10^5 yr.

- Class II: -1.5 $< \alpha < 0$

  Also known as Classical T Tauri Stars (CTTS). They have retained their circumstellar disk, but the envelopes have settled into the midplane or been accreted. They exhibit strong emission lines caused by continuing accretion from the disk. Typical ages are a few to several Myr.

- Class III: $\alpha <$ -1.5

  Also known as weak-line T Tauri Stars (WTTS), as they have weaker emission lines in the optical, which indicates there is less accretion. This is thought to be due to their later stage in YSO evolution. Typical ages are tens of Myr.

With this classification defined, the next step for this thesis is to introduce a subset of class II T Tauri stars: transitional disk objects (TDs).

1.1.2 Transitional Disk Objects

TDs are a subset of T Tauri stars (TTS) that have begun the transition from a star with a complete circumstellar disk to one with a cleared central zone and an outer
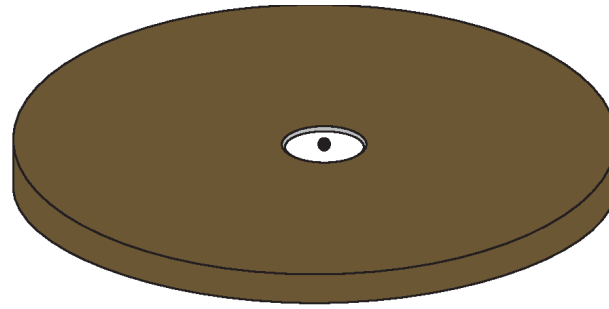
Full Disk
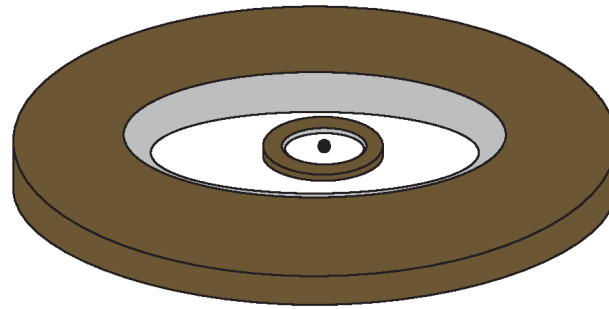
Pre-Transitional Disk
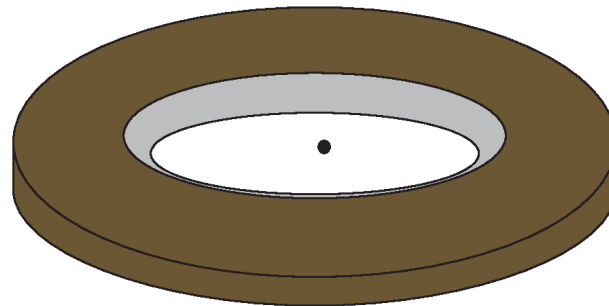
Transitional Disk

FIGURE 1.4: Figure taken from Espaillat et al. (2014) showing the 3 stages of disk evolution. A full disk shows emission deficits at all wavelengths, a pre-transitional disk has a deficit in the mid-IR while a TD has both a mid- and near-IR deficit in its SED.

disk. They were first identified by Strom et al. (1989) via their SED which shows little near-infrared (0.7 - 1.4μm) excess, but strong excess in the mid-IR (1.4 - 15μm) and far-IR (15 - 1000μm) bands. Espaillat et al. (2014) conducted a study on the population and classification of TDs, identifying a stage known as pre-transitional disks, which are thought to be likely candidates for planet formation at its earliest detectable stage. This occurs as the disk, generally following a mass ratio with the parent of $M_{dust}/M_{star} = 3 \times 10^{-5}$ (Bergin & Williams 2018), surrounding Class II objects begins to be cleared by both accretion onto the main star and protoplanetary

objects. It is generally thought that progression from a full disk to a main sequence star with no gas or dust takes on the order of 10 Myr (Strom et al. 1993), with an uncertainty of one order of magnitude. Once a star has reached the main sequence, planets have already been formed, and so the mechanics behind formation can only be inferred. Figure 1.4 shows the evolution of a Class II object from a full disk to a TD. The two methods currently accepted for the clearing of dust and gas from the circumstellar disks are via planet formation and photoevaporation (Ercolano & Pascucci 2017; Pascucci & Sterzik 2009). The process of planet formation should leave accretion tracers which enable indirect detection of planetary mass companions (Uyama et al. 2017). Figure 1.5 is an ALMA image of TW Hya taken from Andrews et al. (2016), which is a transitional disk (TD) object, first classified as such by Salyk et al. (2007).

Another way of validating the classification of Class II and III objects is by their mass accretion rate ($\dot{M}_{acc}$), which is intrinsically linked to the evolution of their circumstellar disks. There have been many such studies in recent years (Alcala et al. 2017; Manara et al. 2012; Rigliaco et al. 2012; Whelan et al. 2015; Zhu 2015). Manara et al. (2016) estimates the $\dot{M}_{acc}$ of a sample of YSOs in the Chamaeleon I star-forming region, and the spread of accretion rates is 2.5×10^{-7} M$_{\odot}$ yr^{-1} to 2×10^{-11} M$_{\odot}$ yr^{-1}. There is still some uncertainty inherent in these results, as they are dependant on age, distance, spectral type and circumstellar extinction. Several ways to calculate the $\dot{M}_{acc}$ have been derived, with one of the first being a relationship between it and the width of the Hα line at 10% intensity (Natta et al. 2004), but due to the intrinsic variability of the line it has been found that the most accurate procedure is to use as many lines as possible (Rigliaco et al. 2010). This ensures that variability in any single accretion indicator will not affect the final estimation of the $\dot{M}_{acc}$.

Classical T Tauri stars are often accompanied by outflows or jets (Whelan 2014), but many have finished this stage in their evolution by the time they become Class II objects, signified by a lower $\dot{M}_{acc}$ due to the accumulation and dissipation of the circumstellar disk (Ercolano 2014). Nisini et al. (2017) investigated the connection between jets, winds and accretion in TTSs, using the [OI]λ 6300 Å line as a tracer. They find a similar $\dot{M}_{acc}$ range as Manara et al. (2016), and discovered that over 77% of TTSs have a low velocity component (LVC) associated with stellar winds, while 30% also have a high velocity component (HVC) associated with jets.
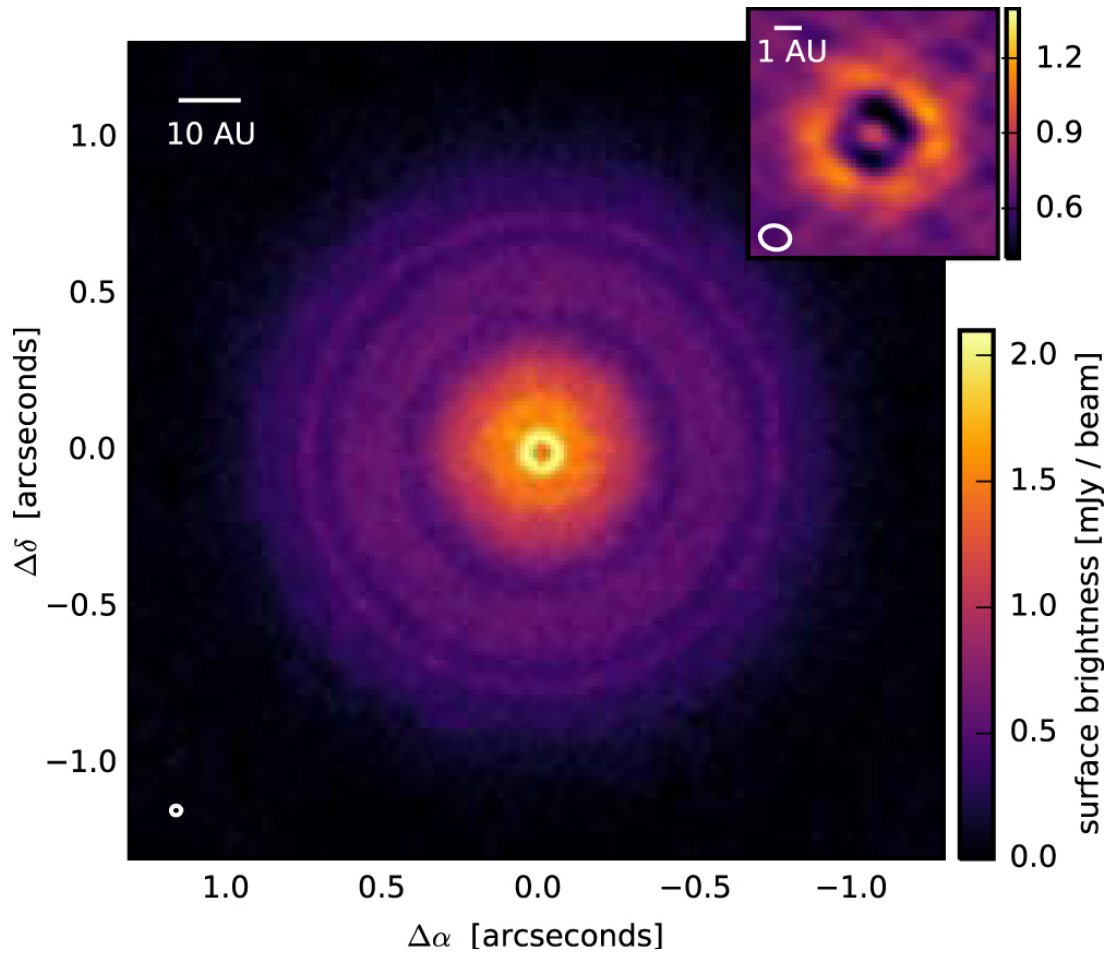
FIGURE 1.5: Image taken from Andrews et al. (2016) showing the 0.8 mm continuum emission of the TD object TW Hya with a zoom-in showing the gap in the inner disk region (as viewed by ALMA).

1.1.3 Planetesimals - Exoplanets in their Infancy

It is generally accepted that the evolution of dust into planetesimals heralds the earliest stages of planet formation, for both the cores of the outer gas and ice giant planets and the inner rocky planets themselves. This growth of dust and gas from a collection of particles to an object with a diameter of 10 - 1000 km is generally thought to be a two-stage process. First, particles collide through Brownian motion and clump together by contact force. Barriers in growth occur at a radius of approximately 1 cm, but collisional mass-transfer or low density coagulation are two theories put forward to overcome the radial drift and inefficient sticking problems of particle growth (Johansen et al. 2014). This continues until the clumps have coagulated into an object with a diameter of 1 km. At this stage, the depth of its gravitational potential well has increased enough to allow capture of other accreting objects and several dominant planetary embryos exist, each carving out their own radial surroundings. This leads to the gaps in a protoplanetary disk as seen in Figure 1.6 (Lissauer 1993). Runaway

accretion follows this stage, and the inner terrestrial planets are formed within the frost line of the disk (Ida & Nakazawa 1989). Beyond the frost line, the abundance of ice means that the cores are much heavier than their dusty counterparts, and grow to around 10 $M_\oplus$. At this point they have a high enough gravitational well to accrete gas from the disk, and they form into gas giants.

Figure 1.6 shows direct observation of a protoplanetary disk around the T Tauri star HL Tau, thought to be only 1 Myr old. In the image, we can clearly see gaps in the protoplanetary disk, indicating that planetary formation begins at a very early stage in a stars evolution.
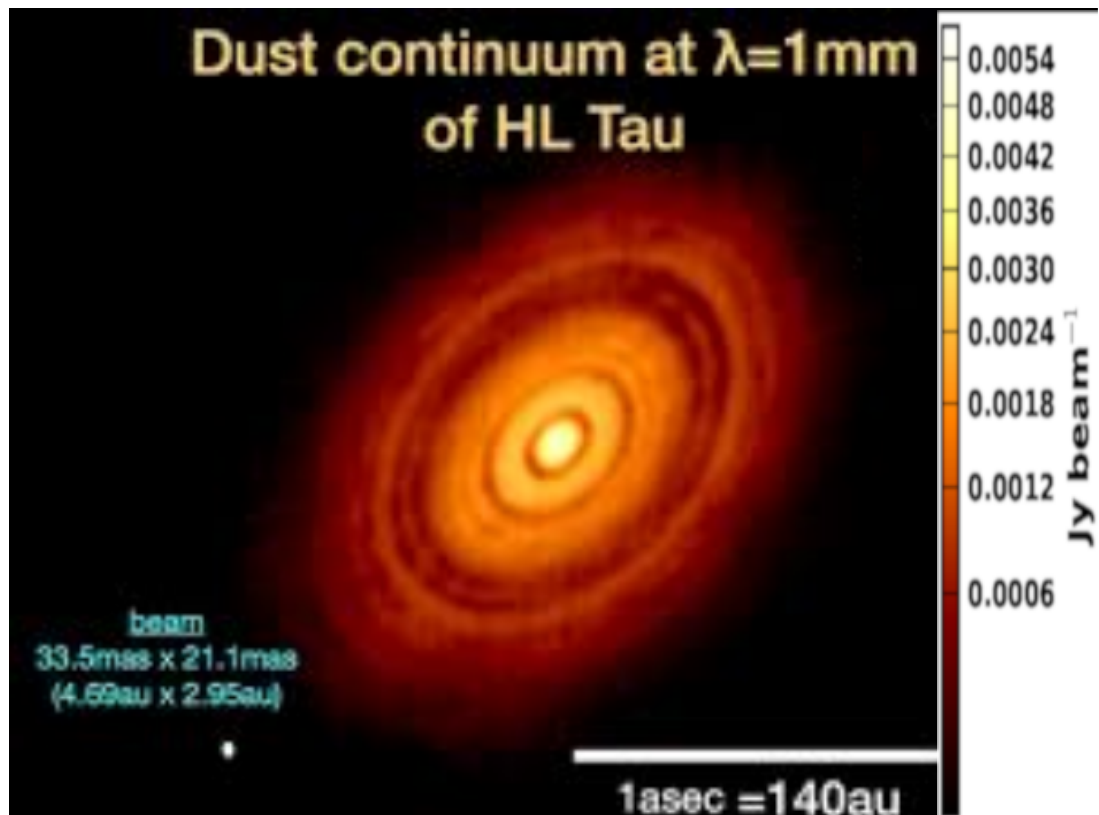
FIGURE 1.6: Image from ALMA of the T Tauri star HL Tau (ALMA-Partnership et al. 2015).

An alternative theory to the accretion model put forward above is known as the *Disk Instability* model(Kepler, Vorobyov & Basu (2010)). This model predicts the development of spiral arms in maximum-mass protoplanetary disks. These dense arms accelerate the initial core accretion process, allowing the formation of much higher mass planets within the same timescale as that of protoplanetary disks. Figure 1.7 shows the first protoplanetary disk featuring spiral arms detected at mm wavelengths, around the YSO Elias 2-27. This was the first evidence of density waves in the midplane of a circumstellar disk where most of the mass for planet formation lies. The

disk also has the regular halo structure closer to the star, perhaps indication that both core accretion and disk instability can take place in the same disk environment (Pérez et al. 2016).
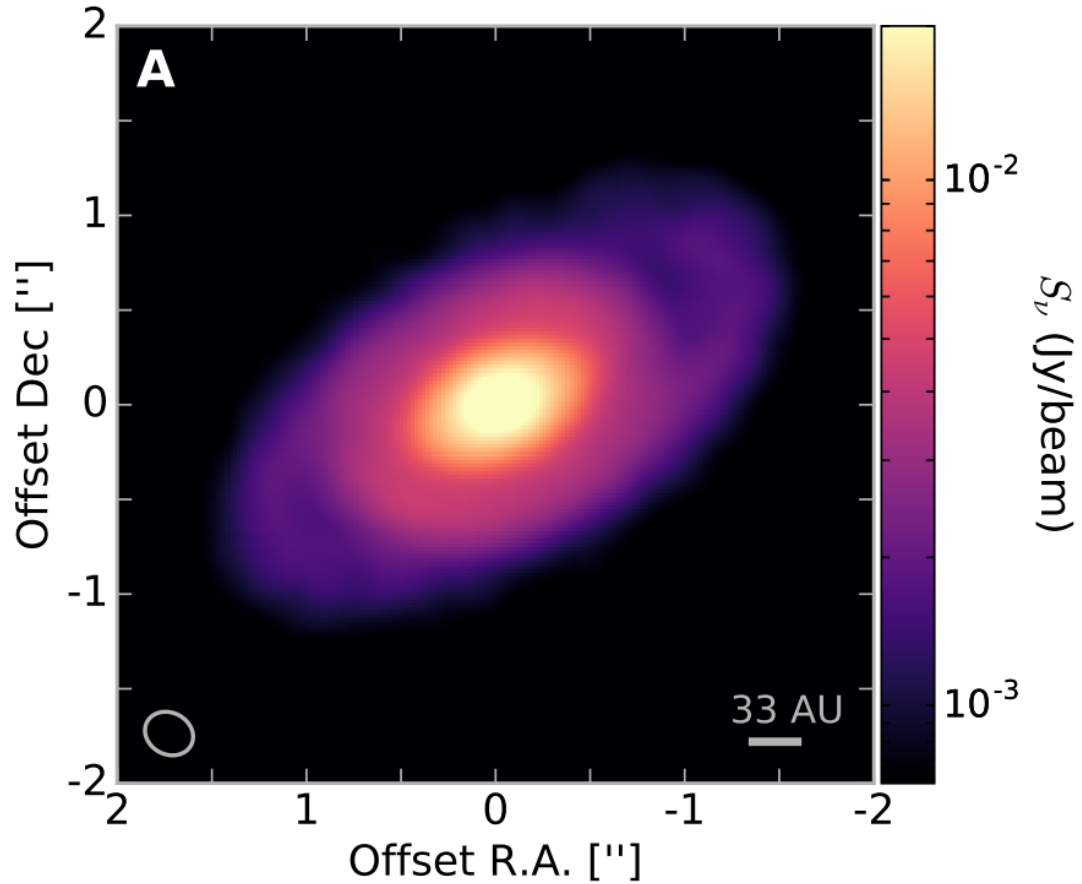
FIGURE 1.7: Image from ALMA of Elias 2-27 at 1.3mm, with the spiral arms extending out from the star (Pérez et al. 2016).

As alluded to earlier, the fact that so many planetary bodies have been discovered around stars suggests that it is a common occurrence throughout the galaxy. The most accepted models today stem from our own Solar System's evolution, but whether the configuration of our Solar System represents an exception or the rule cannot be established until we can probe planetary formation in its infancy.

1.2 Exoplanet detection techniques

With the constant improvement in telescope resolution, image reduction and detection techniques, the problem of resolving the reflected light from a planetary body orbiting a star which (considering an extremely favourable case) is 10^3 times brighter is slowly being overcome. The most successful methods bypass this condition by not directly

imaging the planet itself, but by inferring its existence via indirect methods such as changes of the radial velocity of the star caused by the gravitational pull of the planet, and decreases in the stars brightness caused by a planet transiting across the observers line-of-sight.

Indirect methods generally depend on uncommon circumstances such as transit across line-of-sight of the observer or the alignment of a foreground planet and background source in the case of gravitational microlensing. Space-based telescopes such as the Hubble Space Telescope (HST), Spitzer and Kepler, as well as ground-based telescopes, are all taking part in exoplanet detection via the transit method, resulting in it becoming the most successful method for exoplanet detection in 2014, as shown in Figure 1.8. It is an exciting time for exoplanet science, with the launch of the Transiting Exoplanet Survey Satellite (TESS) in 2018 and the upcoming launch of the James Webb Space Telescope (JWST). These will provide both a larger coverage area (TESS) and higher precision measurements (JWST) than previously achievable.
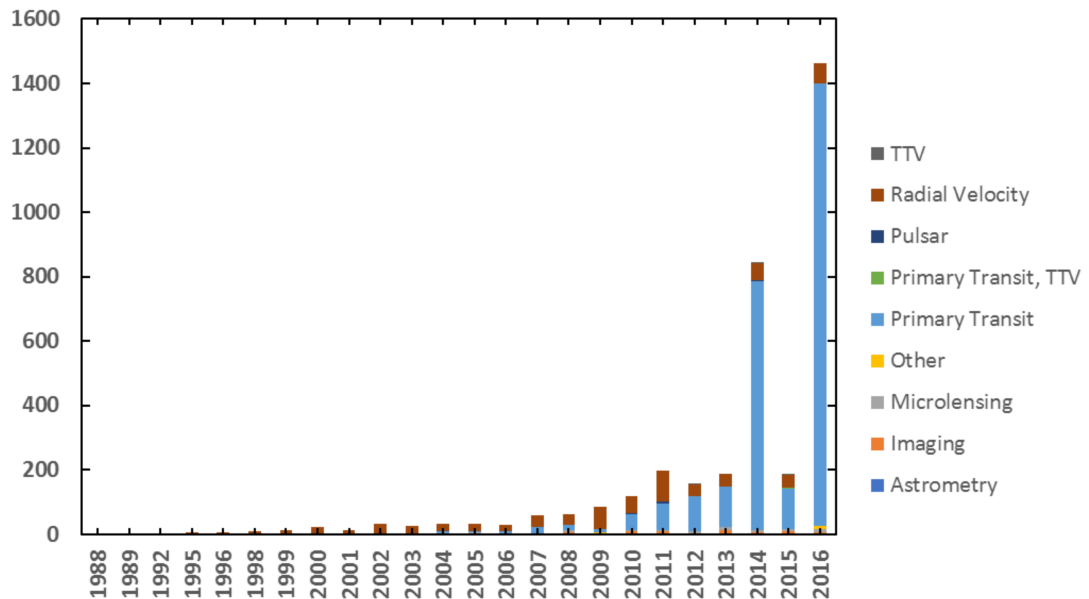
FIGURE 1.8: Count of confirmed exoplanet detections per year based upon which method was used. The data contained in this table comes from www.exoplanet.eu (TTV in this figure stands for transit timing variation).

1.2.1 Radial Velocity

The radial velocity (RV) method of detecting exoplanets is based off the fact that the radial velocity of a star will change due to its orbiting motion around the centre of mass of the star and any orbiting exoplanets. This shift in radial velocity can be detected

through the Doppler effect, in which light moving towards an observer will have its wavelength compressed (blueshift) and light moving away will have its wavelength extended (redshift). This means that an observer on Earth will see a regular shift in the central position of spectral lines based upon whether the star is moving away from or towards the observer. An example of this can be seen in Figure 1.9. The radial velocity signal amplitude, K, is given by the equation:

$$K = \left(\frac{2\pi G}{P_{orb}}\right)^{\frac{1}{3}} \frac{M_p sin(i)}{(M_* + M_P)^{\frac{2}{3}}} \frac{1}{\sqrt{1 - e^2}}, \tag{1.4}$$

Where G is the gravitational constant, P_{orb} is the orbital period, M_p is the mass of the planet, M_* is the mass of the star, i is the inclination of the system, and e is its eccentricity. We observe K, and can estimate the mass of the star from its stellar spectrum. This gives a lower limit on the mass of the planet and is largest when the star and planet are almost perfectly edge on, but the planet is not occulting the star, in which case we would have a transit. The lower limit is based upon the inclination, i, which is difficult to obtain.
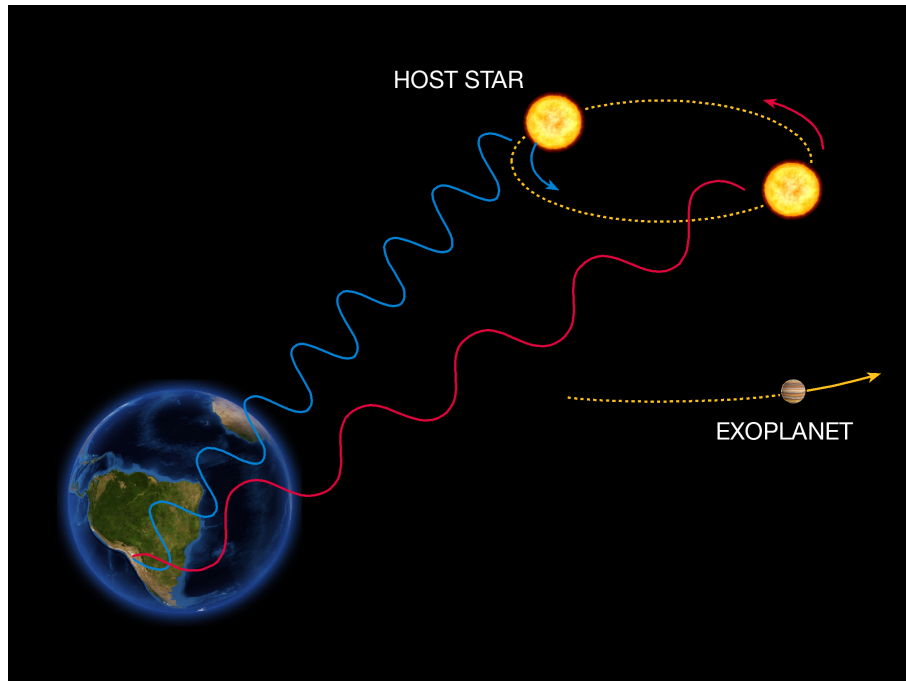
The Radial Velocity Method

ESO Press Photo 22e/07 (25 April 2007)
This image is copyright © ESO. It is released in connection with an ESO press release and may be used by the press on the condition that the source is clearly indicated in the caption.

FIGURE 1.9: Image showing the principle behind the radial velocity method. This image is taken from the website of ESO (www.eso.org).

This method has some limitations, however. Hot stars ($T_{eff} \geq$ 10,000 K) generally have higher rotational speeds, and this leads to broadening of the spectral lines. This makes the shift in central position of the lines difficult to accurately determine. The Fe lines are generally used for accurate RV measurements due to their abundance and non-saturation. For approximately Gaussian line shapes, the accuracy can be shown to be:

$$\sigma_{RV} \sim \frac{\sqrt{FWHM}}{C \cdot SNR},\tag{1.5}$$

where $FWHM$ represents the spectral lines full width at half maximum, C is the depth of the line divided by the local continuum level, and SNR is the signal-to-noise ratio of the continuum.

Another limitation of this technique comes from the need to know the orbital period P_{orb}. This means that for accurate estimations of the planetary parameters, the star needs to be observed for at least one full orbit of the planet around the parent. This is acceptable for *Hot-Jupiters*, which generally have a short orbital period of $\leq$ 10 days. For planets within the habitable zone, the period would be much greater, requiring longer observations of the parent star.

Multi-planet systems, such as our Solar System, also lead to asymmetrical RV measurements, and these perturbations can be difficult to discern from stellar activity. The RV method was used to detect the first confirmed exoplanet orbiting a sun-like star, 51 Pegasi b (Mayor & Queloz 1995).

In the context of our study, the RV method is unsuitable as the planets will still be forming and have not accreted the majority of their final masses. This greatly reduces the RV variations in the parent star, and current telescopes cannot match the sensitivity needed for such detections.

1.2.2   Planetary Transits

As mentioned above, planetary transits (also known as transit photometry) occur when the orbital plane of the planet is edge-on between the observer and the parent star, shown in Figure 1.10. This transit creates a minute drop in the stellar flux of the star. While this is an extremely rare occurrence, the technique itself allows telescopes to monitor a large number of stars simultaneously, increasing the chance of observing such an occurrence. The drop in flux of the parent star is proportional to the ratio of the radii of both the planet and the star squared, given by:

$$\frac{\Delta L}{L} = \left(\frac{R_P}{R_*}\right)^2, \tag{1.6}$$

with the assumptions that both the planet and star are spherical in shape, and that the flux from the planet in negligible compared to that of the parent star.
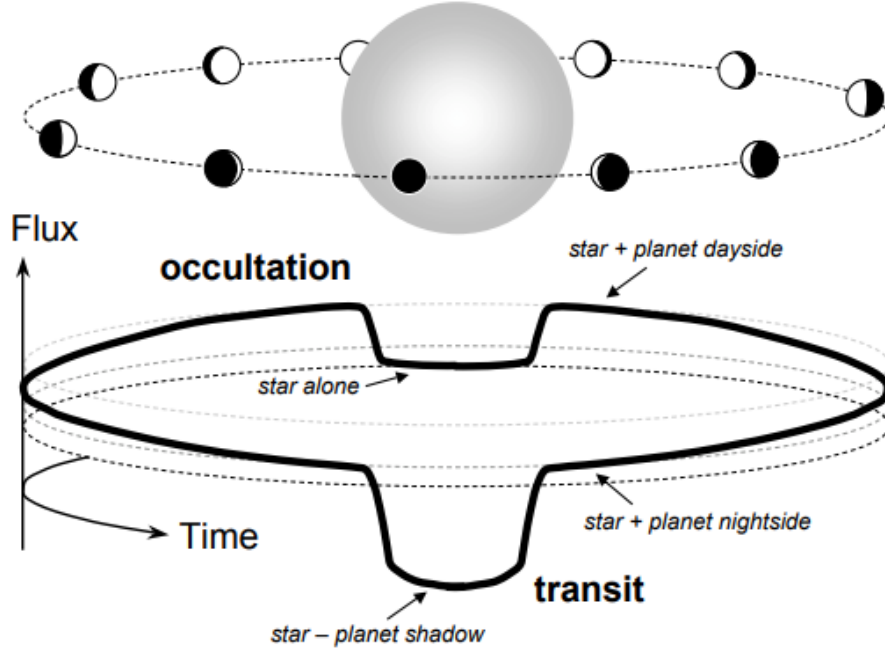
FIGURE 1.10: Image showing the various phases involved in the transit method of exoplanet detection (Winn 2010)

The transit method does allow for several parameters of the planet to be deduced by the shape of the light curve. For example, larger planets will cause a deeper dip in flux, and planets further away will have a longer transit time. In addition, light from the star passing through the planet's atmosphere acts as a probe to its composition. Finally, transit photometry also has no issues with multi-planet systems, as each planet's transit can be extracted from the photometric data (as long as they are in line-of-sight with the observer).

The probability of actually detecting a transit was derived by Winn (2010) and is given by the equation:

$$\rho_{transit} = \left(\frac{R_* \pm R_p}{a}\right)\left(\frac{1 + esin\omega}{1 - e^2}\right), \tag{1.7}$$

where R represents the radius of the star (*) or planet (P), a is the semimajor axis length, e is the orbital eccentricity and ω is the angle between the observers point of

view and the orbital plane of the planet. The "plus" case allows for grazing eclipses and the "minus" case does not. Naturally, the larger the radius of the star, the greater the chance of observing a transit, as there is more area with which a telescope can monitor. For an Earth-sized planet with $a = 0.05$ AU, the probability is $\sim 0.5\%$. However, this method does not rely on tracking a single star to take measurements, and so many stars can be extracted from a wide field of view, helping to overcome the low chance of actually observing a transit per star analysed.

False positives also occur quite often, with a small star orbiting close to a large companion mimicking the signal one would expect from a planet transiting a star.

The transit method is incompatible with exoplanet detection around YSOs as the planets will still be embedded in their protoplanetary disk, preventing a transit from being observed. Another method is still needed if we are to probe exoplanet formation.

1.2.3 Direct Imaging

Direct imaging is seen to represent the most promising method of exoplanet detection as it does not depend on any specific alignment of the stellar midplane with respect to an observer. The only time when a planet would not be detectable is when it is either behind or in front of the parent star. In this unlikely case, the transit method can be used. Direct imaging also allows planetary characteristics to be derived by spectroscopic and photometric measurements. This could potentially allow us to determine the true dispersion of planetary systems in our Galaxy, which is a remarkable goal.

This goal is fraught with obstacles, however. The light reflected from a Jupiter-like planet with a similar orbit to a solar-type star is around 10^{-9} times that of the solar flux itself. This number is derived for an observer only 10 pc away, and gets smaller at larger distances. Therefore extremely high contrast is needed to detect such faint objects. Another major hurdle is the fact that atmospheric turbulence causes temperature fluctuations, which alter the refractive index of air. This effect is commonly referred to as the *seeing* of an observation night, and can be compared to heat haze on a sunny day. This turbulence alters the wavefront of incoming radiation, introducing distortions to the point spread function (PSF) of the telescope, as can be seen in Figure 1.11. Exoplanets can fall on the stars PSF itself, unless there is sufficiently high resolution.

For an ideal telescope, the diffraction limit is given by the equation
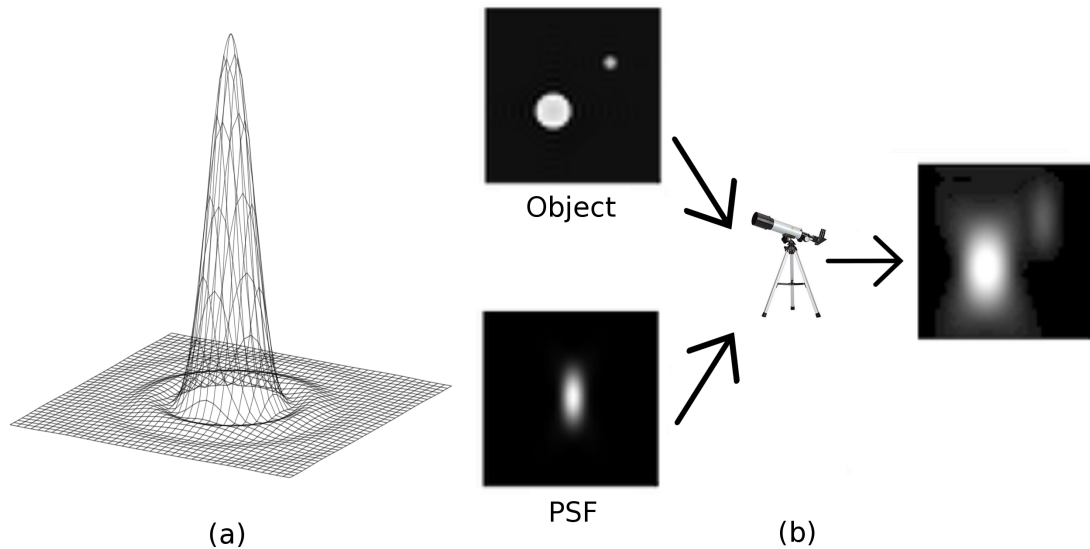
FIGURE 1.11: (a) shows the Airy function, which is the theoretical PSF of a star produced by an ideal telescope. (b) shows the distortion effect of an imperfect PSF on an astronomical object.

$$\theta = 1.22 \frac{\lambda}{D}, \tag{1.8}$$

where θ is the angular resolution in radians, λ is the wavelength and D is the diameter of the lens aperture.

There are many techniques which attempt increase the contrast for large-aperture telescopes. These include (but are not limited to) coronagraphy, differential imaging and optical interferometry. These methods have had some remarkable successes, but they are still limited to looking at young stars located within ~ 200 pc. These conditions increase the detection chance as young stars should have planets that are still in formation. Forming planets are brighter than their fully formed counterparts, and the distance condition helps to increase the overall angular separation, making it easier for telescopes to resolve the planet from its parent star.

Figure 1.12 shows 2M1207b, an exoplanet in wide-orbit around the brown dwarf 2M1207 (Chauvin et al. 2004). This detection was possible as the parent star is a brown dwarf with a mass of around 25 M_{Jup}, and the planet itself has a mass of approximately 5 M_{Jup}. The low luminosity of the brown dwarf and the large size of 2M1027 lowered the contrast needed to resolve such a system.

One way of reducing the distortions caused by the temperature variations was proposed in 1953 by Horace Babcock. He saw the potential of creating a device which could measure the wavefront aberrations and account for them in real time. This was beyond

the technology of the time, but further development was to come from an unlikely source. The United States military saw the potential of Babcock's idea and developed adaptive optics (AO) to help them track the progress of Soviet satellites, as they feared weapons being put into orbit. The countermeasure was to shine a laser from Earth to a satellite in space, which would reflect the laser towards the missile and destroy it. The researchers found that disturbances in the atmosphere caused the laser to disperse, reducing its destructive power. They developed a way of predicting the dispersion caused by the atmosphere, and counter-dispersing the initial laser beam in such a way that when it reached its target, it would converge back into a focused beam (Palca 2013). In 1991, the US government agreed to declassify the work they had done on adaptive optics, and since then it has been instrumental in overcoming atmospheric distortions from ground-based observations.
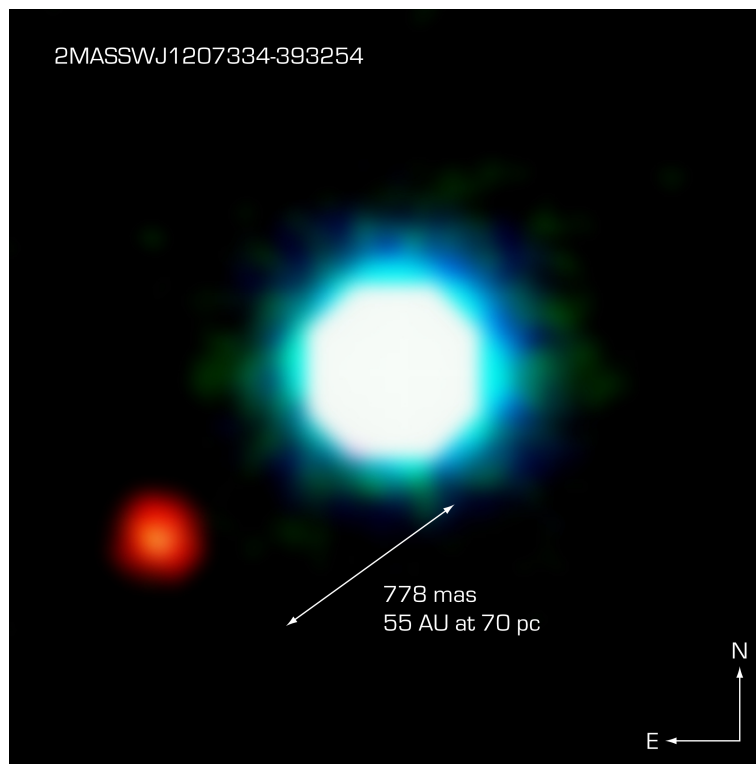
FIGURE 1.12: Image of 2M1027b, the first confirmed exoplanet discovered by direct imaging (Credit: www.eso.org).

Modern adaptive optics systems use a wavefront sensor which receives some of the light from the telescope to identify the optimal mirror configuration in order to account for the atmospheric turbulence. This is then fed to a deformable focusing mirror, which adjusts itself correspondingly. This feedback loop occurs hundreds of times a second and results in a much clearer image of the object under observation, as the deformable mirror constantly adapts to the change in atmospheric temperature, hence the name (A standard setup is depicted in Figure 1.13). As ground-based telescopes

are not limited by size, adaptive optics have allowed them to reach similar if not better resolution than what is achievable in space. Many space-based missions will also employ adaptive optics to account for the interstellar medium (ISM) temperature fluctuations. Direct imaging instruments have been proposed for the Extremely Large Telescope (ELT), which would greatly increase the distance at which exoplanets can be directly detected. For example, the VLT has an angular resolution of 2 mas, where as the ELT will have an angular resolution of 0.5 mas, which is 4 times higher assuming both are used for imaging at the same wavelength, and 16 times higher resolution than the Hubble Space Telescope (HST).
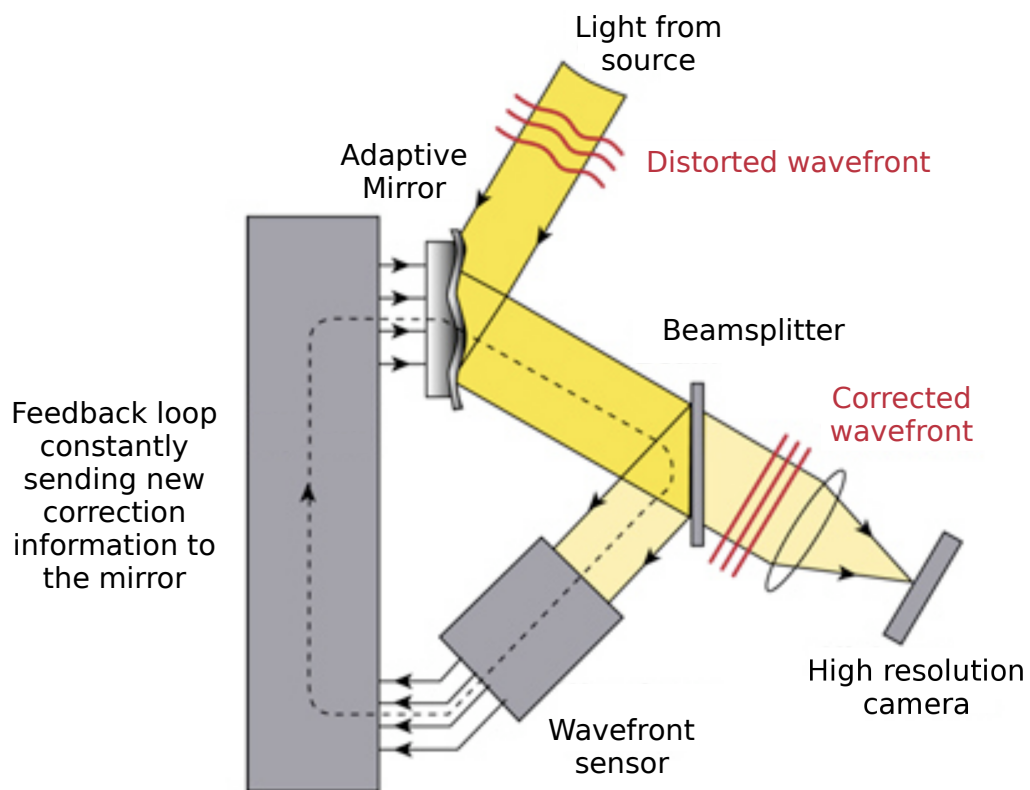
FIGURE 1.13: Diagram showing the feedback loop employed by adaptive optic systems (Credit: NSF Center for Adaptive Optics, cfao@ucolick.org).

Even with AO-aided observations, resolving a protoplanet from the circumstellar disk and its parent star is a tough challenge. One benefit of observing planets at this early stage is that they are still actively accreting material, and so should be hotter and more luminous than fully formed planets. There have been several attempts to directly image exoplanets within TD objects (Close et al. 2014; Huelamo et al. 2011; Schmidt et al. 2008), but so far, very few exoplanets have been confirmed around TD objects (Keppler et al. 2018; Kraus & Ireland 2012; Sallum et al. 2015). Current telescopes dedicated to

the direct imaging of extrasolar planets include the Spectro-Polarimetric High-contrast Exoplanet REsearch instrument (SPHERE) and the Gemini Planet Imager (GPI).

1.2.4 Astrometry

Astrometry is the oldest exoplanet detection technique, first used by William Herschel in the 18th century. Herschel noticed that a star which he was tracking seemed to wobble as it moved, and he hypothesized that this was due to the gravitational pull of a planet orbiting the star (Figure 1.14 shows the principles behind this method). For two centuries this method was used to detect exoplanets, but none of these detections stood up to scrutiny from other astronomers.
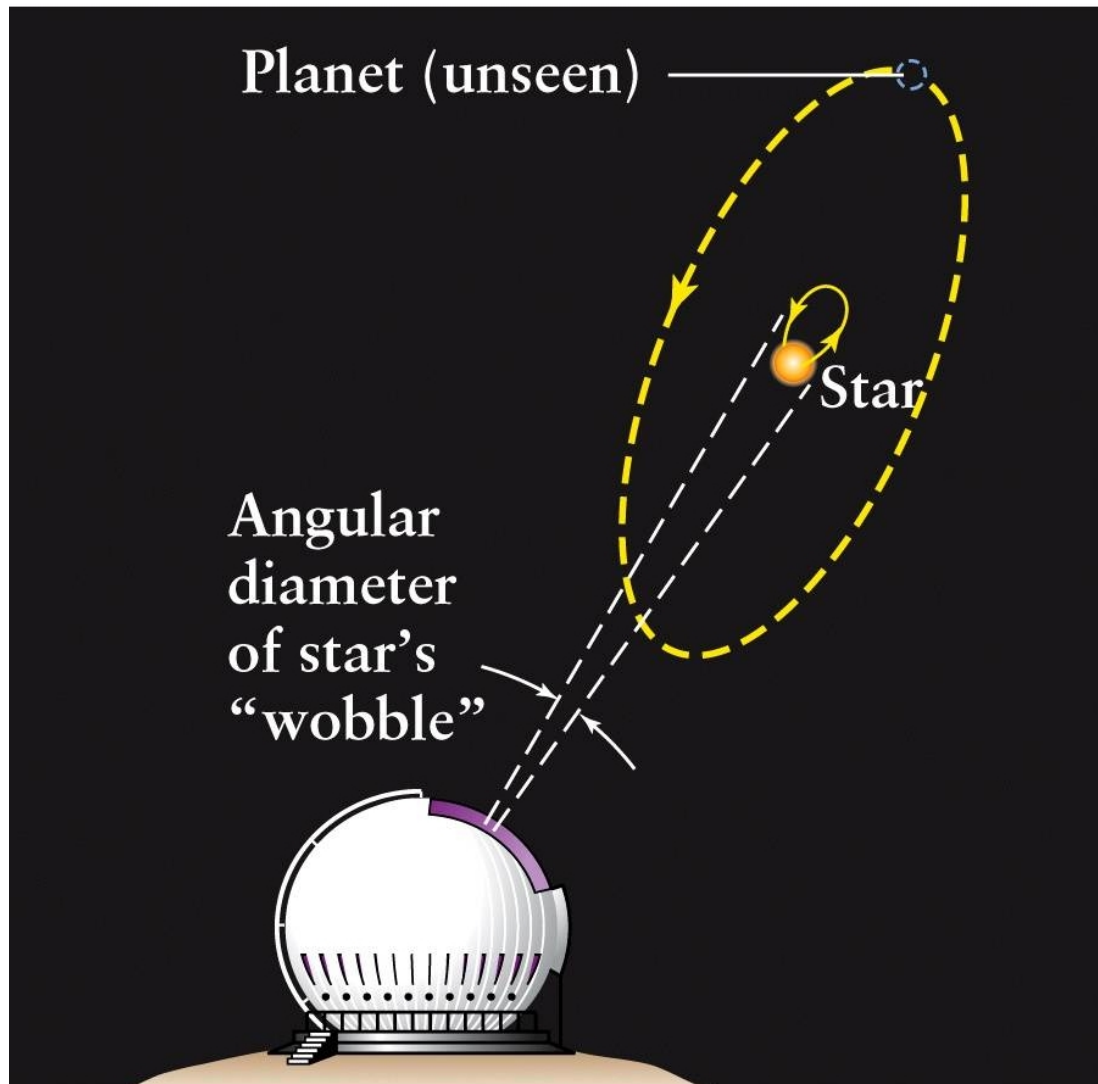
FIGURE 1.14: Picture showing how measurements are taken via the astrometric method (Image taken from https://www.sron.nl).

The theory behind the technique was correct, but the equipment at the time was unable to measure the stellar position to a high enough degree of accuracy. This was mainly due to both the complexity of optical setups and the effects of our atmosphere. This changed in 1989 with the launch of *Hipparcos* by the European Space Agency (ESA).

The angle of the semi-major axis orbit of a star due to an orbiting exoplanet is given by the equation:

$$\theta = \left(\frac{G}{4\pi^2} \right)^{\frac{1}{3}} \frac{m_p}{M_s^{\frac{2}{3}}} \frac{P_{orb}^{\frac{2}{3}}}{D}, \tag{1.9}$$

where M_s and m_p are mass of the star and planet respectively, D is the distance to the star system and P_{orb} is the orbital period of two-body motion (Xu et al. 2017).

The Hipparcos Catalogue contained accurate proper-motion studies of over 180,000 stars in our galaxy, with two more subsequent catalogues being released for over 2,000,000 stars. While this allowed detection of binary star systems, the accuracy was still not high enough for exoplanet detection. A follow-up mission, *Gaia*, was launched by ESA in 2013 with one of its objectives being to determine the mass of 1000 extrasolar planets using astrometry. While *Gaia* does contain a radial velocity spectrograph, the sensitivity is still not high enough for exoplanet detection.

1.2.5 Spectro-astrometry

Spectro-astrometry (SA) is an analysis technique that uses a combination of the measurement of the electromagnetic spectrum of an object, *spectroscopy*, and the precise measurement of its position, *astrometry*. It involves taking spectra at different position angles (PAs) and looking for indications of deviation from the central object, similar to how the astrometry method looks for deviations in the centre of mass of an extrasolar system. For example, when spectro-astrometry is applied to a star, a position spectrum can be produced by fitting the spatial profile as a function of wavelength. Any astronomical object such as a binary or bipolar outflows that are asymmetric about the centroidal position will show deviation in the position spectrum from the expected single-star profile. The important distinguishing factor from astrometry is that the different emission line regions (ELRs) of the star can be analysed. This allows the origin of these emission lines to be determined, which is especially important in the case of unresolved binaries or biploar outflows. SA information can also be calibrated as a function of velocity, used for example in resolving the high and low velocity components for outflows (Nisini et al. 2017).

The idea behind using SA as a technique for exoplanet detection stems from its previous use in exploring the ELR of binary stars. Hα is known to be an accretion tracer, and PMS binaries can be identified by spectro-astrometric analysis of this line. Unless both stars have the same stellar parameters and accretion properties (which is highly unlikely), one star will have a stronger emission line strength, and the centroid will be drawn towards that star. Difference in line width can also cause a deviation from the centroid of a binary star system, as a star with a wider line profile must only overcome the continuum of the other star. Larger exoplanets also undergo accretion, and so applying SA to a YSO offers an alternative method of detecting an accreting exoplanet than the techniques mentioned previously. From results of Hα, the mass accretion rate ($\dot{M}_{acc}$) can also be calculated, and this offers an indication of how evolved a PMS star is, as older PMS stars have less material left to accrete and therefore a lower $\dot{M}_{acc}$. There are also a number of other accretion tracers besides Hα, including Brγ, NaD, Ca II and Paβ, that can be analysed in the attempt to detect accretion from an exoplanet. The [OI]λ 6300 Å line can also be used as an indirect tracer of accretion, as an empirical connection between the different component strengths and $\dot{M}_{acc}$ has been determined (Nisini et al. 2017).

Summary

Star formation begins when a cloud of gas and dust loses its equilibrium via one of many mechanisms. Once this occurs, the cloud will begin to collapse, but as the contraction occurs isothermally, the cloud splits further into numerous local cores. These then collapse forming a central protostellar core, a protostellar disk, an envelope and bipolar outflows. Once the envelope has been removed, the star becomes a Class II object. A subset of these objects known as transitional disks, have had their circumstellar disk partly cleared via either planet formation, photoevaporation, or both. These objects represent the earliest stage of planetary formation that can be detected in the visible regime.

Most current exoplanet detection techniques, such as the radial velocity and transit methods, require the central star to be relatively stable in order for accurate measurements to be taken. TD objects would provide false signals to both of these methods due to the RV fluctuations and the variability in their luminosity intrinsic to YSOs. Direct imaging represents the most promising method in which to observe planetary formation, but the accuracy needed to resolve an object often 1000 times smaller than its parent star remains a difficult task. Only the most advanced ground-based telescopes fitted with adaptive optics can reach this resolution, and until the *James Webb*

Space Telescope begins releasing data, the amount of directly imaged exoplanets will remain low compared to the other major techniques. Spectro-astrometry is presented as an alternative method in which planets in formation around TDs can be detected. It analyses ELRs of possible candidates and aims to detect deviations from the central position spectrum that a single star with no companion would display.

Chapter 2

Spectro-astrometry

2.1   A brief history

Modern SA began in 1982, when Jacques M. Beckers realised that differential speckle-interferometry could be used to resolve binary stars below the standard limit of speckle interferometry; the size of the speckle itself. Beckers realised that for a pair of binaries orbiting a centre of mass, comparing a single speckle at two different wavelengths would show a slight change in the speckle profile. This is due to the Doppler effect, where the star with an orbital motion towards the observer will have a different line profile to that of one moving away from the observer. Fourier analysis of the difference results in direct measurement of the separation and position angle of the binary system. This technique required a special instrumental setup, but enabled close binaries to be resolved beyond the resolution limits at the time. Its main use was in resolving binaries with a V magnitude greater than 7.5 (Beckers 1982).

Bailey (1998b) proposed the use of a standard long-slit charge-coupled device (CCD) for spectro-astrometric measurements. Bailey was investigating pre-main sequence (PMS) binaries, and so used a Hα filter as accretion is still ongoing for PMS objects. For this setup, the reduced observations were viewed at a PA of 0°, 90°, 180° and 270°. The anti-parallel observations were subtracted from each other to remove instrumental effects such as curvature in the spectrum and deviation from the central CCD columns due to misalignment. The orthogonal PAs allow accurate determination of the PA of binaries to be recovered from the observations. Figure 2.1 shows the typical output of a spectro-astrometric observation after PA combination around the Hα emission line.

SA has been used for a wide variety of studies, which began with close-separation binaries (Bailey 1998a; Takami et al. 2003), and as the technique became more widespread
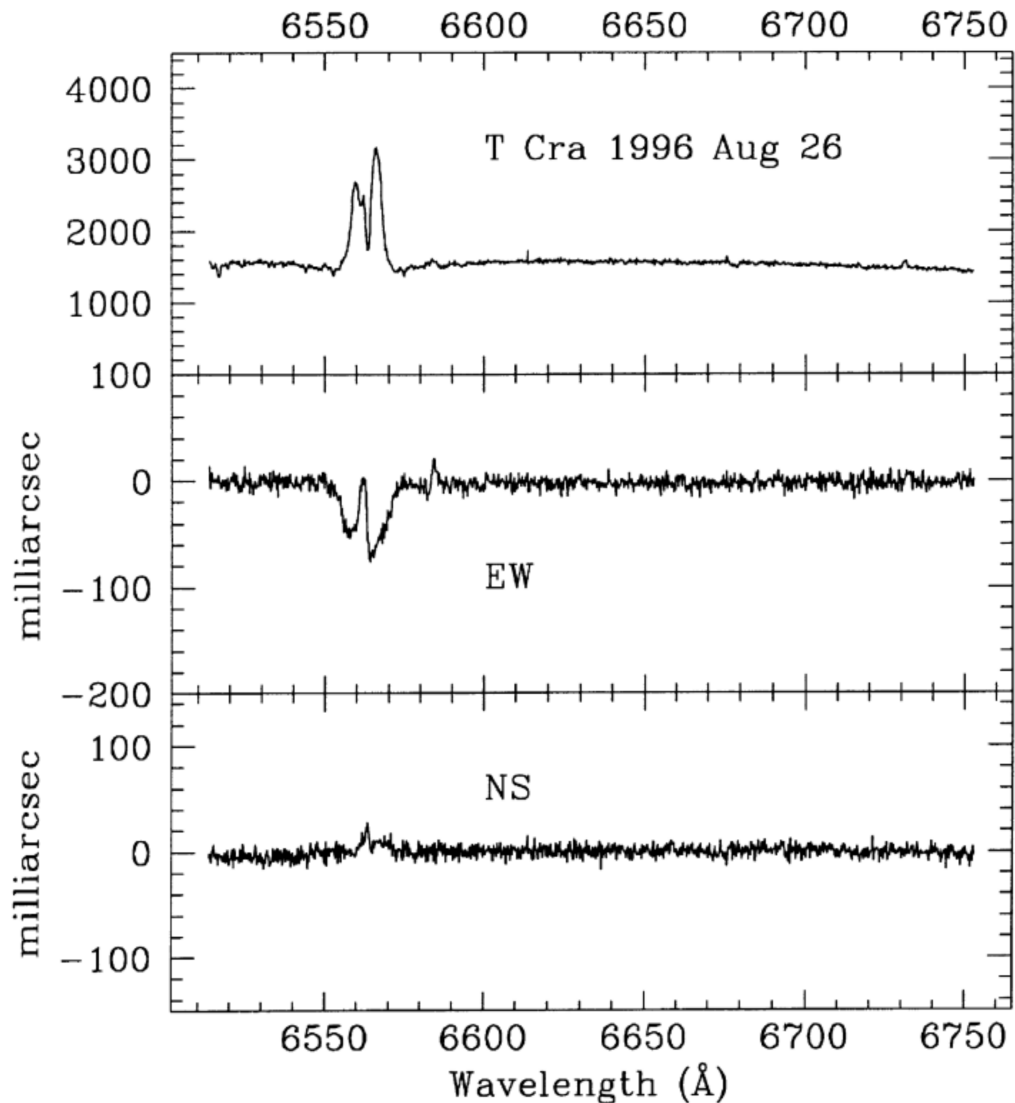
FIGURE 2.1: Spectro-astrometric observation of the PMS star T Cra. This image shows the flux around Hα (Top panel), and the emission centroid with respect to the stellar continuum for both east-west (middle panel) and north-south (bottom panel) PAs. They were constructed using the 4 PAs mentioned above and taken with the RGO spectrograph on the 3.9m Anglo-Australian Telescope. Image taken from Bailey (1998b).

it saw use in investigating outflows (Whelan et al. 2004) which led to the discovery of outflows around brown dwarfs (BDs Whelan et al. (2006)). It has also found use in investigating Keplerian motion in circumstellar disks (Pontoppidan et al. 2008), probing the gas of circumstellar disks (Brittain et al. 2015; Brown et al. 2013; Pontoppidan et al. 2011), black holes (Gnerucci et al. 2010; Stern et al. 2015) and planetary nebula (Blanco Cárdenas et al. 2014) to name but a few. Figure 2.2 shows how SA is used to calculate directional information of jets and outflows.
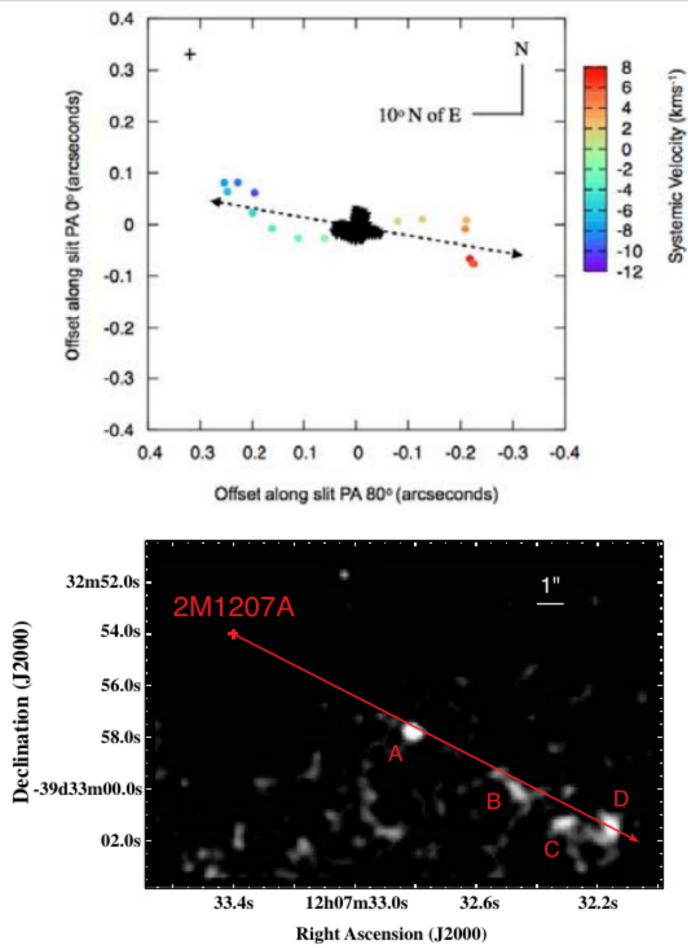
FIGURE 2.2: Example of how SA can provide directional information about jets and outflows. Image taken from Whelan (2014) using the visual and near UV FOcal Reducer and low dispersion Spectrograph (FORS) on the VLT showing the direction of the outflows around the brown dwarf 2MASS1207A.

2.2 Technique

The steps involved in spectro-astrometric observation and the subsequent reduction of those observations is well documented (Bailey 1998a; Takami et al. 2001). Echelle spectra are reduced and transformed into a single long 2d point spread function. The spatial profile has historically assumed to be Gaussian due to the atmospheric refraction, given by the telescopic seeing on the night of observation Bailey (1998b). During this project it was found that a Voigt fit provided a better fit to the wings of the spatial profile than the Gaussian fit for the Ultra Violet Echelle Spectrograph (UVES) instrument with which the observations were taken. These observations and the detector are described in detail in Section 3. Therefore, a Voigt fit was used at all times for the spectro-astrometric analysis. As discussed in Whelan et al. (2015) the precision in the

Voigt fit can be well approximated by Equation 2.6. Fitting a Voigt across the spatial axis allows interpolation beyond the pixel spatial scale.

The package *lmfit* for Python was used to fit a Gaussian, Voigt and Lorentzian function to our data to compare accuracy, and the results can be seen in Figure 2.4. The $\tilde{\chi}^2$ goodness of fit test was also performed for each of the functions, with the Voigt profile having the lowest value. In the bottom graph of Figure 2.4 the difference between the source spatial profile and the fit per pixel is plotted, with the Voigt profile still offering the lowest average difference across the pixel axis. For future uses of spectro-astrometry, the Voigt fitting function should be considered as well as the standard Gaussian form.

A second order polynomial is then fitted to the position spectrum to remove instrument curvature, which is seen in echelle spectra as the curving of each order before addition. These must be removed in order to have a true central position from which to measure the offset of any astronomical phenomena. An example of an unprocessed Echelle spectrum can be seen in Figure 2.3. Once the fitting has been completed, a set of central positions as a function of wavelength remain. This allows any offset in central position of accretion tracers to be detected beyond the seeing limit.
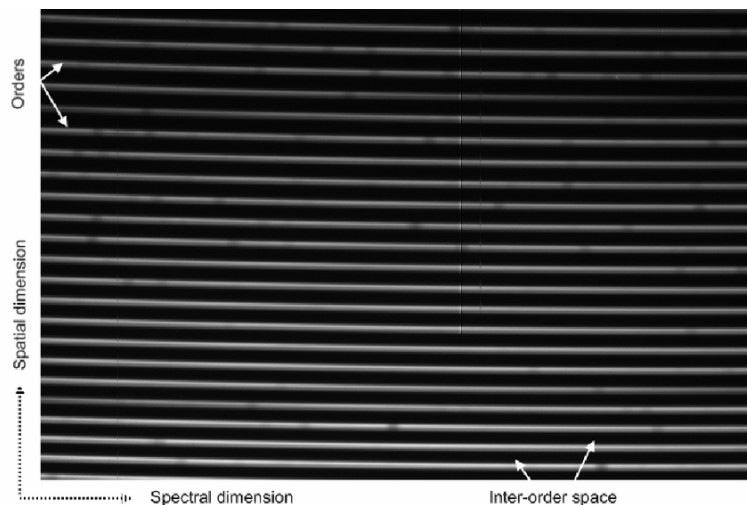
FIGURE 2.3: Figure showing an unprocessed Echelle spectrum of T Cha. The curving of each order can be seen, caused by the splitting of light into its wavelength components.

When the spectrum has been straightened, the next step is to remove the continuum contamination, which occurs, for example, when an absorption feature of a small binary star is filled in by the emission of its larger companion in the same waveband. This is especially relevant for objects which are expected to have a much lower flux level than the source objects, such as substellar objects orbiting around main-sequence stars. It is well known that the emission line barycentre is dragged back towards the
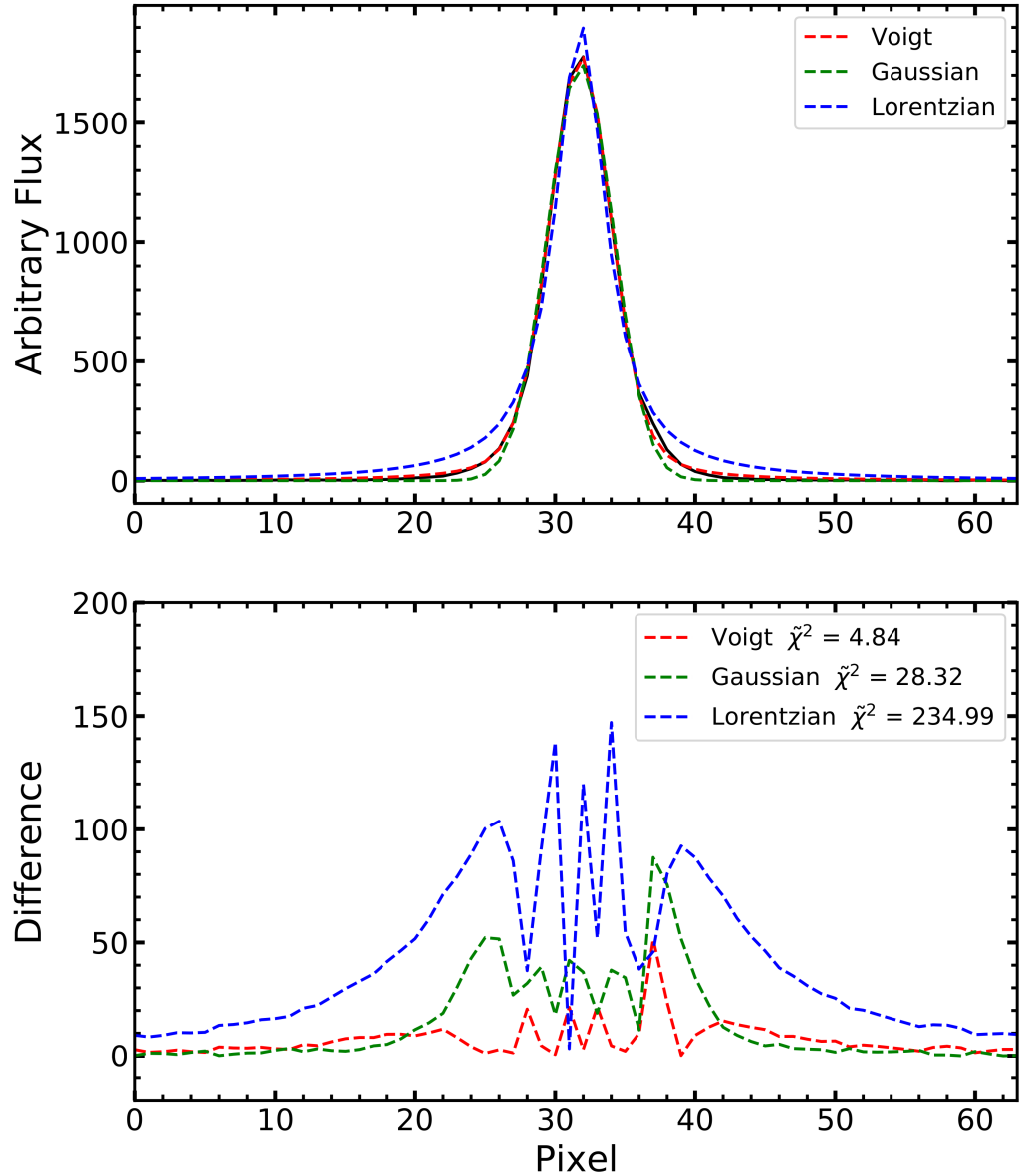
FIGURE 2.4: Figure showing the fit of the source spatial profile for various distributions (top). The bottom panel shows the residuals for each fitting function and their $\tilde{\chi}^2$ values are given in the legend.

source by the continuum, and this can be prevented by simply removing the continuum by using routines in a program such as *IRAF* (as in Whelan & Garcia (2008)), or by calculating the line to continuum intensity ratio and dividing this into the raw positional displacement. This factor is given by

$$I_{\lambda(line)}/[I_{\lambda(line)} + I_{\lambda(cont)}], \tag{2.1}$$

and represents the ratio of intensities of the continuum and line region associated with this continuum level (Takami et al. 2001). This allows previously hidden displacements in the line region to be uncovered, but can only be applied to emission line regions for obvious reasons.

One technique which can be used to increase the signal-to-noise ratio is to bin the resulting spatial profile. One must be careful when binning, as there must be sufficient sampling across the line profile under investigation. As an example, in CTTSs we see Hα line profiles with a wide velocity range, shown in Alencar & Basri (2000) to be anything from $\pm$ 200 to $\pm$ 400 km s^{-1}. If such a CTTS had a substellar companion still in its accretion phase, a Hα line profile of up to $\pm$ 200 km s^{-1} could be expected (Joergens et al. 2013). For this situation a binning factor of the parent star would need at least 10 points across the 400 kms^{-1} line profile for accurate analysis. If a typical high-res spectrograph provides a resolution of 1 km s^{-1} then a bin of up to 40 could be used to increase the signal-to-noise while retaining the form of the line profile.

Figure 2.5 shows an example of the effect of binning on the resulting plots. The binned flux covers up features in the line profile, seen as the top two plots in the figure. For this reason, the fluxes throughout this thesis have not been binned. The centroid and FWHM retain their overall shape, but features hidden within the fluctuations become more apparent, and the sigma is lowered substantially. Therefore, any emission lines showing evidence of signals will be binned to further improve the accuracy of the centroid and FWHM measurements. For both, it is important to increment the binning factor up to the maximum (in this work a value of 40 was chosen) to ensure no smaller-scale signals are masked.

2.2.1   Voigt Profile

The Voigt function is a spectral line profile which has been used in spectroscopy as an approximation of a line profile which has been broadened by both the Doppler Effect and, either Lifetime or Pressure broadening, or a combination of the two. If the line was broadened purely by the Doppler Effect, we would have a Gaussian distribution, but the combination of the other two broadening mechanisms gives a Lorentzian distribution. This accounts for the non-zero intensity at the wings of the distribution, and is why a Voigt profile (which is a convolution of Gaussian and Lorentzian distributions) gives the most accurate approximation of the line profiles we see in our spectra, as seen in Figure 2.4.
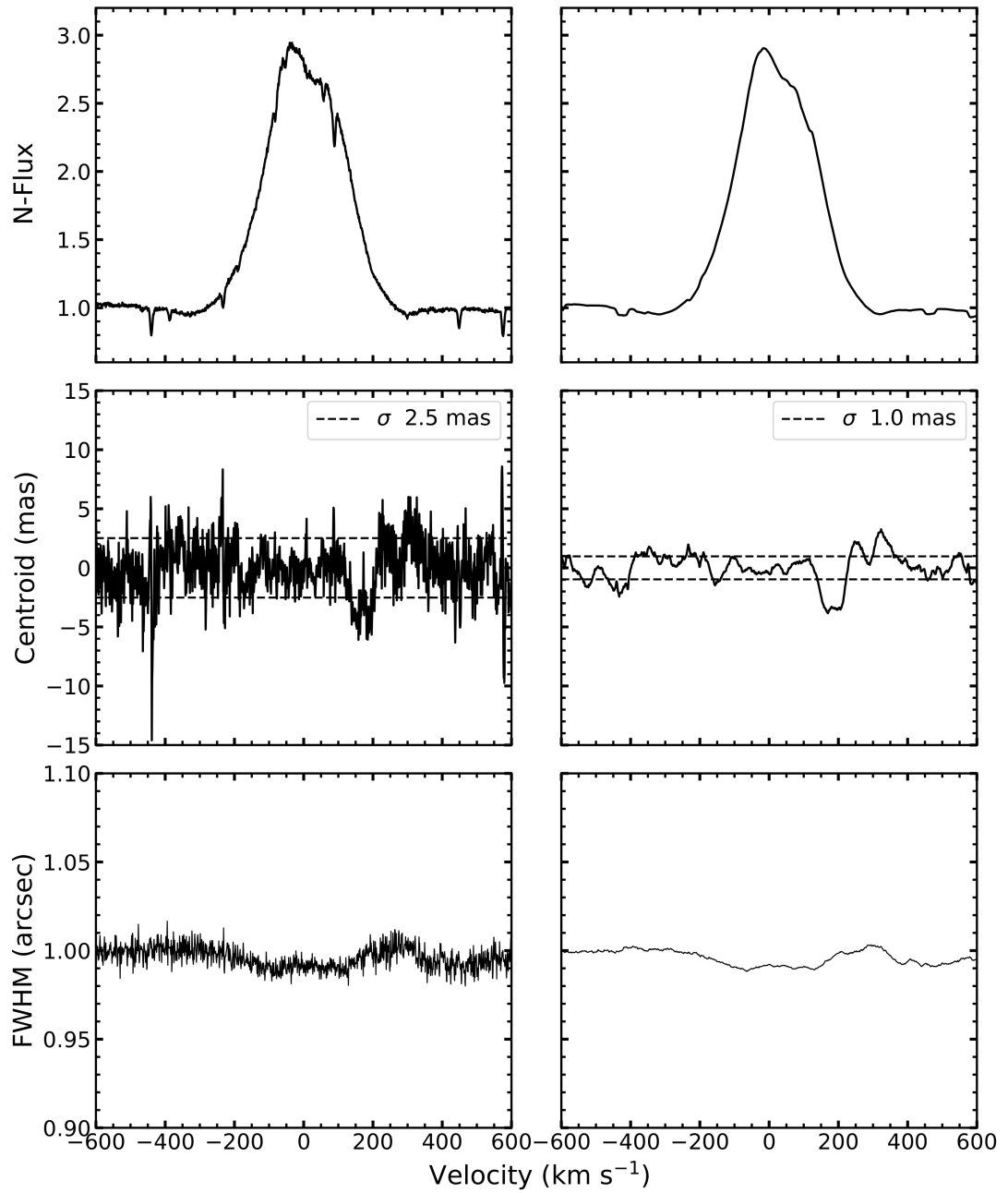
FIGURE 2.5: Figure showing a comparison between unbinned (left) and binned data (right) from HD 142527. From top to bottom: Hα normalised flux, centroid wrt. the continuum, and the FWHM. Plots on the right have been binned by a factor of forty.

$$V(x, x_c | \sigma, \gamma) = \int_{\infty}^{\infty} D(x'|\sigma)\, L(x - x_c - x'|\gamma)\, dx', \qquad (2.2)$$

where $x - x_c$ is distance from line centre x_c, $D(x|\sigma)$ is the centred Doppler profile:

$$D(x|\sigma) = \frac{e^{-x^2/2\sigma^2}}{\sigma\sqrt{2\pi}}, \qquad (2.3)$$

31

and $L(x - x_c|\gamma)$ is the centred Lorentzian profile:

$$L(x - x_c|\gamma) = \frac{\gamma}{\pi((x - x_c)^2 + \gamma^2)}. \tag{2.4}$$

The FWHM of the Voigt profile can be found from the widths of the associated Gaussian and Lorentzian widths. The FWHM of the Gaussian profile is $f_G = 2\sigma\sqrt{2\ln(2)}$. The FWHM of the Lorentzian profile is just $f_L = 2\gamma$.

The FWHM of the Voigt profile is well approximated as

$$f_V \approx 0.5346 f_L + \sqrt{0.2166 f_L^2 + f_G^2}, \tag{2.5}$$

with an accuracy of 0.02 % Olivero & Longbothum (1977).

2.3 Spectro-astrometric precision

The biggest advantage of using this technique is that the resolution limit is not dependant on the pixel scale of the detector. The precision to which the centroid can be measured is primarily dependent on the signal to noise ratio (SNR) of the spectrum and is given by

$$\sigma = \frac{FWHM}{2.355(\sqrt{N_p})}, \tag{2.6}$$

where N_p is the number of detected photons. This allows resolution of objects that are normally below the seeing limit of the telescope itself. Position spectra can also be binned by an appropriate amount to increase SNR ratios, with the cap on the binning being the expected signal width of the line profile under observation. Close et al. (2014) estimate the Hα equivalent width (EW) to be in the range of 150 - 200 km s^{-1} for a 0.25 M$_\odot$ object. For such an object, the position spectra could be binned up to ~ 25 km s^{-1} to ensure enough sampling across the line profile of the object. In 2011, Pontoppidan et al. (2011) succeeded in using AO to obtain photon-limited angular resolutions of 100 - 500 µ-arcseconds. SA had been used to investigate a variety of objects from brown dwarf jets to quasars (Stern et al. 2015; Whelan 2014). With the development of AO, the precision of SA has reached a point where it can be used to investigate disk composition and structure around T Tauri and Herbig Ae/Be stars (Brittain et al. 2003; Brown et al. 2013; Pontoppidan et al. 2008).

2.4   Artefacts and false signals
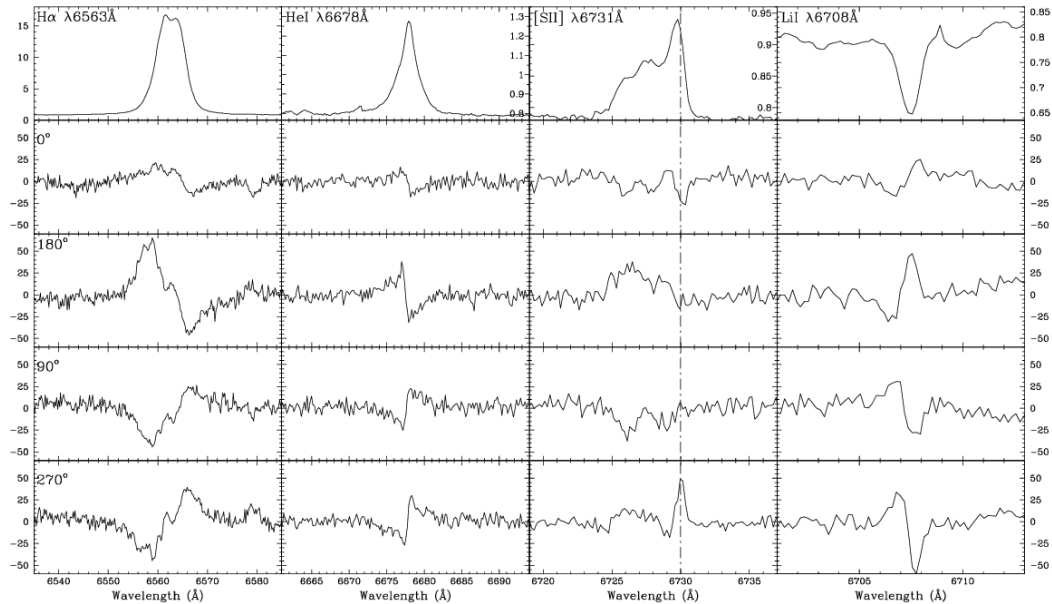
FIGURE 2.6: Figure taken from Brannigan et al. (2005) in which instrumental effects can be seen to mimic real signals. The intensity and position spectra were obtained with the ESO Multi Mode Instrument (EMMI) on the New Technology Telescope (NTT). PAs from top to bottom are 0°, 180°, 90° and 270°, and the lines from left to right are Hα HeI, [SII] and Li. The Hα, HeI, [SII] and Li panels all show an expected outflow signal, but only the [SII] emission centroid profile changes sign at antiparallel positions.

As discussed above, SA allows astronomers to investigate structures below the diffraction limit of the telescope in use. There are certain steps that need to be taken to ensure that these signals are, in fact, real. There are several instrumental and systematic effects that can be introduced to observations which will mimic real signals to a high degree of accuracy. There have been several occurrences of artificial signals arising due to these effects, and consequently several methods of validating the authenticity of any signals present in spectro-astrometric analysis (Bailey 1998b; Brannigan et al. 2005; Takami et al. 2001; Whelan & Garcia 2008; Whelan et al. 2015).

There are two types of effects common in spectro-astrometry; *instrumental* and *systematic*. Instrumental effects include misalignment of spectrum with CCD columns, departure of CCD pixels from the regular grid, imperfect flat-fielding or charge transfer deficiencies. These can be removed by subtracting the anti-parallel PA as described in (Bailey 1998a,b) and Section 2.1, or by polynomial fitting (Davis et al. 2001, 2003; Garcia et al. 2000; Whelan et al. 2004). Systematic effects include unstable AO and telescope tracking errors, and can only be removed by PA subtraction.

In Figure 2.6, a perfect example of artificial signals which mimic the positional offset of a bipolar outflow is shown for the CTTS RU Lup. If analysis is completed only with perpendicular position angles, all 4 accretion tracers would be seen to show a signal, but in fact only the [SII] signal is not artificial, as all other accretion tracers do not change sign when analysed from anti-parallel PAs. Another indication that this signal is not real is the difference in displacement between the 0° and the 180° PAs. This shows a time variable nature in the effect causing the artefact, meaning it cannot be simply removed by PA subtraction.

The final condition to take into account when applying spectro-astrometry to a set of observations is the slit-width versus the seeing. Brannigan et al. (2005) show how a wide slit relative to the seeing can introduce a distortion in the wavelength of light hitting different parts of the diffraction grating, causing a shift in wavelength of the light when it reaches the detector, even though the incident light is of the same wavelength. This is most prevalent when the seeing is smaller than the slit width, and can introduce a distortion in the Gaussian nature of the PSF.

2.4.0.1 Centroid, FWHM and spatial resolution

The spectra are generally cut around the emission line to remove any telescopic artefacts. *Bplot* fits a Gaussian and Lorentzian function to each PSF, shown in Figure 2.7.

The Centre, Gaussian FWHM and Lorentzian FWHM for each wavelength increment are outputted into an splot.log file. This is then used in the *Python* routines to calculate the Voigt FWHM as per Equation 2.5 (An example of one of the scripts used can be found in Appendix A). The centroid value is then converted into spatial space by multiplication of 0.246 and 0.182 for the blue and red arms of UVES respectively. This value represents the spatial (or pixel) scale of UVES per pixel and is given in arcseconds. The centroid is then converted into milliarcseconds (mas) for convenience.

Initially, the *python* packages *SciPy* and *lmfit* were used to calculate the centroid and FWHM without the need to run the *bplot* task. This was achieved in much the same way as *bplot*, fitting the relevant function to each wavelength increment, and proved far more computationally efficient. Some discrepancies were noticed, however, and so the *bplot* version was run as a test. A comparison of the results is shown in Figure 2.8.

As expected, all five methods of centroid measurements show the exact same results, and the values have been incremented away from zero so they can be seen. Interestingly, while both Gaussian FWHM measurement methods provide the same results, the three
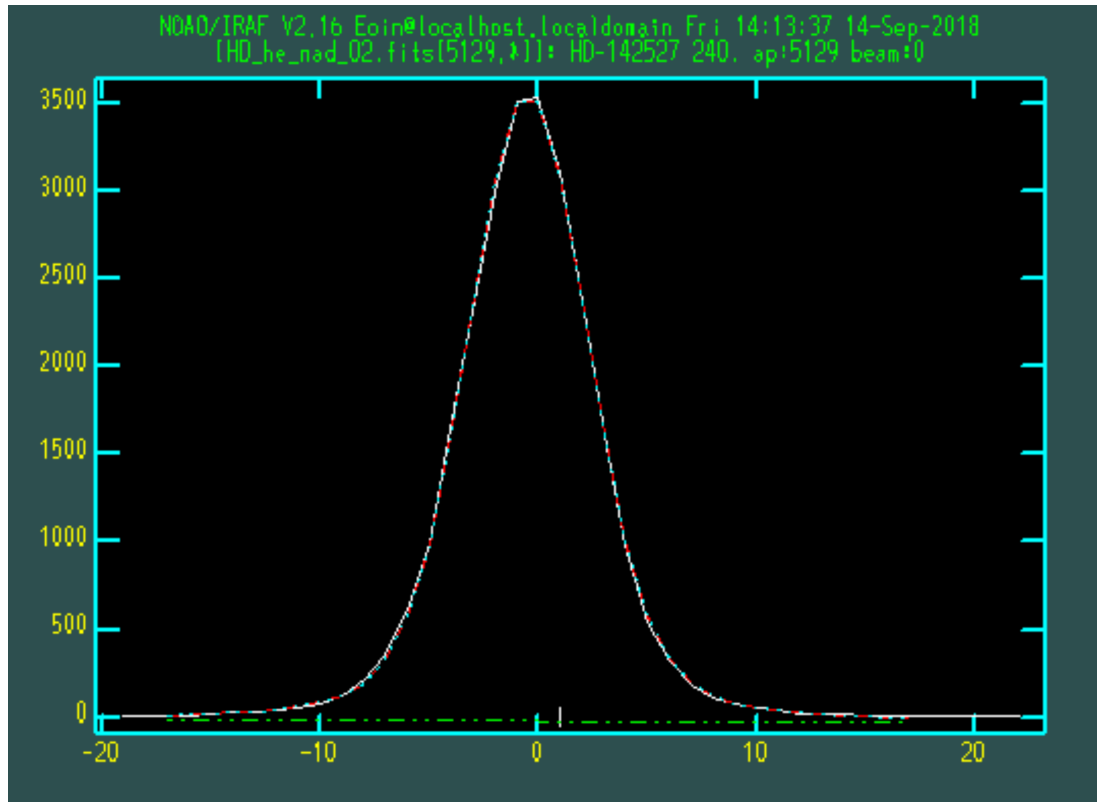
FIGURE 2.7: Screenshot of the final output of the *IRAF* task *bplot*. Each aperture represents a wavelength increment, so 5129 wavelength increments were processed in this example.

Voigt methods all differ from one another. However, as the shape remains the same, no information is lost regarding the origin of the emission.

Summary

Spectro-astrometry is a powerful technique by which high-precision spatial information can be extracted from a seeing limited spectrum. The technique involves the measurement of the centroid of the spatial profile, as a function of wavelength, to produce a so-called position spectrum. The precision to which the centroid can be measured is primarily dependent on the SNR. SA had been used to investigate a variety of objects from brown dwarf jets to quasars. Possible instrumental effects which can introduce false signals to a spectro-astrometric study are telescope tracking errors and unstable active optics. For a spectro-astrometric study it is common to observe the target with different slit PAs. Taking two observations at anti-parallel PAs allows one to confirm detected signals and thus rule out artefacts. Any real signal will invert between the two observations. An analysis of photospheric lines can also be used as a check for artefacts. The advantage of using perpendicular slit PAs is that it also enables the PA
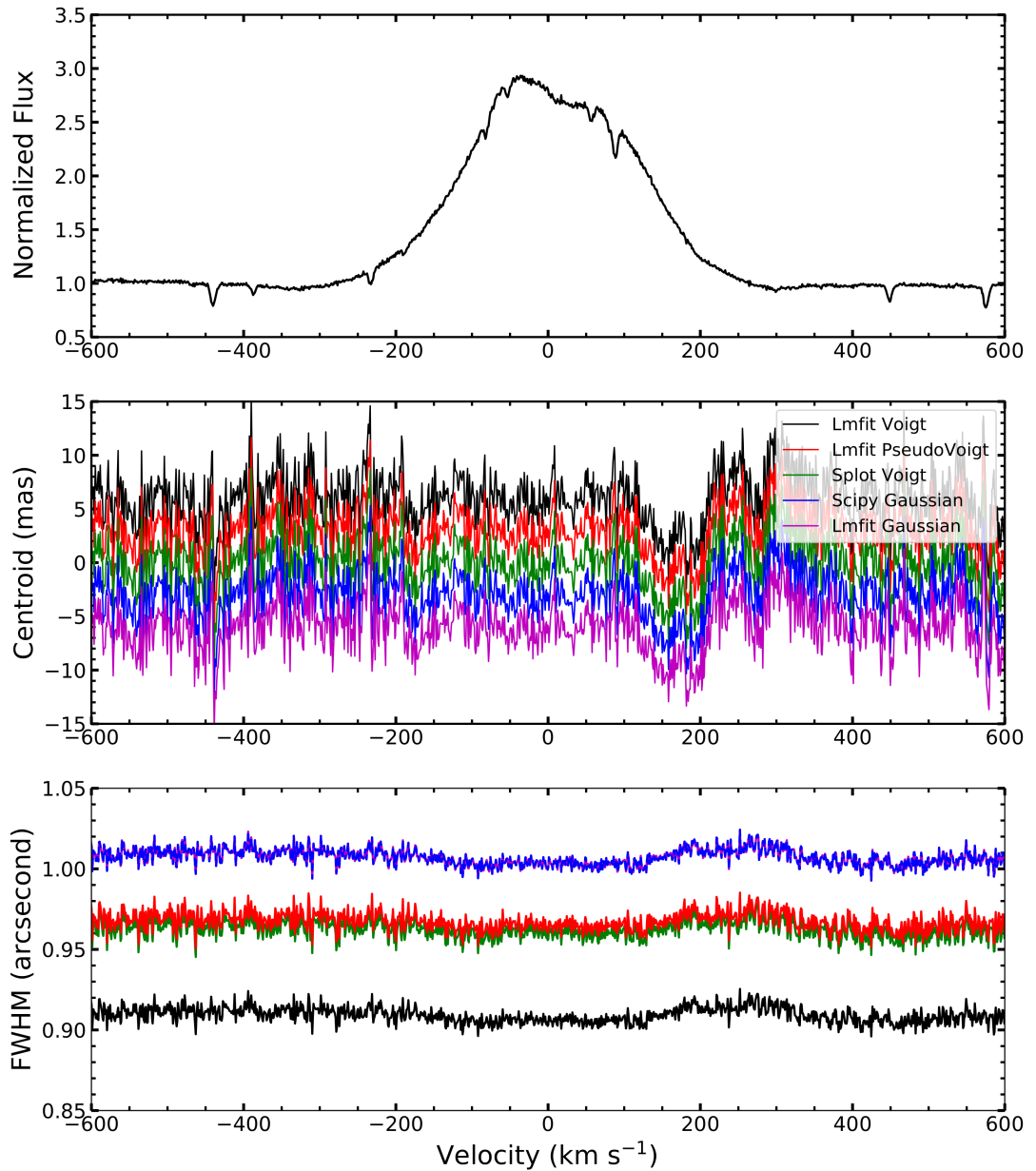
FIGURE 2.8: Comparison between the various packages available for centroid and FWHM calculations. The centroid measurements have been incremented away from zero, as all resulted in the same results. The FWHM values have not been changed.

of the feature under investigation (outflow or companion) to be mapped. A further consideration for any spectro-astrometry project is contamination by the continuum emission. This can be corrected for by subtracting the continuum from the emission line region under analysis or by considering that the extent of any measured offset is weighted by the ratio of the continuum to line emission. In this work it was found that a Voigt fit provided a better fit to the wings of the spatial profile than the Gaussian fit, therefore a Voigt fit was used at all times. A number of methods exist for calculating

the centroid and FWHM of the source spatial profile, and after comparison, it was determined that the *IRAF* routine *Bplot* gave the most accurate results, although the differences were negligible in most cases.

Chapter 3

Observations and Data Reduction

This section provides a description of the instrument with which all observations were taken, UVES, and provides the steps taken in reducing the observations via the ESO Data File Organiser *GASGANO* and their VLT Instrument Pipeline. A comparison of the different packages available for fitting functions to the position spectra used in spectro-astrometric analysis concludes the chapter.

3.1 UVES

All observations of both T Cha and HD 142527 were taken from the Ultraviolet and Visual Echelle Spectrograph (UVES) of the VLT located at the Nasmyth B focus of the UT2 Kueyen Telescope (Dekker et al. 2000). UVES is a cross-dispersed echelle spectrograph which provides good spatial information as well as high resolution across the wavelength scale. Figure 3.1 shows the configuration of UVES and its different modes. The observations all focus on the wavelength range of 5000 - 7000 Å, with a spectral resolution of R $\sim$ 40000. This translates to a velocity resolution of 7.5 kms^{-1}. For all observations, the red mode was used, which sends light down the red path to CCD#3. Observations using the red optical path have two corresponding output files, designated l and u for the lower and upper chips respectively. The lower covers 5000 - 6000 Å and the upper 6000 - 7000 Å. The pixel scale provided by UVES is given in the $.fits$ file headers as 0.246 arcseconds per pixel for the blue arm, and 0.182 arcseconds for the red arm.
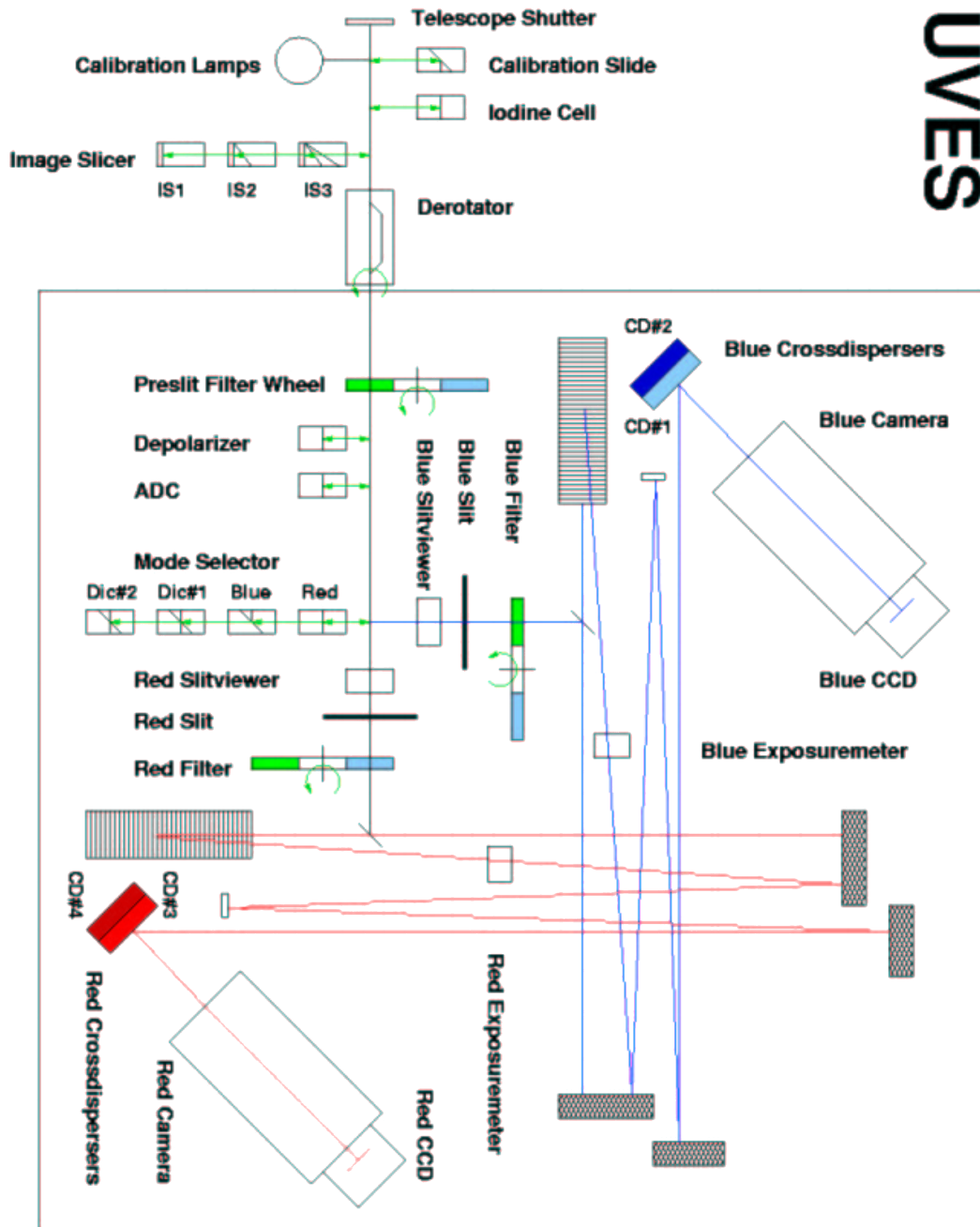
FIGURE 3.1: Diagram of the UVES spectrograph. Image taken from the UVES User manual at www.eso.org.

3.2   Data Reduction

For each of the observation nights of T Cha shown in Table 4.1, a set of calibration files were taken, generally before or after the observations took place. For this dataset, the ESO program *GASGANO* was used to reduce the observations. This program is freely available at http://www.eso.org/sci/software/gasgano.html. The steps involved in creation of master calibration files are outlined below:

1. Load files into *GASGANO* so they can be sorted by program id. *GASGANO* will automatically sort files into PAs and epochs as seen in Figure 3.2. It will also supply standard tables needed in later steps.
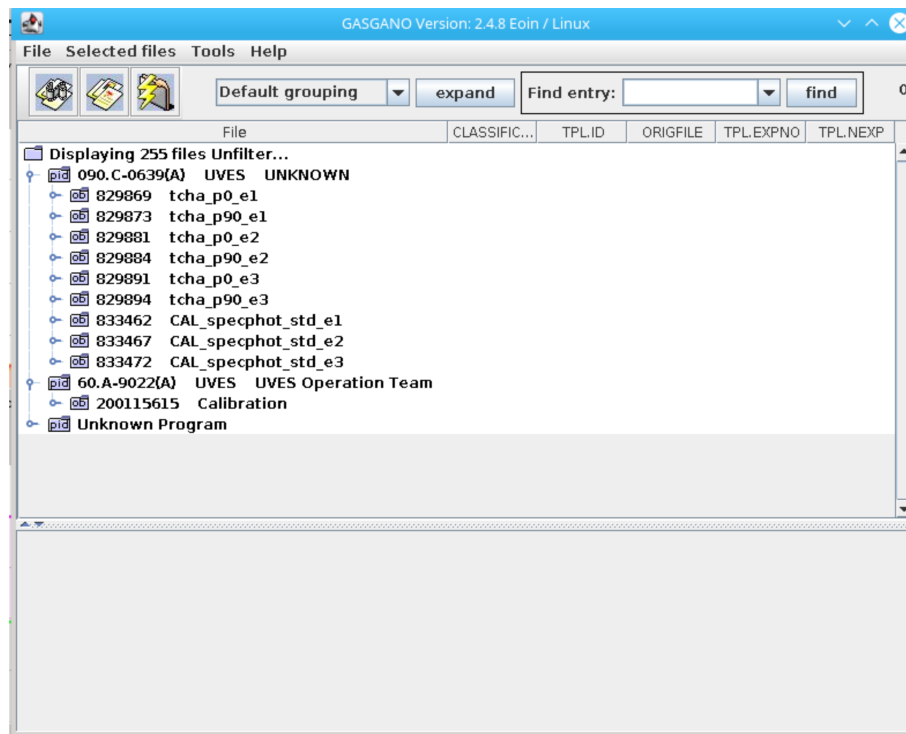
FIGURE 3.2: Screenshot depicting the automatic filtering and sorting of fits files in *GASGANO*.

2. Once the files are loaded into *GASGANO*, select the bias frames corresponding to a set of science images and send these files to *uves_cal_mkbias*. In this project we are using the red arm of UVES, so all calibration files are tagged with *_RED* after their primary designation, as seen in Figure 3.3. The bias frames are median combined into two final calibration files, one for each chip.

3. the format check exposure, classified as *ARC_LAMP_FORM_RED*, is then sent to the recipe *uves_cal_orderpos* along with a Thorium Argon (ThAr) line reference
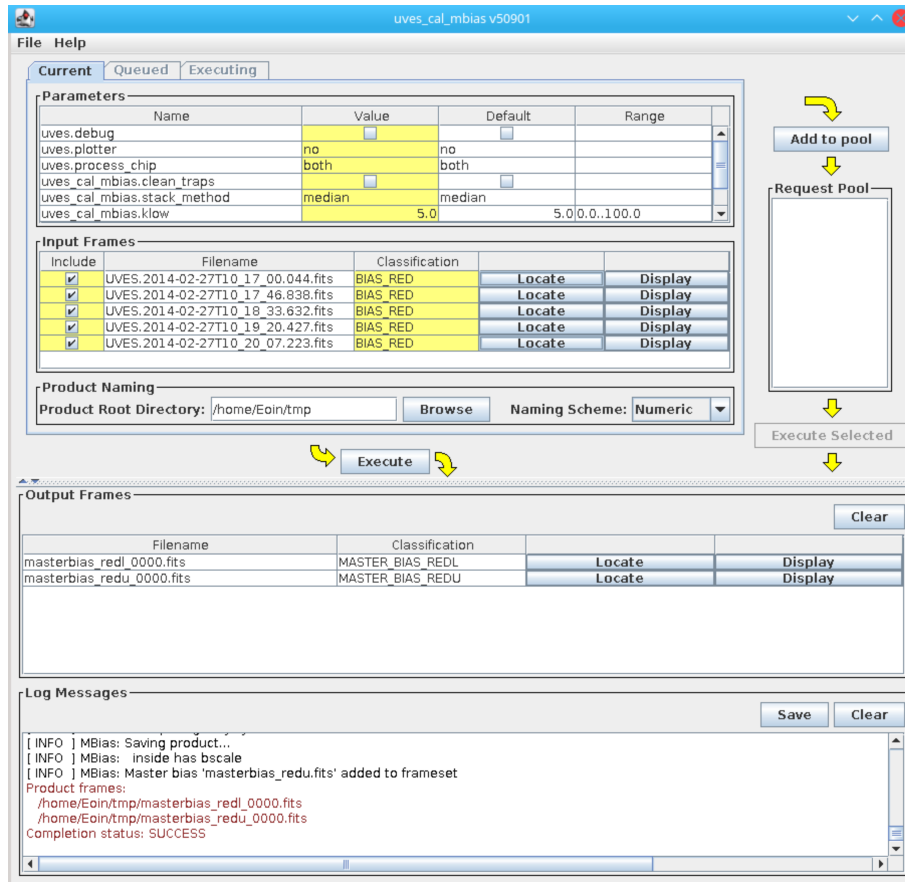
FIGURE 3.3: Screenshot of the output from *GASGANO* upon completion of bias calibration.

table identified by the tag *LINE_REFER_TABLE*. This recipe uses the location of known ThAr lines to automatically fit a first-guess dispersion relation. Successive iterations continue until most lines have been identified. The products are a guess line table and guess order table per chip., as seen at the bottom of Figure 3.4

4. Narrow (0.5") order definition flats are taken using a continuum flat lamp. The flats are used to define the order positions in an echelle image, initially detected with a Hough transformation. The orders are traced and finally fitted with a global polynomial. The flats are classified *ORDER_FLAT_RED* and are sent to the recipe *uves_order_pos* (Figure 3.5) along with the order guess tables produced in the previous step. This produces two order tables for use in the science reduction process.

5. Wavelength calibration frames, classified as *ARC_LAMP_RED*, are taken with a long slit and the ThAr lamp. These are sent to the recipe with the guess-line, wavelength catalogue and order tables to fit a final dispersion. A Gaussian function is used to fit the fainter lines not found using the format check executed
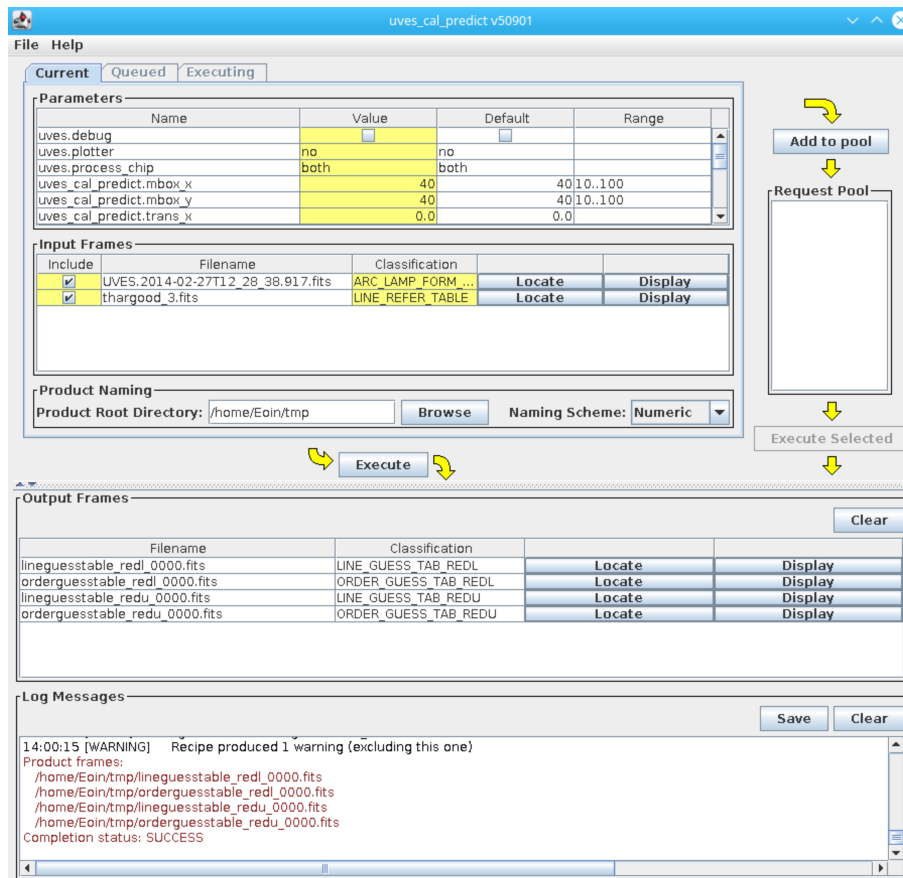
FIGURE 3.4: Screenshot of the first-guess dispersion fitting in *GASGANO* reduction process.

previously. The output is a finalized line table for each chip. The output is shown in Figure 3.6.

6. The flat field frames are long slit images of the continuum flat lamp. They approximate the blaze function, as well as measuring the fixed-pattern noise and fringing in the red. The flats are master-bias subtracted, exposure corrected, medianed and finally background subtracted. a master dark may also be added for subtraction after the flats are median combined. This results in a master flat frame for each chip. As in Figure 3.7, the products of this recipe are two flats and two background flats, one for each chip.

7. Normally, a standard star taken the same night as the observations at the same seeing is sent ot the *uves_cal_response* recipe. It undergoes the same process as the science frame, using the same calibration files, but outputs a relative flux calibration curve used to flux-calibrate the science observations. The curve is then binned to 50 Å resolution, with one response curve for each chip. For our observations, the standard star was not close enough to a reference star in the
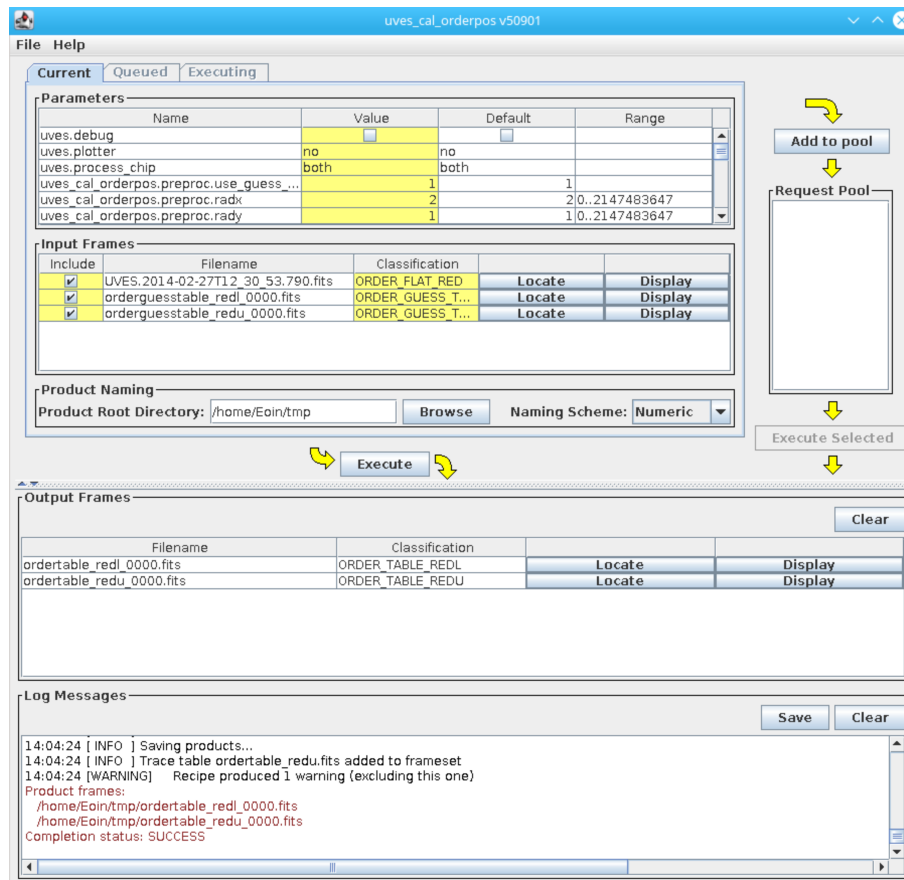
FIGURE 3.5: Screenshot of the output of the recipe *uves_order_pos*.

FLUX_STD_TABLE, so the UVES Master Response curves were used. More information on these can be found at https://www.eso.org/observing/dfo/quality/UVES/qc/SysEf

Once the calibration steps are complete, the science observations are run through the recipe *uves_obs_scired*. The steps involved in the process are as follows:

1. Bias subtraction
2. Dark subtraction (optional)
3. Background subtraction
4. Cosmic-ray removal
5. Flat field correction
6. Wavelength rebinning
7. Sky subtraction
8. Order merging
9. Response correction (If response curve is provided)

The two extraction methods used in this project are outlined below:
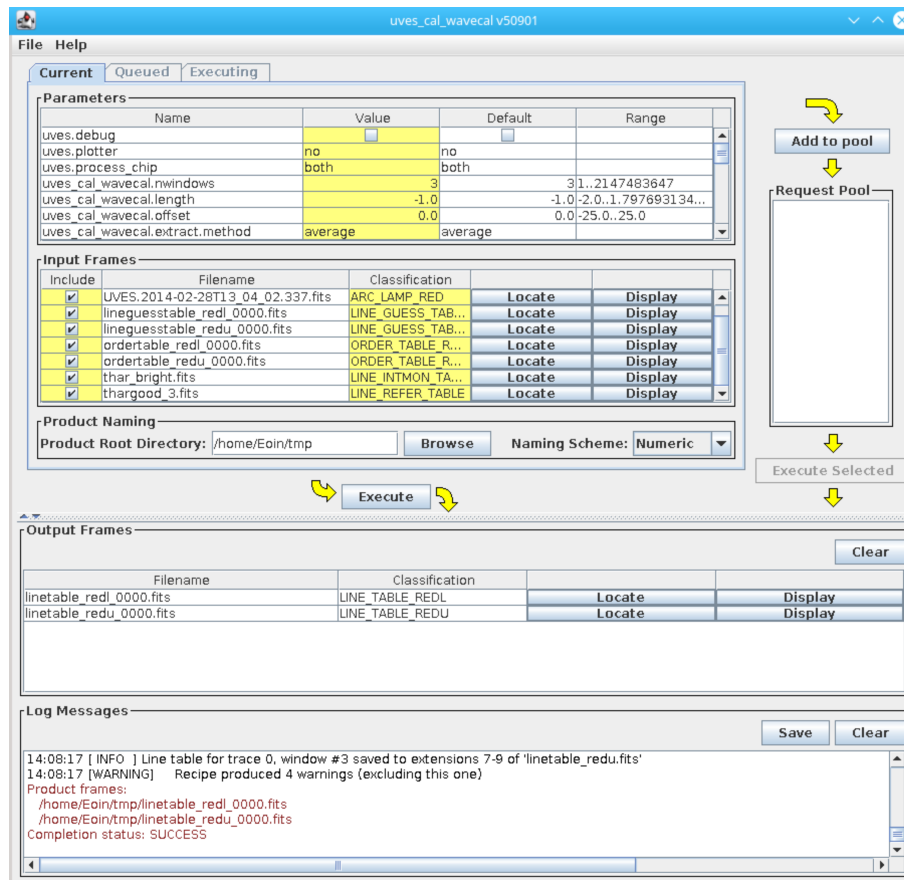
FIGURE 3.6: Screenshot of the wavelength calibration output.

2d: The 2d extraction method runs through the steps outlined above until it reaches response correction. As the Master Response curves are 1d, they cannot be used to flux calibrate 2d spectra. Instead, the recipe performs a rebinning of the flux into a two-dimensional wavelength-slit coordinate grid. Our investigation of Hα do not require flux calibration, and the preservation of spatial information allows spectro-astrometry to be applied to our observations.

Optimal: Optimal extraction fits a Gaussian function to the cross-dispersion flux distribution. The weighted flux per bin is then derived from the fitting profile, which undergoes chi-squared minimization. Cosmic rays cause a strong deviation from a Gaussian distribution, and so are recognized and removed. Sky emission lines are also removed during the optimal extraction method as they fill the whole slit, contributing to the linear term of the spatial profile, but do not contribute to the extracted total intensity. The output of a 1d optimal extraction is shown in Figure 3.8, and this method is used to study the line profiles of important emission lines such as [O I]λ 6300. More information on the optimal extraction algorithm can be found in Horne (1986); Marsh (1989); Mukai (1990)
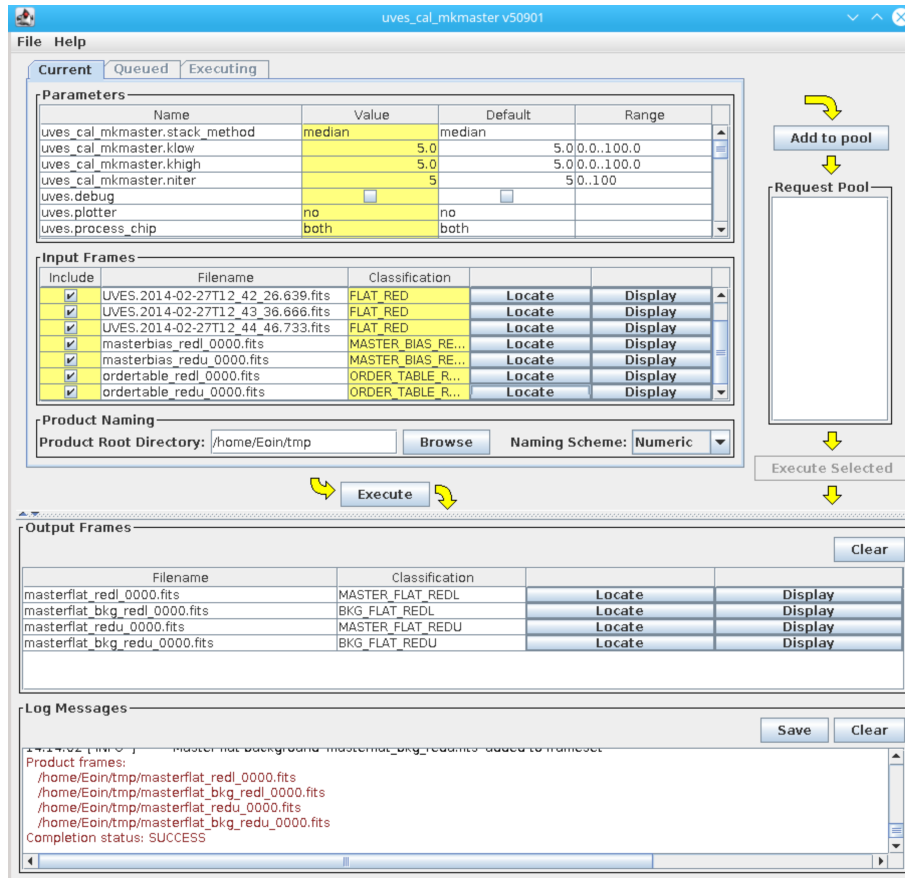
FIGURE 3.7: Screenshot of the output of flat-fielding recipe for *GASGANO*.

For the observations of HD 142527 listed in 5.1, the data was reduced using the ESO Pipeline for UVES, version 5.8.2. This program automates the steps outlined above, and as for T Cha, both 1d and 2d spectra were generated for further analysis.

Figure 3.9 shows the setup screen for the UVES pipeline, with the actors highlighted in yellow. These act in the same way as the corresponding recipes in *GASGANO*, with different parameters available for configuration depending on the desired output. Once the parameters have been configured, the pipeline will automatically run through all the steps necessary. The resulting spectra are shown on a data visualisation application (if one is configured in the initial stages) such as *ds9* or *Fv*.

Summary

Both observations of T Cha and HD 142527 were taken with the Ultraviolet and Visual Echelle Spectrograph on the VLT. For pipeline reduction, both the *GASGANO* and *EsoReflex* programs were used. The 1d product of the pipelines were used for RV
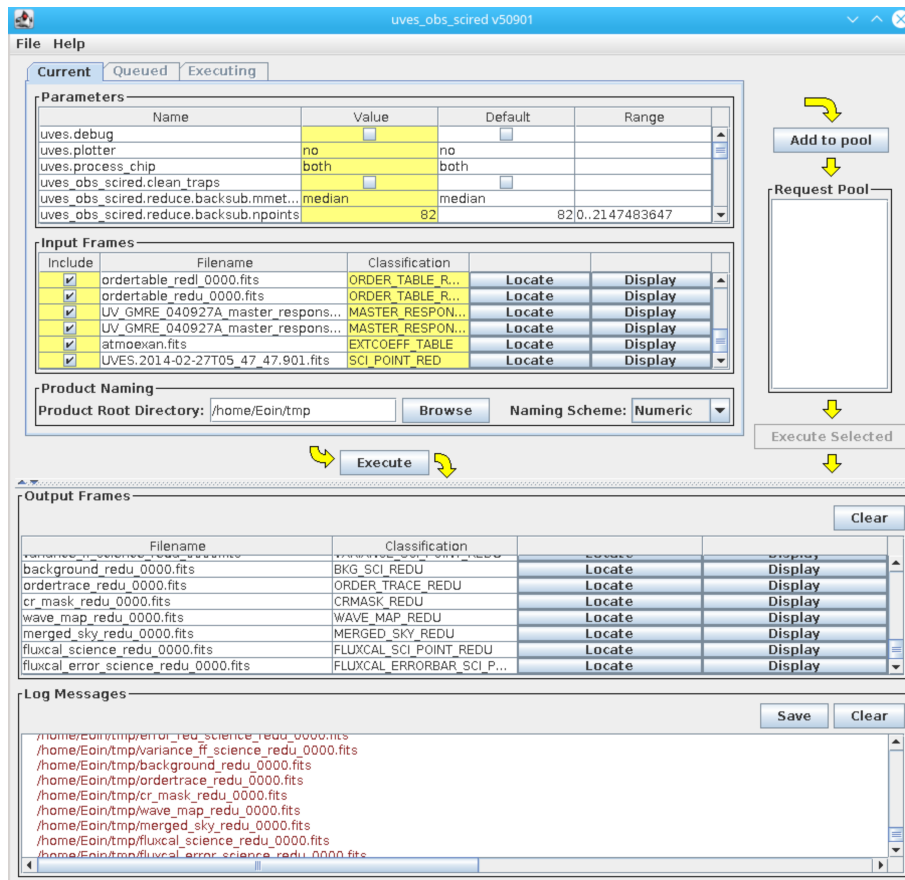
FIGURE 3.8: Screenshot of the final output of the science reduction steps, with all master calibration files used in combination with an extinction coefficient table. The output files will change depending on which extraction method was used to reduce the data. The above image is of a 1d reduction run, as the master response curves were included in the recipe.

corrections and emission line flux calculations, and the 2d products are used for spectro-astrometric analysis.
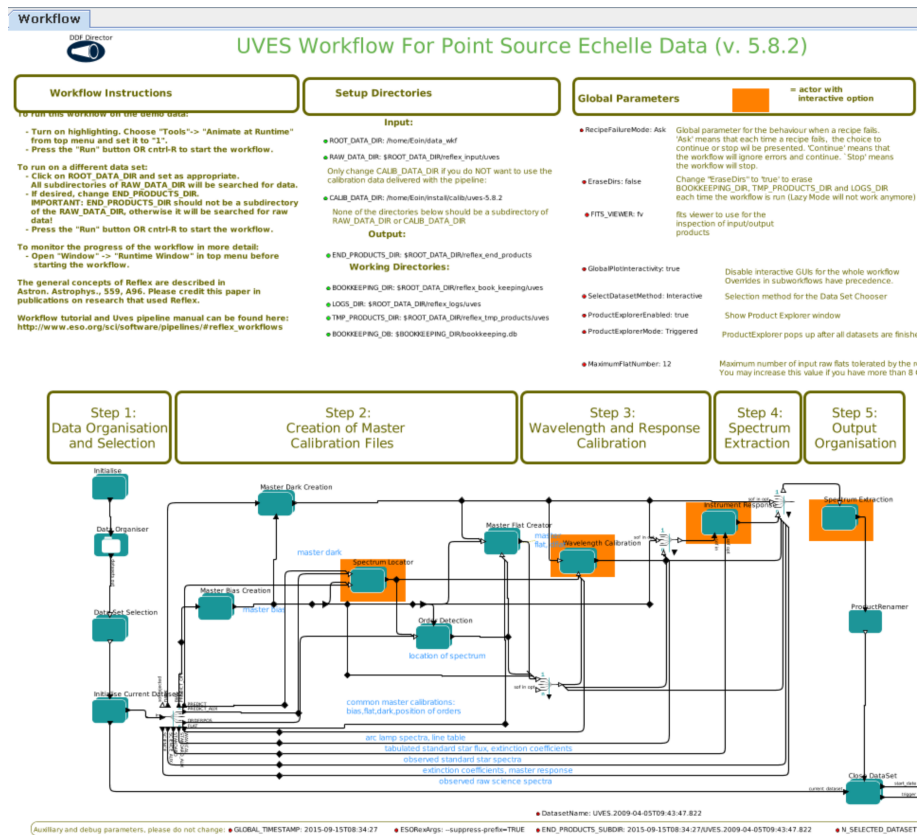
FIGURE 3.9: Screenshot of the ESO Reflex pipeline workflow for UVES. EsoReflex is freely available at http://www.eso.org/sci/software/esoreflex

Chapter 4

UVES Spectroscopy of T Chamaeleontis: Line Variability, Mass Accretion rate and Spectro-astrometric Analysis

This section describes the star T Cha, and aims to provide results of the spectro-astrometric analysis as well as some stellar parameter calculations. This is followed by a summary and discussion of the results obtained. T Cha was chosen as a good candidate for this spectro-astrometric study due to the strong possibility that its inner disk contains a planetary companion and because of its remarkable Hα variability. As the clumpy structures proposed to be responsible for the line variability orbit closer to the star than the forming planet, any Hα emission from a forming planet should be easier to detect during a period of obscuration of the inner circumstellar zone. Specifically, our goal here is to test if a contribution from the possible exoplanet T Cha b can be detected using SA. Figure 4.1 shows an ALMA image of T Cha in which the gap between the disk and the central area can clearly be seen. It is within this gap that we hope to detect signals form T Cha b.

4.1 Target

T Cha is a T Tauri type variable star with a TD (Hendler et al. 2018; Schisano et al. 2009). It is a member of the ε Cha Association (d $\sim$ 110 pc (Gaia-Collaboration et al. 2018)). Its age is given as 7 Myr by Torres et al. (2008) and its mass, radius and
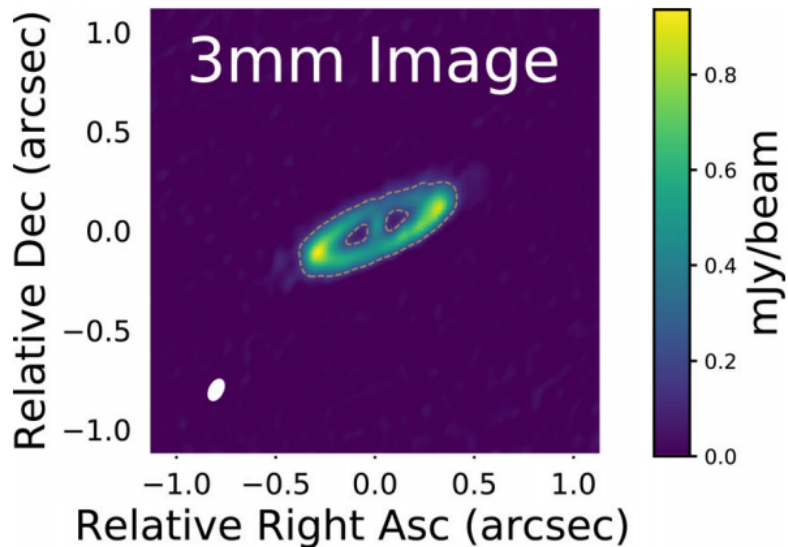
FIGURE 4.1: ALMA 3mm cleaned image of T Cha with the beam shown as an elliped in the bottom left corner. The contour shown covers a 5σ accuracy level taken from Hendler et al. (2018).

spectral type are estimated to be 1.3 $M_\odot$, 1.8 $R_\odot$ and G8 respectively (Schisano et al. 2009). Schisano et al. (2009) show that T Cha is still actively accreting and calculate $\dot{M}_{acc}$ to be ~ 4 x 10^{-9} $M_\odot$ yr^{-1} using the 10% width of the Hα line. The inclination and PA of the T Cha accretion disk are $\approx 73 \pm 5^o$ and $113°$ respectively (Huelamo et al. 2015; Pohl et al. 2017). The accretion disk has been found to be composed of an inner optically thick disk ranging from 0.13 au - 0.17 au (Olofsson et al. 2013), and an outer dust disk radius of > 80 au (Huelamo et al. 2015). These two disks are separated by a gap and it was first proposed that this gap housed a substellar companion (T Cha b) by Huelamo et al. (2011). Hendler et al. (2018) present ALMA observations of T Cha
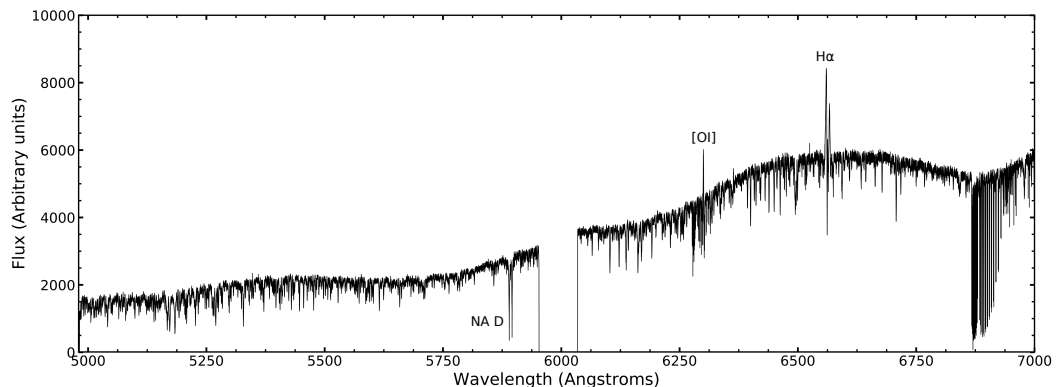
FIGURE 4.2: The full UVES spectrum of T Cha in epoch 2 with the prominent lines marked. The spectrum is split into two parts: the lower section with a wavelength range of $\approx$ 5000 - 6000 Å and the upper section with a wavelength range of $\approx$ 6000 - 7000 Å

49

which reveal the gap to have a width of between 18 au and 28 au. They conclude that the most likely explanation for their observations is that embedded planets are acting to carve out the dust gap. They estimate that if T Cha's gap were caused by a single planet the planet's mass would be ~ 1.2 M$_{Jup}$. The conclusions of Hendler et al. (2018) support the results of Pohl et al. (2017) who present modelling of VLT/SPHERE data.

A further notable feature of T Cha is the extreme variability of its emission line spectrum. Schisano et al. (2009) report strong variability in the main emission lines (Hα, Hβ and [O I]λ 6300) which correlates with variations in visual extinction of over three magnitudes. The prominent emission lines of this dataset are noted in Figure 4.2, showing the spectrum of T Cha for epoch 2. Both the shape and strength of the lines are variable with the Hα line profile changing from pure emission to nearly photospheric absorption over a timescale of days. Schisano et al. (2009) argue that variable circumstellar extinction could be responsible for both the variations in the stellar continuum flux and for the corresponding changes in the emission lines. They propose that clumpy structures, containing large dust grains and orbiting the star within a few tenths of au, would episodically obscure the star and, eventually, part of the inner circumstellar zone. The observed radial velocity changes in the star reported by Schisano et al. (2009) would support this scenario.

4.2   T Cha Observations

Spectra were obtained with UVES with a spectral range of $\sim$ 500 to 700 nm and a spectral resolution of R $\sim$ 40000 (Dekker et al. 2000). The strategy was to obtain spectra at anti-parallel and/or perpendicular slit PAs to check for artefacts in the spectro-astrometric signature (Brannigan et al. 2005) and to recover the PA of the planetary companion. Four epochs of data were considered to allow the effect of the T Cha's variability on the chances of detecting a planet to be investigated (Whelan et al. 2015). Table 4.1 gives details on the observations which make up each epoch including the slit PAs used. Epoch 1 consists of UVES observations of T Cha taken in May 2012 (Program 089.C-0299 (A)) from the ESO archive, while epochs 2 to 4 consists of UVES observations taken in February and March 2014 (Program 090.C-0639(A)). The datasets were initially reduced using the ESO program *GASGANO* for UVES.

Epoch	Slit PA (^{o})	Date	Time (UT)	Obs time (s)	Seeing (")
1	67	2012-05-02	02:58	300	1.01
		2012-05-02	03:04	300	1.11
		2012-05-02	03:10	300	1.06
		2012-05-02	03:16	300	1.10

Epoch	Slit PA (^{o})	Date	Time (UT)	Obs time (s)	Seeing (")
		2012-05-02	03:21	300	1.15
1	247	2012-05-02	03:36	300	0.76
		2012-05-02	03:42	300	0.76
		2012-05-02	03:48	300	0.89
		2012-05-02	03:54	300	0.86
		2012-05-02	03:59	300	0.87
1	157	2012-05-02	04:13	300	0.76
		2012-05-02	04:19	300	0.76
		2012-05-02	04:25	300	0.77
		2012-05-02	04:31	300	0.80
		2012-05-02	04:37	300	0.86
1	337	2012-05-02	04:50	300	0.79
		2012-05-02	04:55	300	0.78
		2012-05-02	05:01	300	0.74
		2012-05-02	05:07	300	0.85
		2012-05-02	05:13	300	0.90
2	0	2014-02-28	05:47	600	0.89
		2014-02-28	06:26	600	1.22
		2014-02-28	06:49	600	0.93
		2014-02-28	07:00	600	1.23
		2014-02-28	06:10	600	1.28
		2014-02-28	07:21	600	1.09
		2014-02-28	07:32	600	1.06
		2014-02-28	07:43	600	1.25
2	90	2014-02-28	07:56	600	0.94
		2014-02-28	08:07	600	0.96
		2014-02-28	08:18	600	1.09
		2014-02-28	08:29	600	0.94
		2014-02-28	08:40	600	0.96
		2014-02-28	09:01	600	1.06
		2014-02-28	09:12	600	0.94
		2014-02-28	09:23	600	1.05
3	0	2014-03-04	04:14	600	1.05
		2014-03-04	04:25	2304	1.28
		2014-03-04	04:59	3598	1.24
		2014-03-04	06:00	1652	1.25
		2014-03-04	06:29	260	1.19
3	90	2014-03-04	06:45	1000	1.27
		2014-03-04	07:03	1000	1.23
		2014-03-04	07:20	1000	1.26
		2014-03-04	07:38	2000	1.33
		2014-03-04	08:17	2000	1.45
4	0	2014-03-09	02:21	600	1.01
		2014-03-09	02:32	600	1.17
		2014-03-09	02:43	600	1.09
		2014-03-09	02:53	600	1.05
		2014-03-09	03:04	600	1.14
		2014-03-09	03:15	600	1.14
		2014-03-09	03:26	600	0.97
		2014-03-09	03:37	600	1.07

Epoch	Slit PA (^{o})	Date	Time (UT)	Obs time (s)	Seeing ('')
		2014-03-09	05:42	600	0.95
		2014-03-09	05:53	600	0.84
		2014-03-09	06:04	600	0.96
		2014-03-09	06:14	600	0.86
		2014-03-09	06:25	600	0.78
		2014-03-09	06:36	600	0.72
		2014-03-09	06:47	600	0.90
4	90	2014-03-09	03:50	600	0.98
		2014-03-09	04:00	600	1.04
		2014-03-09	04:11	600	1.00
		2014-03-09	04:22	600	1.14
		2014-03-09	04:33	600	1.08
		2014-03-09	04:44	600	0.89
		2014-03-09	04:54	600	1.19
		2014-03-09	05:05	600	1.44
		2014-03-09	07:04	600	1.26
		2014-03-09	07:15	600	1.27
		2014-03-09	07:26	600	1.12
		2014-03-09	07:36	600	1.11
		2014-03-09	07:47	600	1.28
		2014-03-09	07:58	600	1.18
		2014-03-09	08:09	600	1.15
		2014-03-09	08:20	600	1.28

TABLE 4.1: Full log of UVES observations of T Cha. The seeing values are corrected for airmass. In epoch 2, PA 0, the observation times fluctuated considerably as the target was lost for an unknown length of time.

4.2.1 Post-processing

Once the science images have been reduced into 1d and 2d spectra, they must be corrected for photospheric lines. Only the NaD and [O I]λ 6300 line profiles are contaminated by photospheric absorption features in the 1d spectra. The Hα line profile is unaffected for T Cha (Simon et al. 2016).

The spectra were corrected for photospheric absorption using the TTS V2246 Oph, another K0 spectral type star. The photospheric correction for the [O I]λ 6300 line follows the technique of Simon et al. (2016). First, a 20 Å cut centred around λ 6300 is made on both the object and the photospheric standard to approximate a flat continuum. Then the standard is aligned with the object by cross-correlation, and the emission lines of the standard broadened if needed. The standards absorption features would usually be reduced by a factor matching the veiling (r_λ, representing how much of the photospheric lines are filled in by continuum excess emission), but as found in Schisano et al. (2009), T Cha appears to have no continuum excess emission. Finally

the photospheric standard was divided into each of the spectra using the iraf task *telluric* to give a flux calibrated spectrum free from photospheric contribution. This is shown in Figure 4.3.
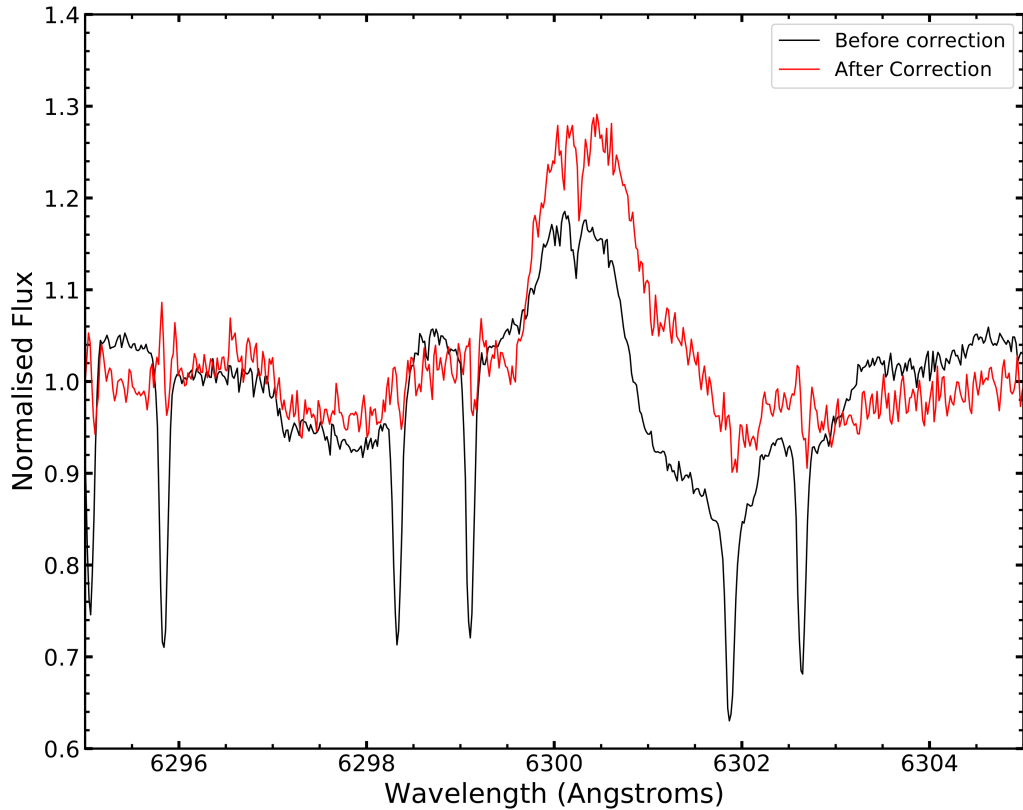
FIGURE 4.3: Image showing the uncorrected spectrum in black, and the corrected spectrum in red. The TTS V2246 Oph was used as a standard in the removal of the photospheric lines as its spectral shape is very similar to that of T Cha. The spectra shown are of the [O I]λ 6300 line from epoch 3, PA 90°.

Due to the variability of T Cha it is important to account for extinction in order to obtain flux values with the highest possible accuracy. For T Cha, this consists of both visual and photospheric extinction, caused by both the gas still accreting onto the star and for periods where some of the disk is obscuring our line-of-sight.

In order to calculate the extinction, the observation in which Hα is fully in absorption was selected. This corresponds to T Cha being in its brightest state, with the continuum from the star covering up most of the emission from Hα. This gives us a starting A$_V$ value, taken as 1.2 from Schisano et al. (2009). All observations were normalized to 6349 Å, and the additional A$_V$ value required to minimize residuals between the other observations and our template are noted in Table 4.2. It should be noted that the [O I]λ 6300 values in Table 4.2 are not extinction corrected, as the [O I]λ 6300 emission does not originate from inside the photosphere, but comes from the stellar

Epoch and PA	A_V	V_{rad} (kms^{-1})	L_{line} (x 10$^{-5}L_\odot$)	Mag (R band)
E1-67	1.2	14.9	3.0 ± 0.1	8.73
E1-157	1.1	14.5	4.1 ± 0.1	8.47
E1-247	1.2	14.5	4.4 ± 0.1	8.84
E1-337	1.4	14.2	4.3 ± 0.1	8.68
E2-0	1.9	14.5	1.1 ± 0.1	9.89
E2-90	1.9	14.3	1.1 ± 0.1	9.63
E3-0	1.5	14.9	0.8 ± 0.1	10.1
E3-90	1.4	15.0	1.2 ± 0.1	9.69
E4-0	1.7	14.7	1.2 ± 0.1	9.5
E4-90	1.7	14.7	1.3 ± 0.1	9.43

TABLE 4.2: Extinction estimates for the different epochs. Radial velocities, line luminosities and magnitudes for the [O I]λ 6300 line. The error in the radial velocity measurements is 0.1 km s^{-1}. The R band magnitudes were calculated at 6349 Å.

wind of T Cha. The extinction values are used for the calculation of the Hα emission from T Cha b in Section 4.3.6.

In Figure 4.4 an example of this process is shown. For this case, the black line representing the 90° PA has already been corrected to the chosen standard, which was the PA of 67° in epoch 1. The red line representing epoch 3 must have its A_v value increased until the residual value is at its lowest point. In this case, the red spectra needed an A_v value of 1.85 to reduce residuals to their minimum.

The R-band magnitude values are also shown in Table 4.2 and the variability of the star can be seen in the difference between the highest value of 10.1 and lowest value of 8.47, when the star was at its brightest. These were also calculated at 6349 Å, as it is the central wavelength of the R band. The Line luminosities shown were calculated using equation 4.2 shown in Section 4.3.5.

The extinction of HD 142527 is much lower, and not as variable as for T Cha. Also, a lack of observations preclude the use of the method detailed for T Cha. Therefore, an extinction value of 0.6 A_V was applied to all spectra as per the calculations of Verhoeff et al. (2011). This represents the extinction due to the ISM and the circumstellar material surrounding the star.

4.3 Results

In this section, results of spectro-astrometric analysis of the emission lines identified in the observations is presented. The lines analysed are Hα, [O I]λ 6300 and the NaD lines respectively.
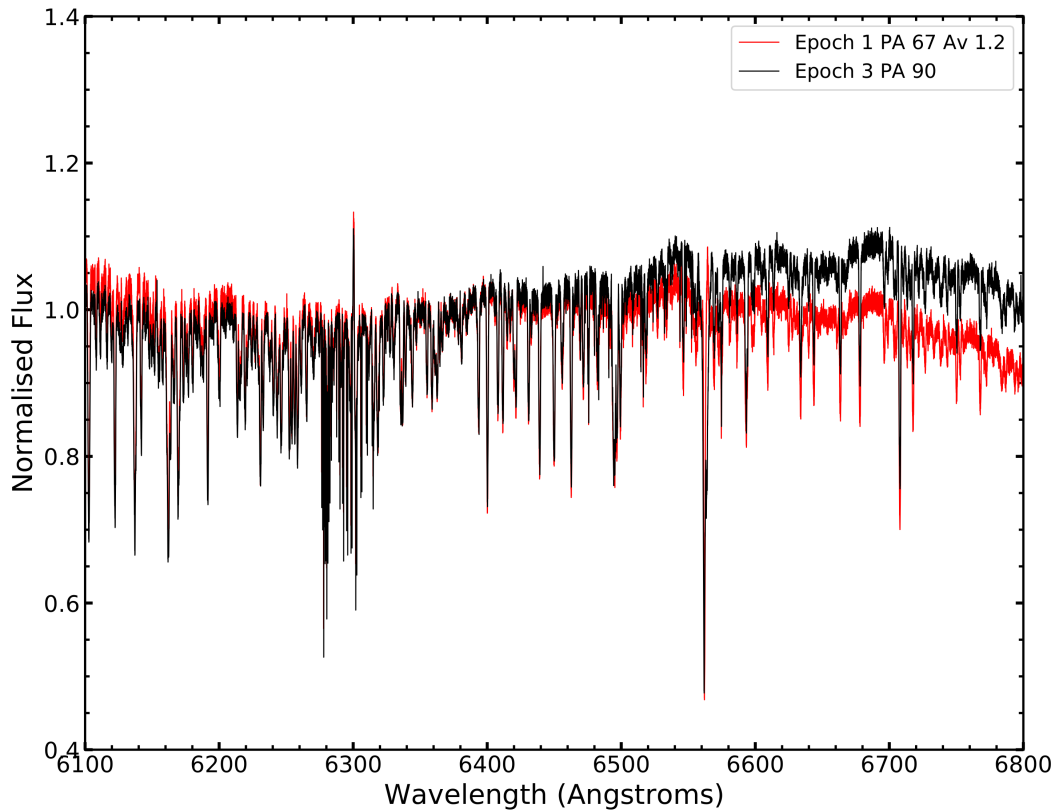
FIGURE 4.4: Figure showing how the extinction calculation was completed on the normalised Hα line profile of T Cha.

4.3.1 Spectro-astrometric Analysis

As discussed in Chapter 3, spectro-astrometry was applied to the main emission lines in the wavelength range. T Cha was chosen as a good candidate for this spectro-astrometric study due to the strong possibility that its inner disk contains a planetary companion orbiting at > 20 au (Hendler et al. 2018). As the clumpy structures proposed to be responsible for the line variability orbit closer to the star than the forming planet, any Hα emission from a planet in formation should be easier to detect during a period of obscuration of the inner circumstellar zone.

Initially, all of the spectra were reduced using *gasgano* or the *reflex* pipeline and analysed. Signals were detected in some of these spectra in Hα and so the observations were reduced by hand as a check to the efficacy of pipeline reduction. Hand reduction here means the observations were reduced using *IRAF* routines. What follows are results from the hand-reduced spectra. All spectra were corrected for RV measurements calculated via cross-correlation described in Section 4.3.4. Each spectrum has also been corrected for heliocentric RV.

4.3.1.1 Hα

In this section, results of the Hα analysis are presented. Figures 4.5, 4.6, 4.7 and 4.8 show the median combined normalised flux, spatial centroid and FWHM for each epoch. Then the 4 epochs are presented together in Figure 4.9 to highlight variability, and finally a discussion on the use of binning will follow.

The general shape of the Hα emission profile remain the same throughout the observations that make up the individual epochs. This allows the observations to be combined in order to reduce SNR. Regardless, each observation is checked before combination to ensure no signals are being averaged out of the final product. The Hα line profiles are also shown in Figure 4.9, and the variability inherent in this line is clear. It is clearly seen going from showing some emission in epoch 2 to being dominated by absorption in epochs 1, 3 and 4. Schisano et al. (2009) explain these changes in the Hα line as being due to the obscuration of T Cha by the occulting clumps and thus the suppression of the stellar continuum flux. Consequently, when the stellar continuum flux is at its lowest more of the Hα line region is seen in emission. It is also likely that a significant part of the Hα emission is obscured by the occulting clumps. Both accretion shocks and a stellar wind will contribute to the Hα emission (Whelan et al. 2014a), however it is not clear what fraction of the Hα emission originates close enough to the star to be obscured.

Figure 4.5 shows the results for epoch 1. The spectrum has been continuum normalised and corrected for the source radial velocity. The line profile of Hα in this epoch is one of absorption with a width of only ~ 225 km s^{-1}. This epoch corresponded to the lowest average magnitude and highest average flux level, with the continuum level ~ 6 x 10^{-13} erg/s/cm^2 after extinction correction. Another interesting note is that this epoch corresponds to images taken in 2012, whereas the other 3 epochs are all within two months of each other in 2014, and this may be a reason it has twice as strong a continuum level. The centroid shows no deviation from zero beyond the 3-σ detection limit and the FWHM remains constant with an average value of 0.6 arcseconds, consistent with the seeing value for these observations.

Figure 4.6 shows that the Hα in epoch 2 has the largest amount of emission of all the epochs. Even so, there are two absorption features centred at -50 and +50 km s^{-1} the line profile in this epoch is much broader than the one seen in epoch 1, ranging from -300 to +300 km s^{-1}.

Figure 4.7 shows the line profile during which T Cha was in its most quiescent state. If we were to detect a spectro-astrometric signal, epoch 3 would be the most likely
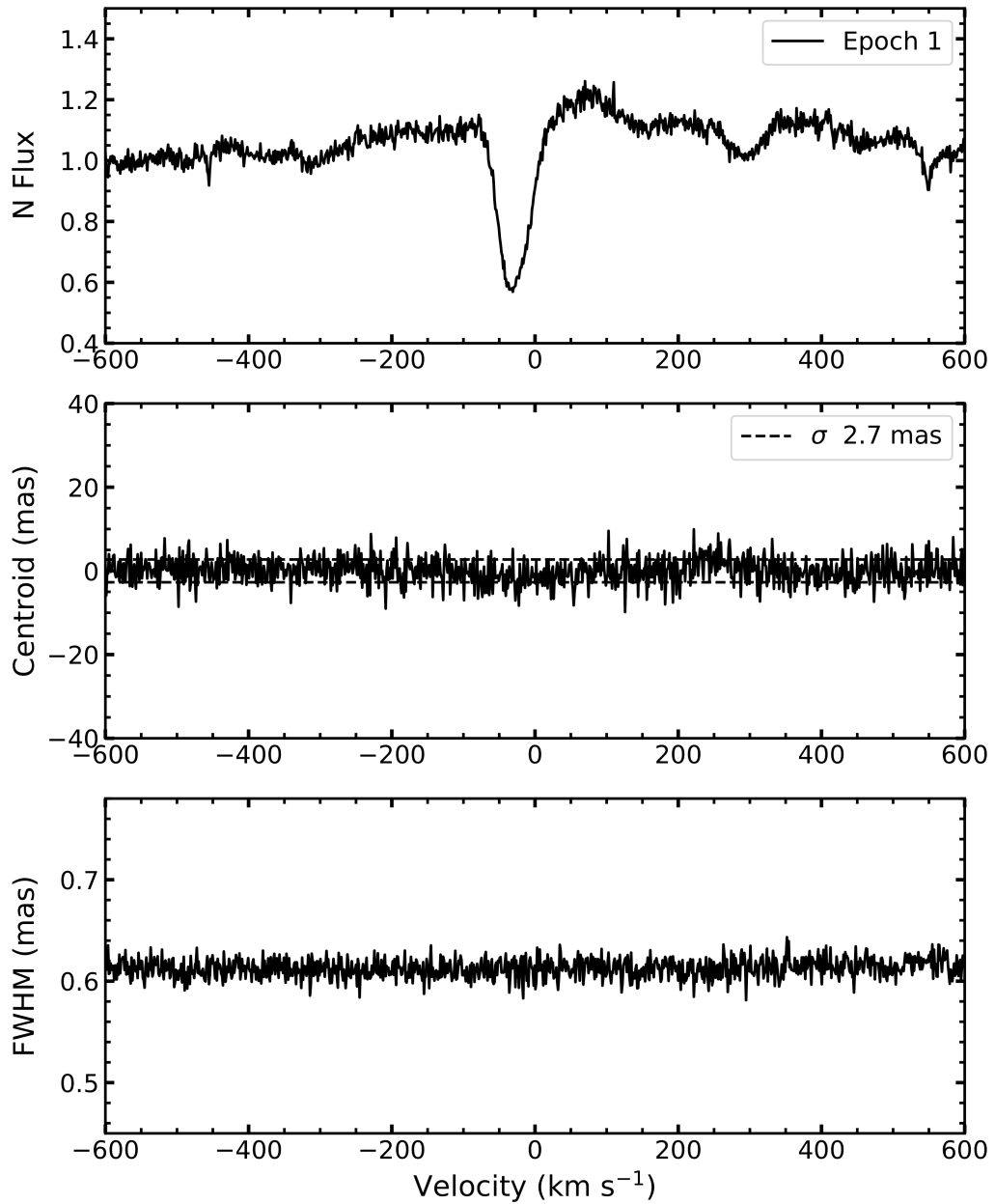
FIGURE 4.5: Results for epoch 1. The normalised Hα line profile, centroid and FWHM is a combination of the orthogonal and anti-parallel PAs listed in Table 4.1, containing 20 observations in total.

candidate, with the continuum level at its lowest amongst all the epochs. This means that a contribution from a companion is most likely to be noticeable against the parent continuum level.

Figure 4.8 shows an interesting line profile with both red and blue-shifted absorption and a blue shifted emission feature at $+250 \text{ km s}^{-1}$. The line profile is $\sim 450 \text{ km s}^{-1}$ in width, the second largest below epoch 2. The centroid shows only minor fluctuations
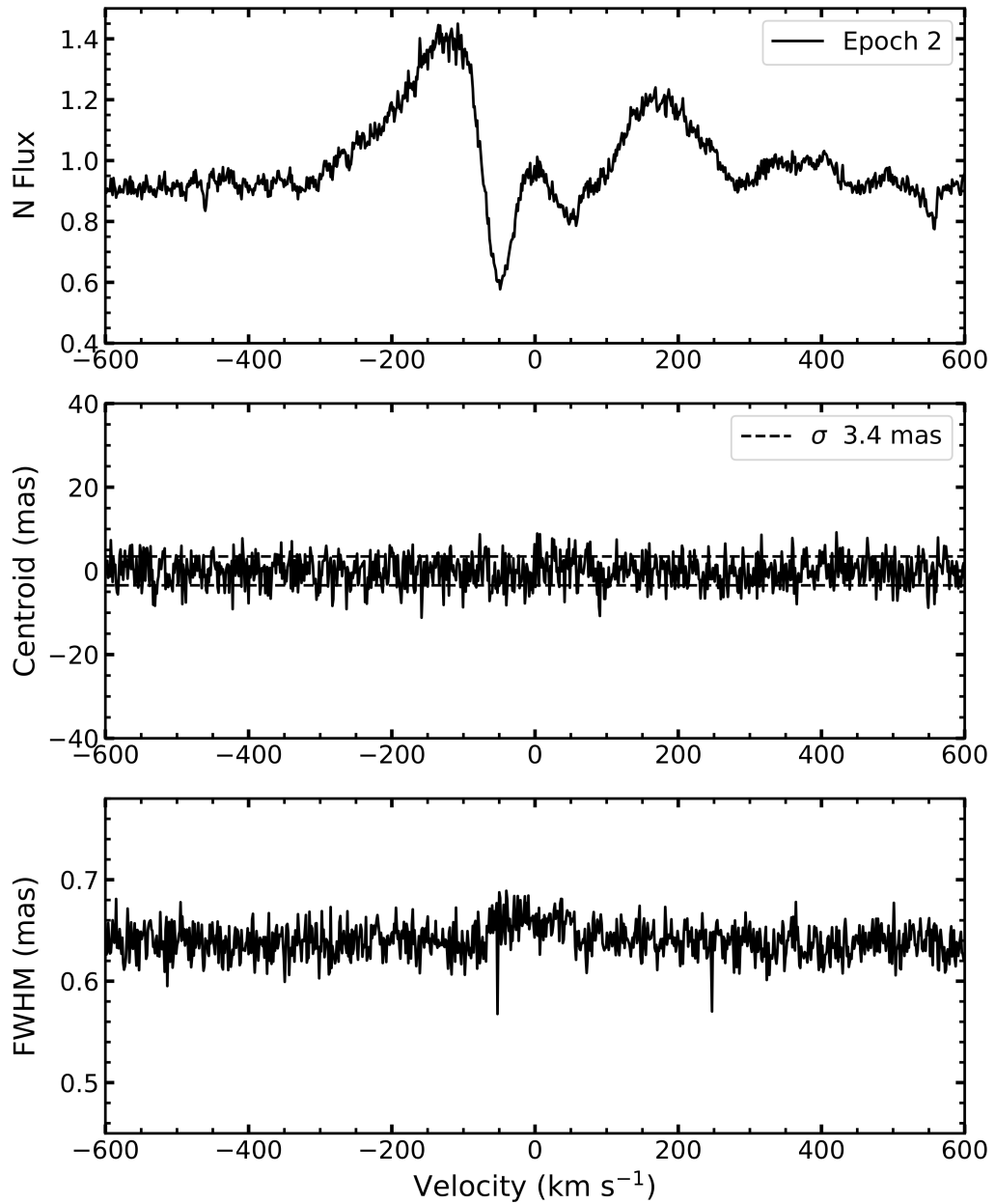
FIGURE 4.6: Figure showing the spectro-astrometric results for epoch 2. The spectrum shown consists of the normalised Hα line profile, centroid and FWHM which are a combination of the two PAs noted in Table 4.1, each consisting of 8 individual observations.

away from zero most prominent at -50 km s^{-1}. The FWHM value is lower and more tightly grouped than average due to the number of observations that were combined to produce this spectra, increasing the SNR.

In Figure 4.9 a summary of each epoch is shown together for comparison. Epochs 1, 3 and 4 show some slight deviations around the centroid, but again nothing reaching
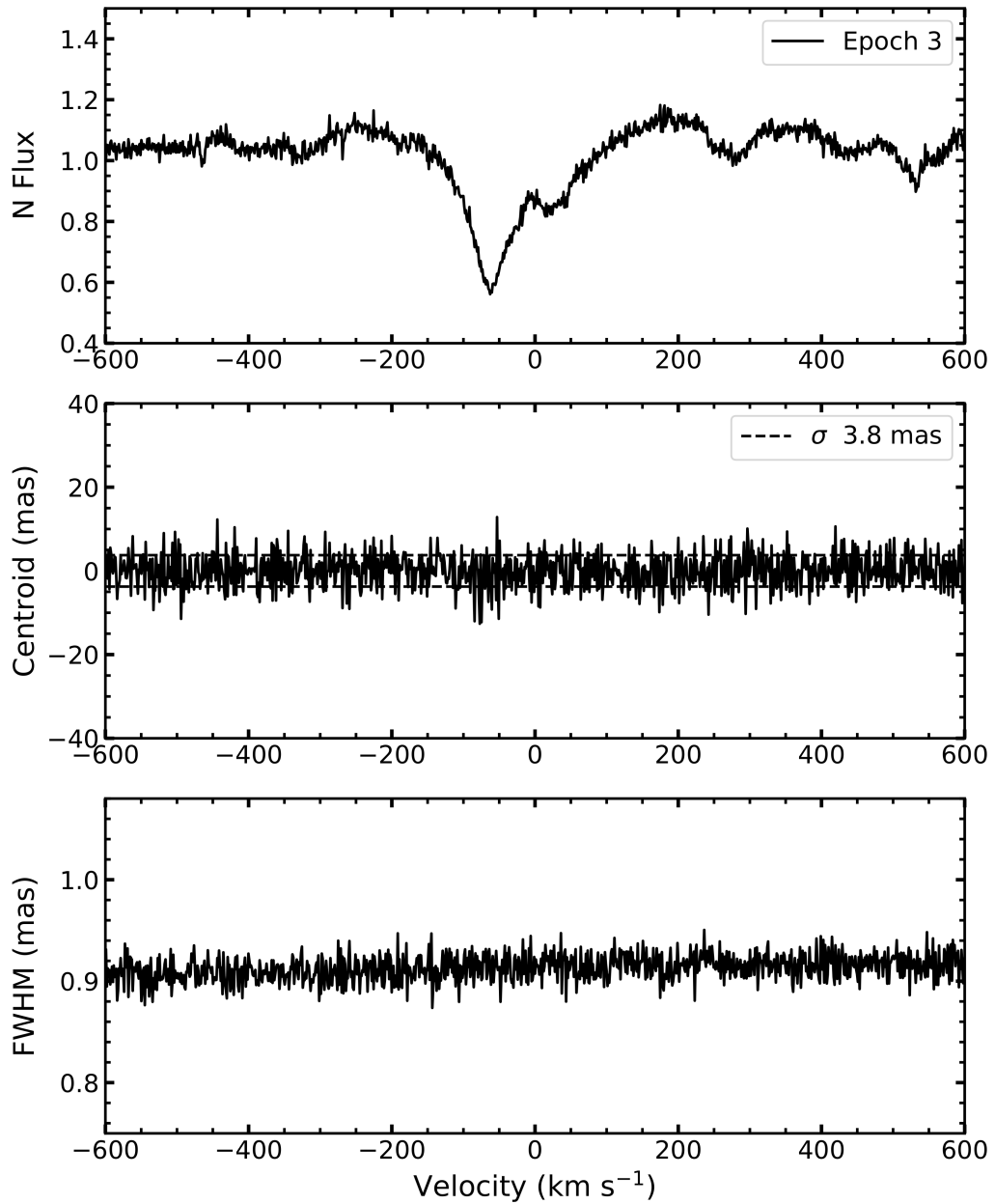
FIGURE 4.7: Figure showing the spectro-astrometric results for epoch 2. The spectrum shown consists of the normalised Hα line profile, centroid and FWHM which are a combination of the two PAs noted in Table 4.1, each consisting of 5 individual observations.

a 3-σ level. The FWHM of epoch 3 is higher than the average value of ∼ 6.5 mas as this epoch had the worst average seeing, giving a lower SNR. The flux level of epoch 3 is also the lowest from our data, giving rise to the higher FWHM as the intensity peak is not as sharp as the observations with high flux levels.
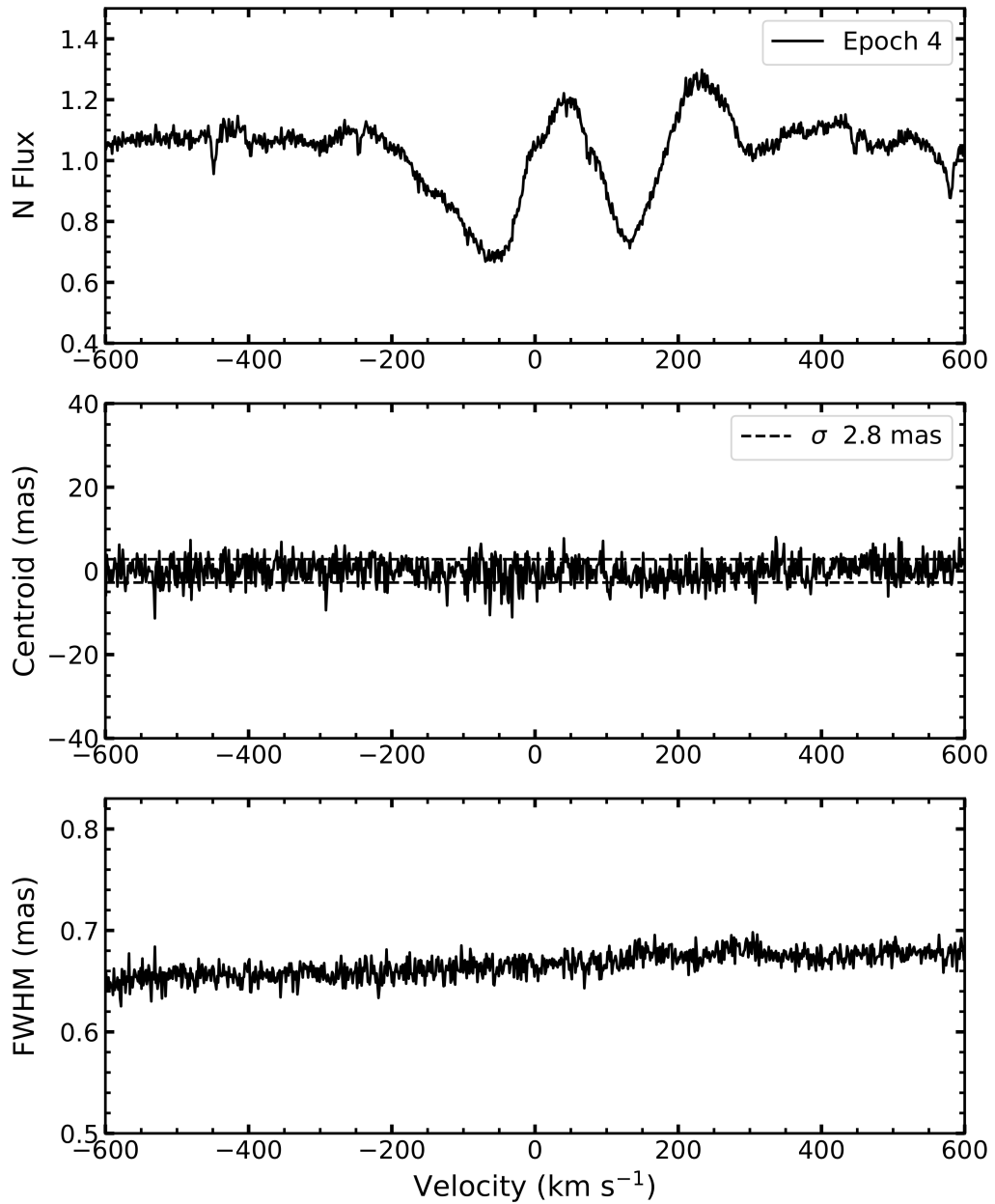
FIGURE 4.8: Figure showing the spectro-astrometric results for epoch 4. The spectrum shown consists of the normalised Hα line profile, centroid and FWHM which are a combination of the two PAs noted in Table 4.1, each consisting of 16 individual observations.

Several different binnings were also tested to increase the S/N and thus spectro-astrometric accuracy. The size of the binning which is appropriate is set by the width in velocity of the emission line region which is under investigation and the spectral resolution of the instrument. For TTS the accretion cutoff for the width of the Hα line is generally set at 270 km s^{-1} with a width of 200 km s^{-1} adopted for substellar objects (Jayawardhana et al. 2003). If we assume the same accretion criterion for planetary
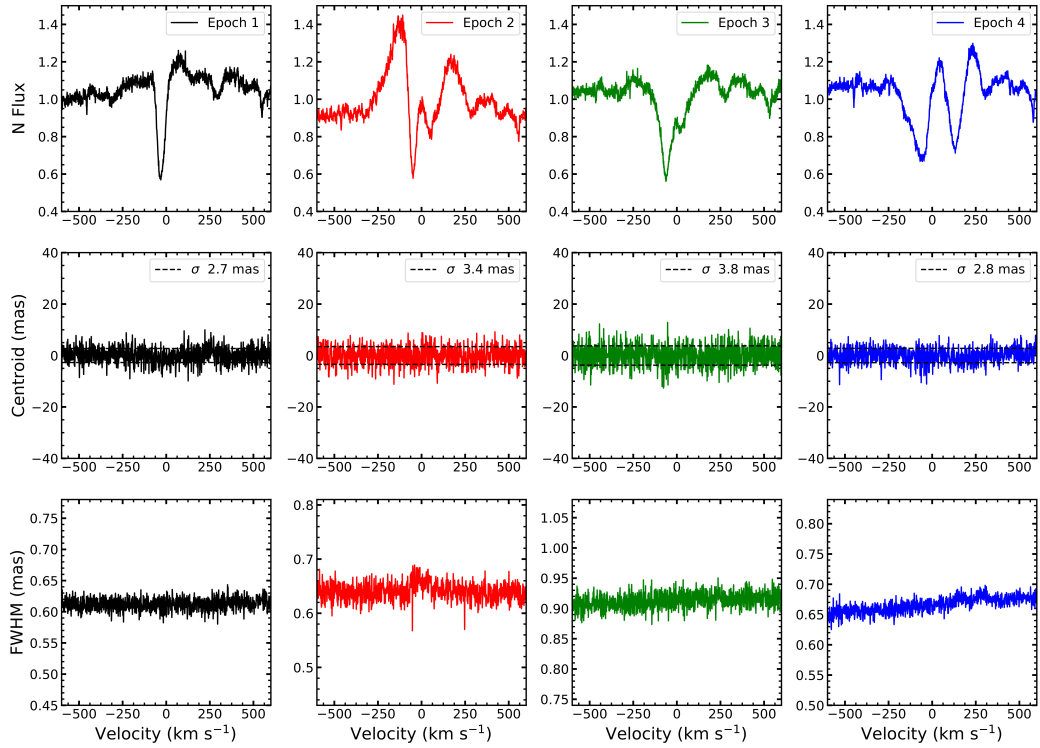
FIGURE 4.9: Combined normalised Hα line profiles, centroids and FWHMs for each epoch.

mass objects a bin of 40 would increase the spectro-astrometric accuracy to ~ 0.5 mas while providing a sampling of 5 points across a Hα line of width 200 km s^{-1}. The velocity resolution of the UVES spectra is ~ 7.5 km s^{-1}.

Figure 4.10 shows the binned spectra for the 4 epochs. The centroid y-axes have been reduced to ± 8 mas to better observe the centroid fluctuations and their σ levels. Each has been binned by a factor of 40 as discussed above, and several features can be seen outside of the 1-σ limit.
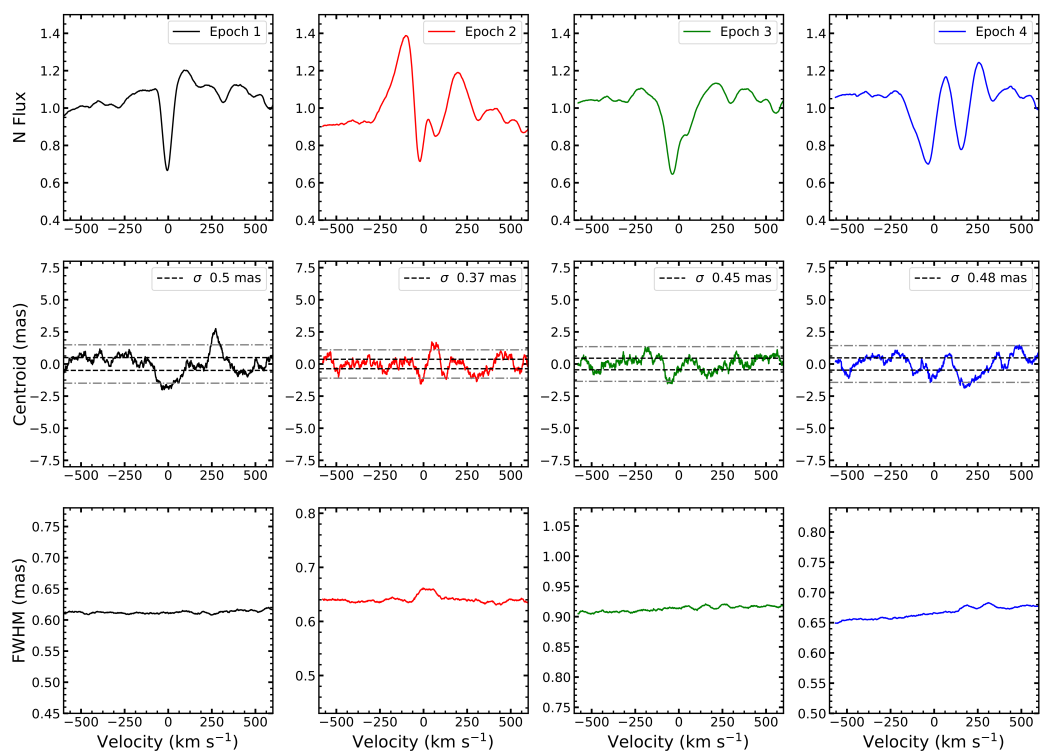
FIGURE 4.10: Binned line profile, centroid and FWHM of the 4 epochs. The 1- and 3-σ values are shown in black and grey lines respectively.

4.3.1.2 [O I]λ 6300 Å and NaD

In this subsection we present spectro-astrometric results of the [O I]λ 6300 and Na D lines. For both of these lines, no signals are expected from T Cha b. The low velocity component (LVC) of the oxygen line is known to originate in stellar wind, with the high velocity component (HVC) indicating the presence of bipolar outflows. As T Cha b is substellar, no wind is expected, and bipolar outflows have not been detected for such low mass objects. T Cha itself does not show any bipolar outflows. Both its estimated age of 7 Myr and its low radial velocity support this, as it has most likely already evolved past the stage of outflow.
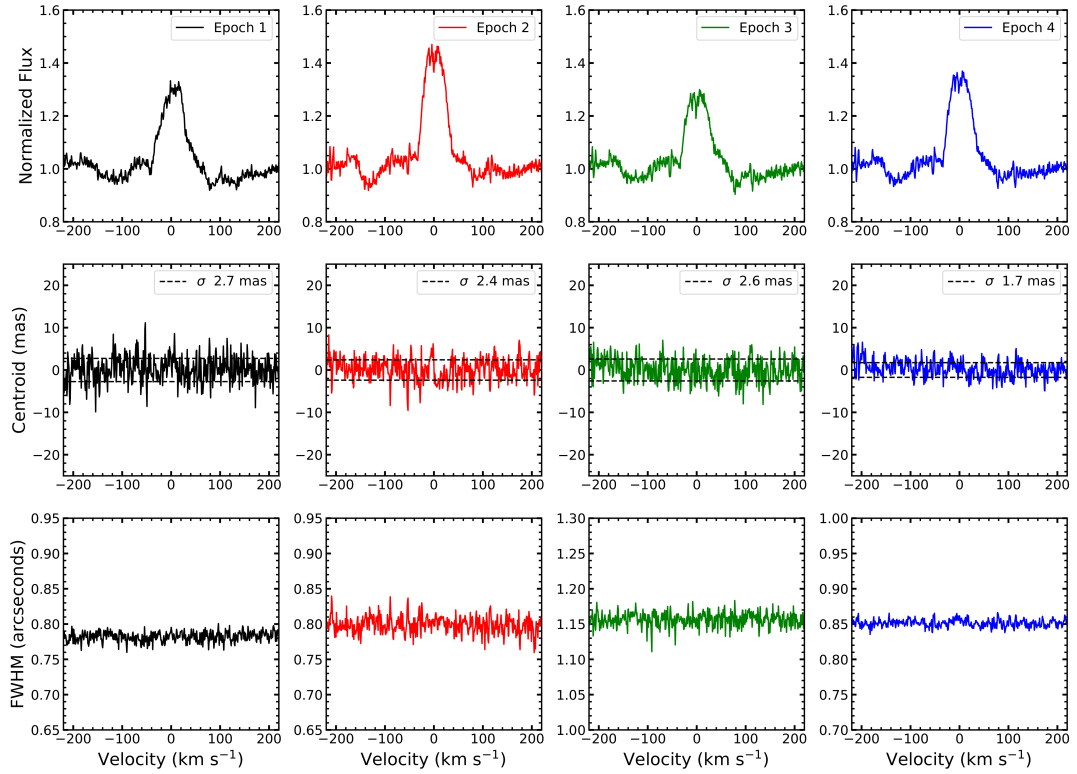
FIGURE 4.11: Normalised flux, centroid and FWHM values around the [O I]λ 6300 line in each epoch. Photospheric lines have been left in the spectra due to their irrelevance in centroid measurements.

As shown in Figure 4.11 the oxygen line remains constant in shape, with the intensity of the line varying slightly between epochs. For epoch 1, the line does not exhibit strong emission, even thought the overall flux level is highest in this epoch. This is most likely due to the variability of the star itself. Much as the Hα line profile of this epoch is in absorption, we see a weaker emission than in epoch 2 and 4, where the Hα line profiles also show some signs of emission, with epoch 2 being strongest in both Hα and [O I]λ 6300 emission. Thus, there does appear to be a correlation between line

emission strength, as opposed to the continuum flux level. As a baseline, the data from Table 2 in Schisano et al. (2009) has been plotted to show the expected correlation. The black line is the average and the dashed lines represent the 1-σ deviation from the average. The red points representing this dataset lie well within the standard deviation, if a little on the lower side.
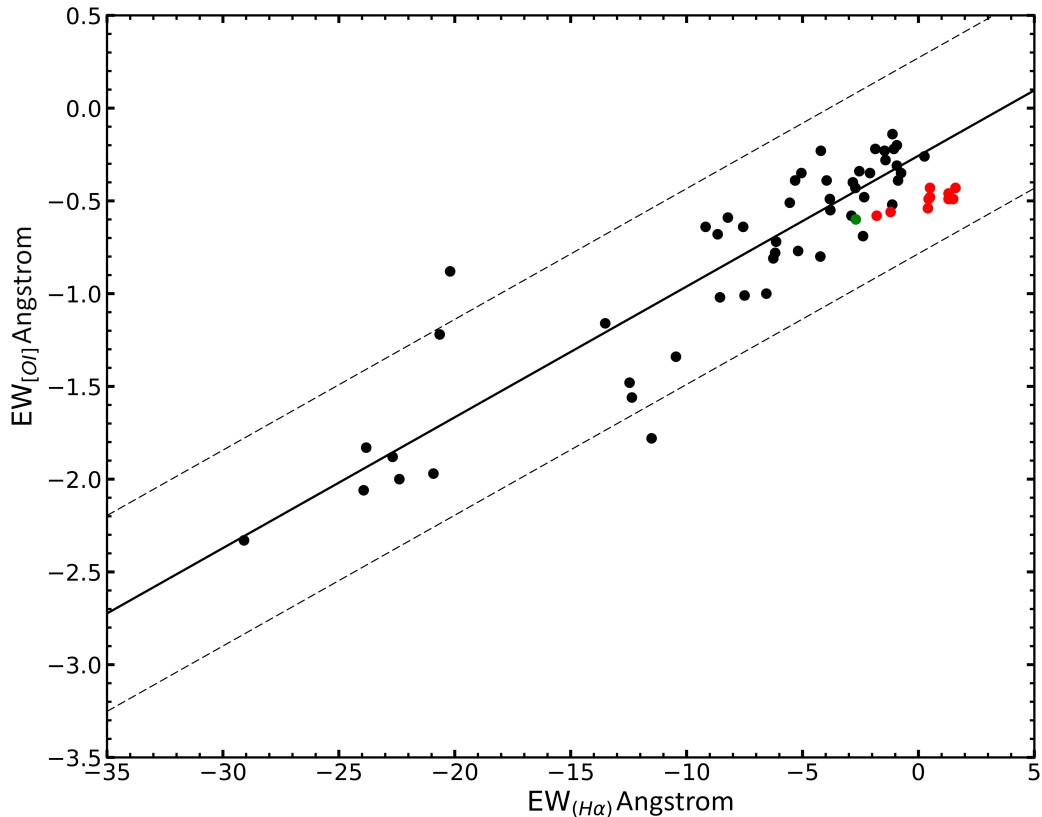
FIGURE 4.12: The correlation of the Hα and [O I]λ 6300 EWs. The black points are the FEROS data presented in Schisano et al. (2009). The red points are the measurements from the UVES spectra presented here and the green point is the average values from the Covino et al. (1997) dataset.

The Na D lines are observed in the 2d spectra. The NaD absorption features are generally centred around the photospheric lines with only slight red or blueshifts of $\sim$ 5 - 10 km s^{-1} in each epoch. While there were no signals expected in the NaD lines, they were used in order to calculate the RV of T Cha for our observations via cross-correlation. The RV values can be found in Table 4.2.

4.3.2 Artefacts

In this work the spectro-astrometric analysis was carried out using specially designed python routines. During the analysis two problems with artefacts were encountered.
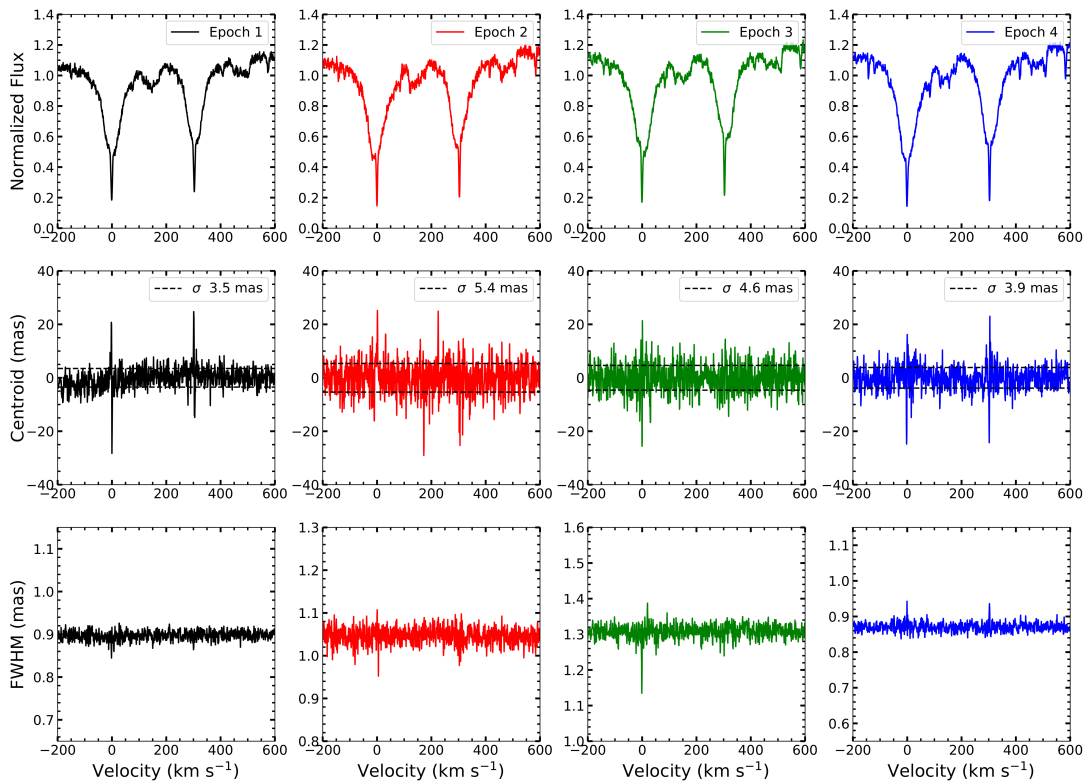
FIGURE 4.13: Combined NaD spectra for each epoch. Epochs 1 to 4 are shown from left to right, and from top to bottom is normalised flux, centroid and FWHM. The x-axis is velocity, zeroed at 5896 Å. The photospheric lines have not been removed in these spectra due to their position within the absorption features from T Cha itself.

In Whelan et al. (2015) the authors discussed how X-Shooter data is affected by spatial aliasing due to the rebinning of the spectra from the physical pixel space (x,y) to the virtual pixels (wavelength, slit-scale) by the X-Shooter pipeline.

The consequence of this for the SA was that an oscillating pattern on a scale of ~ 10 mas was introduced to the position spectrum. In Figure 4.14 the Hα position spectra for the PA of 157° is shown and a similar pattern is seen as was found in the X-Shooter observations of Whelan et al. (2015). It is argued that the rebinning step in the UVES pipeline is also causing a spectro-astrometric artefact due to spatial aliasing. The solution to this first artefact is not to use the pipeline reduced 2D spectra for the SA but to re-reduce the data. The spectra were therefore re-reduced using standard IRAF routines which did not include a re-binning step.

A second artefact was encountered following the median combination of some of the spectra. As stated in Table 4.1 each epoch is made up of numerous separate observations. For each epoch, each individual spectrum was analysed separately. While slight signals may be seen in individual observations, because the signal we are looking for is so small it is almost impossible to tell whether these are noise until the observations

65

are combined into a single spectrum. Therefore, the observations within each epoch were median combined into single spectra. For epoch 3 strong signals were detected in the median combined data but not in the individual spectra (see Figure 4.15). Close inspection of the spectra revealed that the position of the source in the slit had drifted between observations and thus artefacts analogous to those caused by imperfect tracking were introduced when the spectra were combined. To check that this is indeed the origin of the artefact we firstly removed the spectra that showed the maximum drift.

The spectro-astrometric analysis of the median combined remaining spectra showed no signal. A different approach was to shift the position of the spectrum in each 2D order so that the centres of each spectra were at the same position and then to median combine the shifted spectra. As is clear from Figure 4.15, no spectro-astrometric signal was detected in the median combined shifted spectra. One of the motivations for taking several spectra rather than just one long observation was to allow
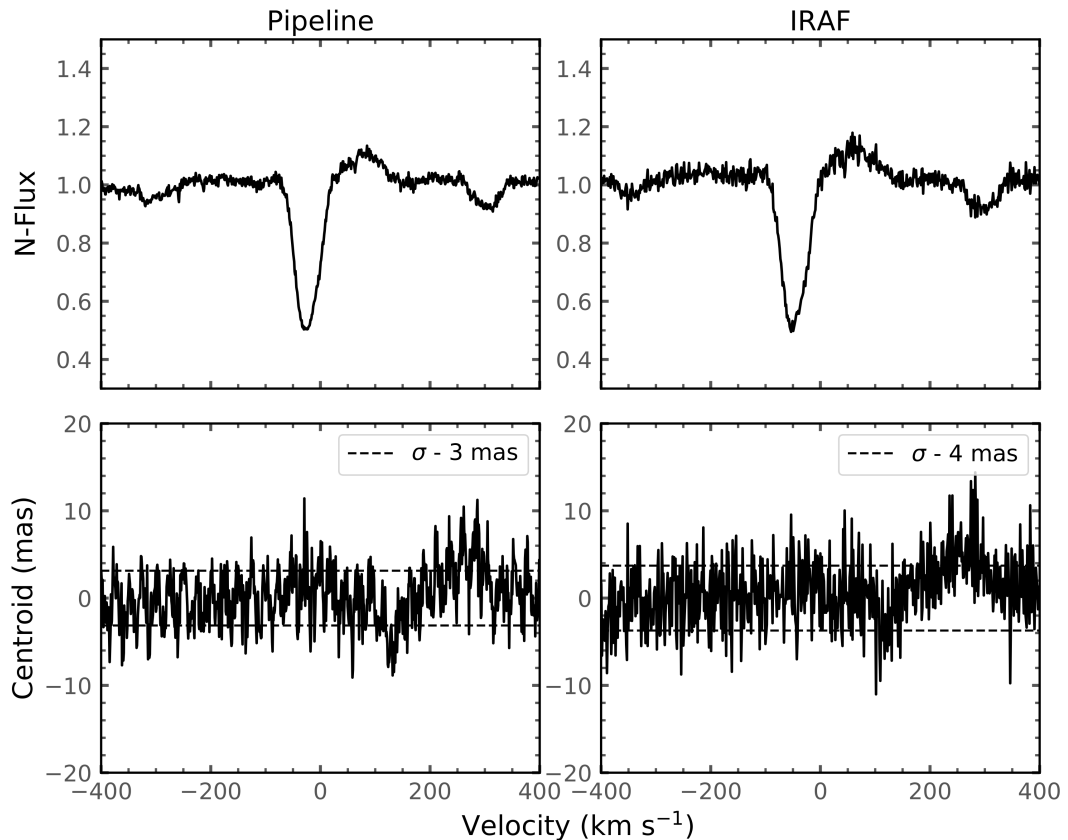
FIGURE 4.14: Figure showing the instrumental effect introduced by the pipeline reduction method (left panels), as the UVES Pipeline was not created with spectro-astrometry in mind. This is due to pixel shift during the re-binning and straightening process, causing the repetitive, almost sinusoidal pattern seen in the bottom left panel. The spectrum (right panels) has been reduced by hand and the instrumental effect has been removed. The top panels show normalised flux and the bottom show the position spectrum.
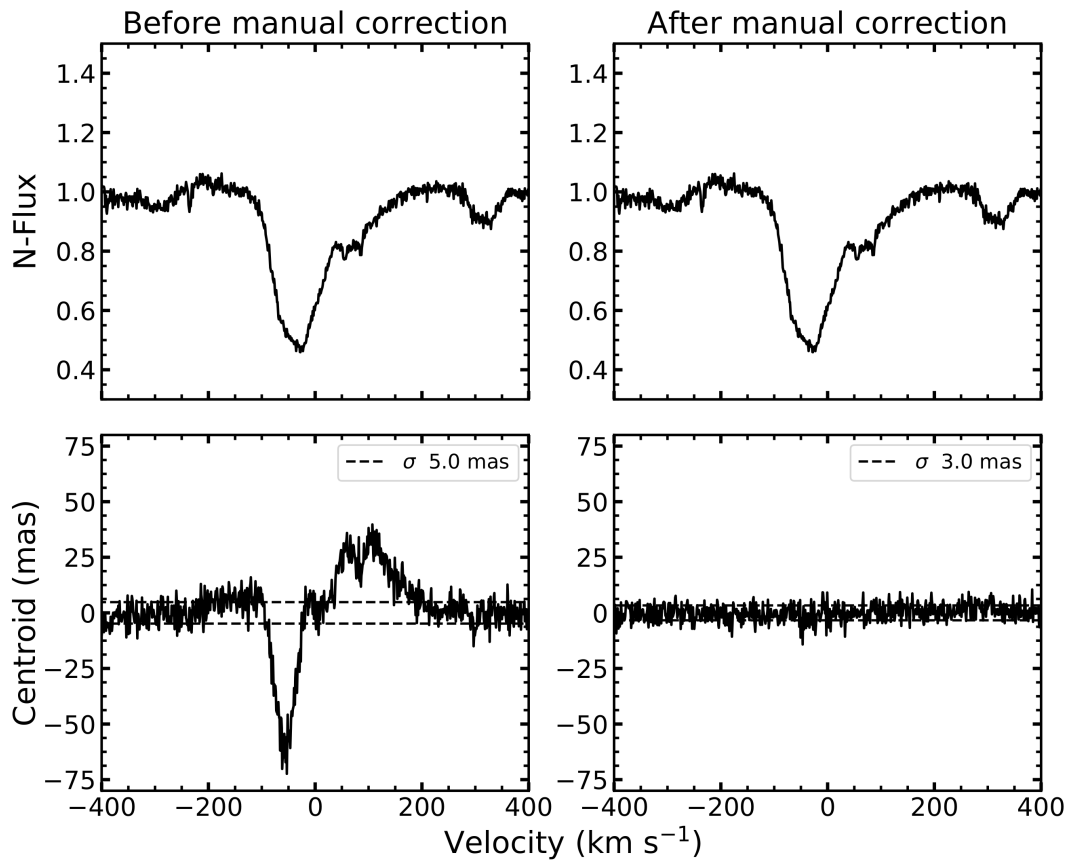
FIGURE 4.15: Comparing the unaltered median-combined normalised Hα line profiles and centroid measurements (left) and manually re-aligned Hα profile and centroid measurements (right). Both plots are taken from epoch 3 at the zero position angle.

for maximum consideration of the source variability. This artefact should be considered when planning future spectro-astrometric studies where variability is a factor.

4.3.3 Line Profiles

As mentioned earlier, an impressive property of T Cha is its extreme variability on the timescale of only a few days. The line profiles of NaD, [O I]λ 6300 and Hα are presented in Figure 4.16.

For each epoch in Figure 4.16, the black line represents the initial PA and the red line the orthogonal PA (in epoch 1 the PAs are 67° and 157° and for epoch 2 - 4 the PAs are 0° and 90°). The NaD line profiles are similar in both PA and epoch, with only minor changes in continuum absorption features around the lines themselves. The [O I]λ 6300 line profiles in epoch 2 - 4 all show a small absorption feature at 0 km s^{-1} centred in the emission region. This is indicative of the circumstellar disk (van der Plas et al. 2008), and the small changes in line profile are associated with disk inhomogeneity.
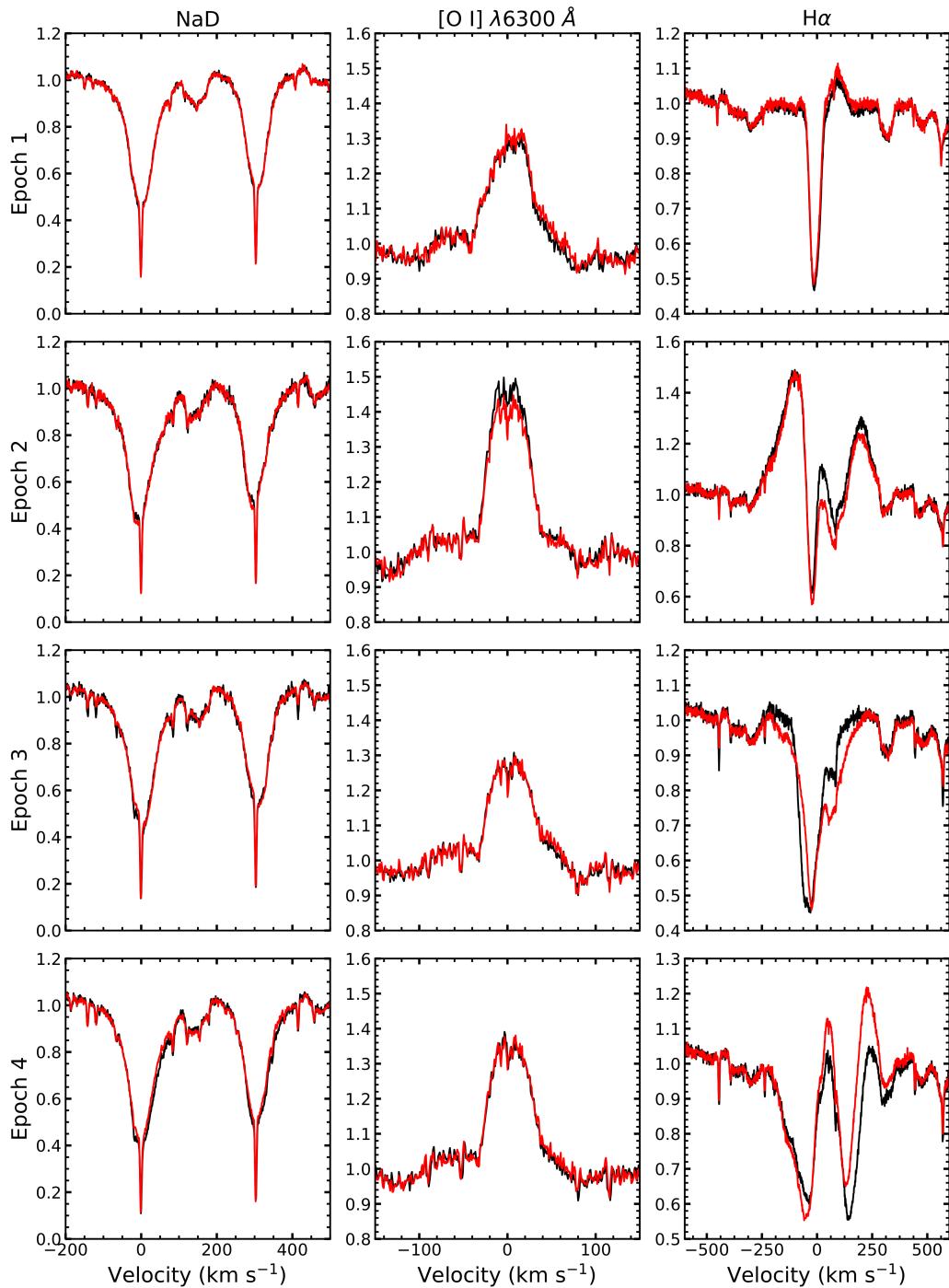
FIGURE 4.16: line profiles, centroids and FHWMs for the major lines present in our observations, normalised and corrected for heliocentric and radial velocity.

The Hα line profiles are most variable in epochs 2 - 4. The clearly visible changes in line profile between the orthogonal PAs within each epoch show how quickly the profile changes, despite the images being taken within a few months of each other.

This figure also allows the comparison between the [O I]λ 6300 and Hα line profiles.

Epoch 1 shows slightly blueshifted absorption and a small redshifted emission feature at 50 km s^{-1}in [O I]λ 6300 profile. This correlates with a relatively low normalised oxygen flux value of just over 1.3. Epoch 2 contains the most significant source of emission in all of the epochs, with a large blueshifted emission feature centred at -100 km s^{-1} and a smaller redshifted feature centred at 150 km s^{-1}. The oxygen emission profile in epoch 2 is also the strongest in the data set, peaking at a value of 1.5. Epoch 3 contains the strongest absorption feature in Hα, and the oxygen emission in this epoch is at its lowest, barely reaching a value of 1.3. Epoch 4 contains both blueshifted and redshifted absorption in Hα with a small emission feature at 250 km s^{-1} most prominent in the 90° PA. The shifts in emission and absorption features in Hα as well as corresponding changes in the strength of the oxygen line profile point to a macroscopic process affecting all regions of the stellar spectrum simultaneously. The changes in the continuum level itself also mirror the changes in emission line strength pointing towards and obscuration of the star itself. This may be due to the high inclination of T Cha's disk, with patches of dust in the inner circumstellar disk blocking out the star periodically.

4.3.4 Radial Velocity Measurements

In order to calculate the RV of T Cha over the different epochs, the template HD 142391 was downloaded from the ESO archive. The template was then corrected for heliocentric velocity (around 9.8 km s^{-1}) and its known RV of 44.8 km s^{-1} (Nordstrom et al. 2004). Once the template was corrected for these values, the spectra of T Cha were compared and a Gaussian was fitted to both of the NaD absorption features. Once the absorption peaks were centred at the same position as the NaD lines from the template via cross-correlation, the corresponding RV was recorded and presented in Table 4.2. Figure 4.17 shows an example of this with the initial uncorrected spectra of the template (black dashed line) and T Cha (red dashed line), and the corrected spectra (solid lines).

4.3.5 Mass Accretion

According to the magnetospheric accretion model, accretion material moves along the closed magnetic field lines from the inner disk onto the central star. When the accreting material impacts the stellar surface we have a shock. As shown by Gullbring et al. (1998), the luminosity released in the impact of the accretion flow can be derived from
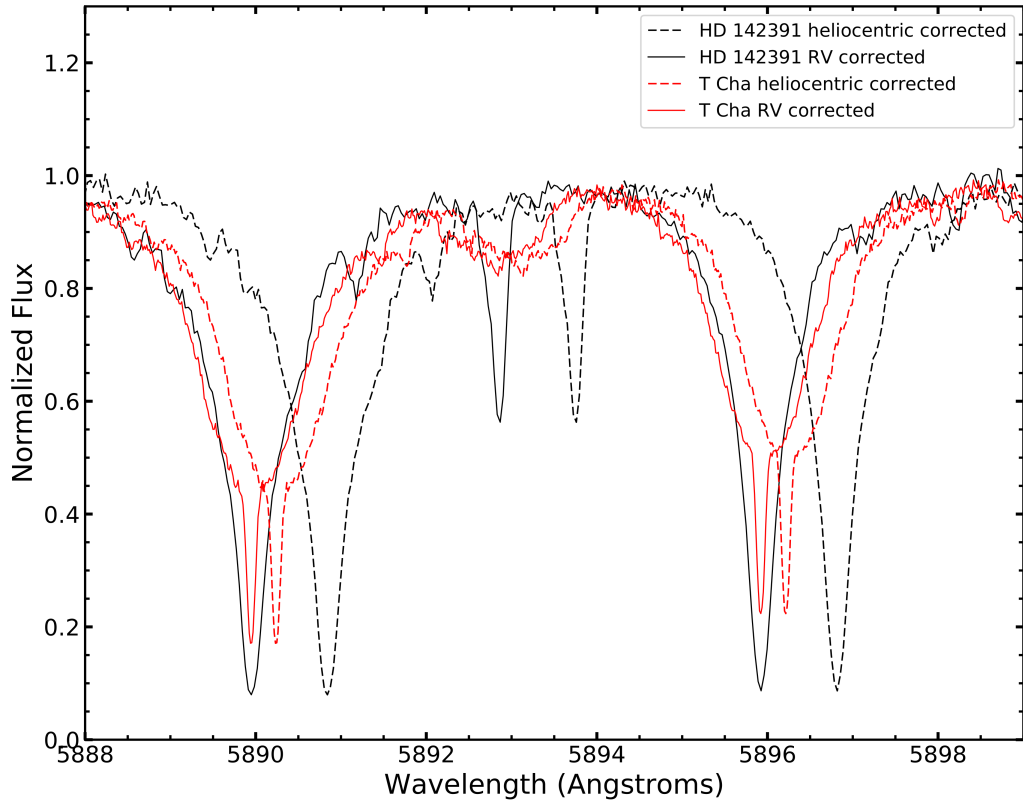
FIGURE 4.17: Figure depicting how cross-correlation was applied to the normalised NaD lines in T Cha with respect to the template HD 142391 to calculate RV values.

the energy equation as

$$L_{acc} = (GM_*M_{acc}/R_*)(1 - R_*/R_{in}), \tag{4.1}$$

where M_* and R_* are the mass and radius of the star, and R_{in} is the radius of the inner accretion disk of the star.

The accretion luminosity can be directly measured by quantifying the UV excess. If there are no observations of the UV excess one can use the observed empirical correlations between the luminosity of some optical and near-IR lines which are thought to be excited in the accretion columns and L_{acc} (e.g. Fang et al. (2009); Herczeg et al. (2011); Muzerolle et al. (2003)). These correlations are found for large samples of stars for which a direct measurement of the UV/optical excess and of the luminosity of emission lines (e.g. Hα, Hβ, Paβ, Brγ etc.) was available. Here we follow this approach to measure $\dot{M}_{acc}$ for T Cha.

T Cha is known to lack both detectable veiling and UV excess which is indicative of low mass accretion Schisano et al. (2009). However, the high inclination angle of the T Cha

disk could mean that a significant amount of the emission from the accretion zone could be blocked by the circumstellar disk giving the impression of a low $\dot{M}_{acc}$. The effect of a high inclination angle disk on the accretion properties has been reported for other objects (Whelan et al. 2014a). Also Schisano et al. (2009) note that the non-detection of veiling in T Cha may also be caused by the relatively high continuum flux emitted by its G8 photosphere. Schisano et al. (2009) also estimate the mass accretion rate for T Cha at $\log(\dot{M}_{acc})$ = -8.4 $M_\odot$ yr^{-1} using the width of the $H\alpha$ line at 10% intensity. However, there were several uncertainties associated with this estimate, including the difficulty in defining the continuum level, the fact the relationship between $\dot{M}_{acc}$ and the 10% width of the $H\alpha$ line (that was derived for the substellar mass regime) shows a larger dispersion at higher masses and finally that the relationship could only be applied where Gaussian decomposition of the line profile into an emission component with overlapping absorptions was possible. As the $H\alpha$ line is primarily detected in absorption here it is not possible to use the $H\alpha$ 10% width or line luminosity to estimate $\dot{M}_{acc}$, although the latter is attempted here for epoch 2. An alternative is to use the [O I]λ 6300 line which is used as an indirect tracer of $\dot{M}_{acc}$ in TTSs (Nisini et al. 2017; Whelan et al. 2014a).

To calculate $\dot{M}_{acc}$ from the [O I]λ 6300 line the relationships of Nisini et al. (2017) giving the luminosity of the [O I]λ 6300 LVC in terms of both $\log(L_{acc})$ (Figure 4.18 blue points) and $\log(M_{acc})$ (Figure 4.18 red points) were used. Also included in this calculation were the Covino et al. (1997) [O I]λ 6300 line luminosities reported in Table 3 of Schisano et al. (2009) and given here for completeness in Table 4.3. The mean value of $\log(\dot{M}_{acc})$ calculated from the Nisini et al. (2017) relationships (denoted by the blue markers in Figure 4.18) is -8.2 $\pm$ 0.4 $M_\odot$ yr^{-1} and this is marked in Figure 4.18 by the black line. The standard deviation in the results is delineated by the black dashed lines. The green dashed line is the average $\dot{M}_{acc}$ value from Schisano et al. (2009) and the green point is the value calculated using the luminosity of the part of the $H\alpha$ line in emission in epoch 2. The mass accretion rate derived using the $H\alpha$ flux in epoch 2 is -10.1 $\pm$ 0.2 $M_\odot$ yr^{-1}. For this calculation the relations of Alcala et al. (2017) were used. Assuming for the time being that the $H\alpha$ emission line region must originate from outside of the occulting zone, no extinction correction was applied.

The (L_{line}) is estimated using the equation

$$L_{line} = 4\,\pi\,d^2\,f_{line}, \tag{4.2}$$

where d is the distance to T Cha and f_{line} is the flux of the [O I]λ 6300 line. We then use the relationship between L_{acc} and L_{Line} in Nisini et al. (2017) for the LVC of the

Epoch	F_c	$EW_{H\alpha}$ (Å)	$EW_{[OI]}$ (Å)	$FWHM_{[OI]}$ (km s^{-1})	$L_{[OI]}$	$\log(\dot{M}_{acc})$
E1-67	2.1	0.50	-0.43	54	3.0 ± 0.1	-7.9
E1-157	2.5	0.44	-0.49	55	4.1 ± 0.1	-7.5
E1-247	2.4	0.50	-0.48	57	4.4 ± 0.1	-7.6
E1-337	2.5	0.41	-0.54	57	4.3 ± 0.1	-7.6
E2-0	0.5	-1.80	-0.58	45	1.1 ± 0.1	-8.5
E2-90	0.6	-1.2	-0.56	46	1.1 ± 0.1	-8.5
E3-0	0.6	1.3	-0.46	51	0.8 ± 0.1	-8.8
E3-90	0.9	1.6	-0.43	53	1.2 ± 0.1	-8.5
E4-0	0.8	1.5	-0.49	47	1.2 ± 0.1	-8.4
E4-90	0.9	1.3	-0.49	52	1.3 ± 0.1	-8.4
C1:C6	-	-2.7	-0.6	-	1.4 ± 0.1	-8.4
C1	-	-	-0.8	-	1.4 ± 0.1	-8.4
C2	-	-	-0.9	-	1.3 ± 0.1	-8.4
C3	-	-	-1.2	-	1.5 ± 0.2	-8.3
C4	-	-	-0.3	-	1.3 ± 0.1	-8.4
C5	-	-	-0.3	-	1.2 ± 0.1	-8.5
C6	-	-	-0.2	-	1.2 ± 0.2	-8.5

TABLE 4.3: The extinction, stellar continuum flux ($\times 10^{-13}$ erg/s/cm^2/Å), Hα and [O I]λ 6300 EWs, FWHM, line luminosity (in units of 10^{-5} L$_\odot$) and corresponding mass accretion rate (in units of M$_\odot$ yr^{-1}) for each epoch. The error in the radial velocity measurements is 2 km s^{-1}. The $\log(\dot{M}_{acc})$ values are the mean values from the two Nisini et al. (2017) relationships. The line fluxes and consequently the line luminosities are without an extinction correction and have the continuum emission subtracted. Also shown are the values from the Covino et al. (1997) study and presented in Table 3 of Schisano et al. (2009). C1:C6 is the average values for the 6 epochs of the Covino et al. (1997) data.

[O I]λ 6300 line luminosity which is given as

$$log(L_{[OI]LVC}) = a^*log(L_{acc}) + b, \tag{4.3}$$

where a and b are the slope and constant of a line equation, and are taken as (0.59 $\pm$ 0.04) and (-4.13 $\pm$ 0.11) respectively. As can be seen in figure 4.16, there is no major HVC seen in any of our epochs. Then the equation

$$\dot{M}_{acc} = 1.25^*(L_{acc}R_*)/(GM_*), \tag{4.4}$$

is used (Gullbring et al. (1998); Whelan et al. (2015)).

In Figure 4.19 the relationship between mass and mass accretion rate is plotted for low mass and substellar objects, including a sample of TD objects taken from Manara et al. (2014). T Cha is also shown here. The thick and thin red crosses correspond to the TTSs published in Manara et al. (2016) and Alcalá et al. (2014) respectively. The Manara et al. (2016) sample are all Cha I sources. The linear correlation shown is for these objects and the motivation is to see how well the TD objects (especially T Cha),
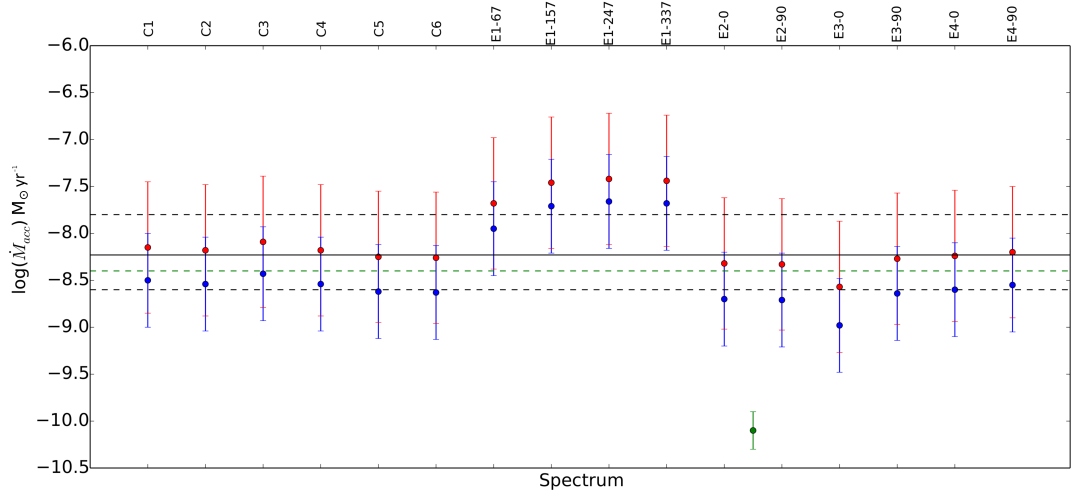
FIGURE 4.18: $\dot{M}_{acc}$ rates for T Cha calculated using the relationships of Nisini et al. (2017). The black points correspond to the values calculated using the $\log(\mathrm{L}_{[OI]LVC})$, $\log(\mathrm{L}_{acc})$ relationship and the blue points to the $\log(\mathrm{L}_{[OI]LVC})$, $\log(\dot{M}_{acc})$ relationship. The 10 UVES epochs are included in the calculation as well as the 6 epochs given in Table 3 of Schisano et al. (2009) and taken from van der Laan, H.; Perola (1969) (labelled here C1 to C6). The black line is the mean value with the 1-σ value shown by the dashed black lines. The green dashed line is the Schisano et al. (2009) result and the green point is the value calculated using the luminosity of the part of the Hα line in emission in epoch 2.

brown dwarfs (BDs) and planetary mass objects follow this correlation. This figure builds on figures published in these papers and on Figure 7 of Whelan et al. (2015). From Figure 4.19 it can be seen that the values of $\dot{M}_{acc}$ for T Cha calculated from the [O I]λ 6300 luminosity, the Hα 10% width and the Hα luminosity in epoch 2 are within the range of values reported for TDs objects, although the epoch 2 value is on the low side. Comparing the epoch 2 Hα $\dot{M}_{acc}$ with the other values would suggest that a significant portion of the Hα emission line region is also obscured during the periods of occultation. It is calculated that the Hα line flux measured in epoch 2 would need to increase 30 fold to give $\log(\dot{M}_{acc})$ = -8.2 M$_\odot$ yr^{-1}. Studies of other young stellar objects have shown that the disk can greatly suppress emission from the accretion zone leading to a perceived low $\dot{M}_{acc}$ (Nisini et al. 2017; Whelan et al. 2014a). The distance of a few tenths of an au proposed by Schisano et al. (2009) as the distance at which the occulting clumps around T Cha orbit would be sufficient to block emission from the accretion zone as well as the star and thus can explain the large dimming of the Hα line emission. Accretion is expected to occur on a scale of $\sim$ 0.1 au (Hartmann et al. 2016). Therefore, the bulk of the Hα emission must come from accretion here with perhaps also a small contribution from a wind. Whereas a greater portion of the [O I]λ 6300 line is originating from beyond the region of obscuration making it a better measure of $\dot{M}_{acc}$ in this case (Nisini et al. 2017).
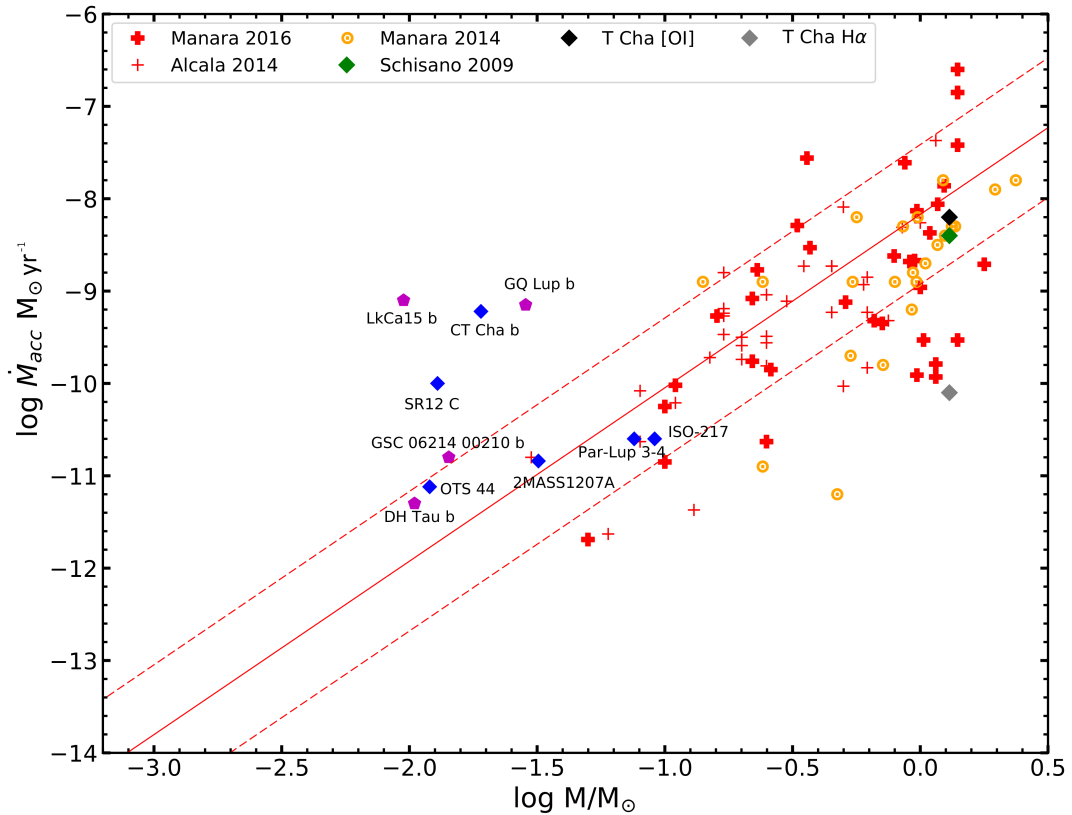
FIGURE 4.19: Comparison of the $\dot{M}_{acc}$ values obtained for T Cha with accreting objects with masses within the range of low-mass stars to planets. The planets are represented by purple hexagons and the BDs by blue diamonds and they are all marked with their names. The red line represents the linear fit to the results of Alcalá et al. (2014) and Manara et al. (2016) for a sample of TTSs. It gives the correlation between M and $\dot{M}_{acc}$ for these types of objects. The dashed lines represent the 1-σ deviation from the fit. The yellow dots are a sample of TD objects taken from Manara et al. (2014). The values of $\dot{M}_{acc}$ for the TD objects generally lie within the range of the TTS values. For the individual BDs and planets the results are taken from the following studies. Lk Ca15 b Whelan et al. (2015); GQ Lup b, GSC 06214 and DH Tau b - Zhou et al. (2014); LkCa 15 b - Sallum et al. (2015); OTS 44 - Joergens et al. (2013); 2MASS1207A - Mohanty et al. (2005); ISO-217 - Whelan et al. (2014b); Par-Lup3-4 - Whelan et al. (2014a); SR 12 C - Santamaría-Miranda et al. (2017); CT Cha B - Wu et al. (2015).

4.3.6 The protoplanet T Cha b

The existence of a protoplanet, T Cha b, orbiting around T Cha has been debated since its hypothesis in 2011. Huelamo et al. (2011) discovered a gap in the disk of T Cha by fitting of its SED. It was then observed in the L' and K_S filters and emission from a faint companion was detected, but only in the L' band. It was also not confirmed whether this object was bound to the primary. Then, Olofsson et al. (2013) modelled the SED with *MCFOST*, a Monte Carlo radiative transfer code for *Python*, and found that forward scattering from the edge of the disk was the most likely source of the

detected emission. Cheetham et al. (2015) observed T Cha with the same setup as was used by Huelamo et al. (2011), but with 3 additional years of data. It was concluded that while the detected emission was indeed present in the datasets, it was caused by an artefact introduced during the image reconstruction phase.

The presence of a gap in T Cha's circumstellar disk remained an incentive for further study, and Pohl et al. (2017) observed T Cha using SPHERE on the VLT. It was found that a companion larger than 8.5 M_{Jup} was ruled out for distances between 0.1" - 0.3", and this limit decreased to 2 M_{Jup} for distances of 0.3" - 0.4", but the possibility of lower-mass planets still existed. Hendler et al. (2018) presented ALMA observations that were in agreement with the predictions of Pohl et al. (2017), but proposed that the most likely force carving out the gap clearly present in T Cha's circumstellar disk is an embedded planet/s. In the single-planet scenario, a mass of 1.2 M_{Jup} was estimated; however, the width of the gap meant that this planet must have an eccentric orbit, and a multi-planet scenario was chosen as a more likely determinant for the observed gap in the disk of T Cha.

This led to the motivation behind applying SA to T Cha, and while no confirmed signal is detected, the methodology of Whelan et al. (2015) can be used to apply an upper limit to the mass accretion of a 1.2 M_{Jup} planet if it does indeed reside within the disk of T Cha.

4.3.6.1 Mass Accretion

The planetary mass accretion rate has only been measured to date for a small number of objects and some results have been higher than would be expected (LkCa 15 b and GQ Lup b) if the correlation for TTS extends into the planetary regime (refer to Figure 4.19).

For example, LkCa 15 b and DH Tau b are two cases of planetary mass accretion estimates for two different scenarios: LkCa 15 b is an embedded protoplanet while DH Tau b is a wide companion (Whelan et al. 2015; Zhou et al. 2014). For arguments sake, let us assume that T Cha b is actually a 10_{Jup} planet, we can use the $\dot{M}_{acc}$ values to give an upper and lower limit to the $\dot{M}_{acc}$ of T Cha b. For the upper limit, Whelan et al. (2015) calculated a $\log(\dot{M}_{acc})$ of -8.9 and -9.3 $M_{\odot}$ yr^{-1} for masses of 6 M_{Jup} and 15 M_{Jup} respectively. These both correspond to $L_{H\alpha} \sim 7 \times 10^{-5}$ $L_{\odot}$, so this would be a reasonable upper limit for T Cha b. For the lower limit, Zhou et al. (2014) measured $\log(\dot{M}_{acc})$ = -11, -9.3 and -11.4 $M_{\odot}$ yr^{-1} for GSC 06214 -00210, GQ Tau b and DH Tau b respectively, using the luminosity of their Hα emission. These values of

$\dot{M}_{acc}$ correspond to $L_{H\alpha} = 9.3 \times 10^{-6}$ $L_\odot$, 2×10^{-5} $L_\odot$ and 6.5×10^{-7} $L_\odot$. Also Zhou et al. (2014) give the masses of these three objects as 15 M_{Jup}, 28 M_{Jup} and 11 M_{Jup} respectively. Keeping to our assumption of a mass of ~ 10 M_{Jup} for T Cha b, a value $L_{H\alpha} = 1 \times 10^{-6}$ $L_\odot$ would seem reasonable as a lower limit given the results of Zhou et al. (2014). Using the 1-σ upper limit to the correlation presented in Figure 4.19 would suggest a similar value. It is found from our mass accretion rate study that $L_{H\alpha}$ $= 4 \times 10^{-3}$ $L_\odot$ would be needed to achieve $\log(\dot{M}_{acc}) = $ -8.2 $M_\odot$ yr^{-1}. Therefore the ratio between the Hα emission from T Cha and T Cha b can be taken as ranging from 1.8×10^{-2} to 2.5×10^{-4}. Given that Hendler et al. (2018) show the gap to extend from 18 au to 28 au one can expect any planet to be located at ~ 23 au or 190 mas at the distance to T Cha. The corresponding size of the offset that would be measured using SA is this distance multiplied by the ratio of the strength of the Hα emission from the planet and star which is 3.42 - 0.05 mas. Given that a maximum binning of 40 is recommended and would return a spectro-astrometric accuracy of 0.5 mas it is concluded that while it should be theoretically possible to detect a 10 M_{Jup} planet it is not possible to use SA to detect T Cha b in this dataset. It should also be noted that calculation outlined here assumes no contribution from the continuum emission from T Cha and that Hendler et al. (2018) suggest a possible mass of ~ 1 M_{Jup}. Both of these points would mean that an even better spectro-astrometric accuracy would be necessary. It is worth noting that the [O I]λ 6300 $\dot{M}_{acc}$ results were not used to estimate an upper limit to the flux of T Cha b and then used to estimate a $\dot{M}_{acc}$. The reason for this is that it would assume that protoplanets have winds like TTSs, which is something that has not been proven.

4.4 Discussion & Conclusion

The UVES observations of T Cha presented here agree with the conclusions of Schisano et al. (2009). However, by the inclusion of the epoch 1 dataset, looking further at the mass accretion rate and including a spectro-astrometric analysis the results of Schisano et al. (2009) can be added to and the following conclusions made.

1. The spectro-astrometric analysis shows that the likely origin for the [O I]λ 6300 line is a wind. Thus, it is possible that part of the emission due to this wind could be obscured by the disk of T Cha. Indeed, this could be the explanation for the differences noted between the epoch 1 [O I]λ 6300 line profiles and the epoch 2-4 profiles. Overall it can be concluded that the [O I]λ 6300 is a better tracer of the mass accretion rate onto T Cha than Hα as results derived from

$L_{[OI]}$ (-8.2 M$_\odot$ yr^{-1}) give values within the range calculated for other TD objects (generally around -9 $\pm$ 1 M$_\odot$ yr^{-1}).

2. The mass accretion rate study shows that a significant proportion of the Hα emission is suppressed during the periods of obscuration. The mass accretion value derived for Hα of -10.1 M$_\odot$ yr^{-1}points to the bulk of the Hα emission originating from the accretion shocks and the scale over which the obscuration occurs are in agreement with magnetospheric accretion theory. It can be argued that the use of the Hα 10% width as a measure of $\dot{M}_{acc}$ gives a value more compatible with the [O I]λ 6300 line as the Hα line luminosity and not necessarily the line width is affected by the orbiting clumpy material.

3. It is difficult to deduce anything about the origin of the Hα line from the spectro-astrometric analysis. However, by making a reasonable estimate of $\dot{M}_{acc}$ for T Cha b and thus the luminosity of its Hα emission it can be shown that the spectro-astrometric accuracy achieved here is not sufficient to make a detection. This is true even if a large binning is considered. Overall, it is concluded that the unique properties of T Cha i.e. the strong G8 photosphere, the variable continuum emission and the variable Hα emission make it more complicated to apply SA to this source. In particular, the fact that the line is often in absorption means that is is difficult to quantify the contribution from the stellar continuum and to remove it.

To date, two TDs objects have been investigated by us to determine if SA can be used to detect a planetary companion. In Whelan et al. (2015) no detection of LkCa 15 b was made and this planet was subsequently detected using differential imaging with the Hα emission from Lk Ca15 b detected with a line luminosity of 6 $\times$ 10^{-5} L$_\odot$(Sallum et al. 2015). Manara et al. (2014) give log($\dot{M}_{acc}$) = -8.4 M$_\odot$ yr^{-1} for Lk Ca15 which corresponds to L$_{H\alpha}$ = 3 $\times$ 10^{-3} L$_\odot$. Our results for T Cha and estimates for T Cha b are in agreement with these results for Lk Ca15 and LkCa 15 b. Sallum et al. (2015) detect LkCa 15 b at a distance of 93 $\pm$ 8 mas from its parent star. Considering the line luminosities and this distance would mean that a spectro-astrometric accuracy of < 0.2 mas would have been necessary in Whelan et al. (2015) to detect this planet. This is just below the value of 0.5 mas that was achieved, but the value was calculated assuming no contribution from the continuum emission of T Cha and T Cha b having a mass of 10 M$_{Jup}$. As was the case here with T Cha the analysis of LkCa 15 b was also complicated by problems with spectro-astrometric artefacts. From the work described in this thesis and the LkCa 15 study it can be concluded that while straight-forward in theory it is difficult to apply SA to the problem of routinely detecting planetary companions to TD objects.

Chapter 5

HD 142527

This section describes the star HD 142527, and aims to provide a description of the target and a summary of the results obtained. A companion to this star was discovered at a distance of approximately 12 au, using data from the VLT's Nasmyth Adaptive Optics System Near-Infrared Imager and Spectrograph (NaCo) (Biller et al. 2012). This was then confirmed via Hα imaging using AO on the Magellan Clay telescope (Close et al. 2014). As discussed in Chapter 4, Hα is one of the best accretion indicators and this was one of the reasons HD 142527 was chosen. Another reason HD 142527 is a good candidate for spectro-astrometry is that the mass ratio between the companion and its parent (1:15) is smaller than the size ratio between T Cha b and T Cha estimated by Hendler et al. (2018) (1:833). Following the non-detection of T Cha b, the intent is to bridge the gap between detection of binaries and exoplanets via application of SA to a star with a very-low-mass companion, in this case HD 142527B. The Hα emission ratio between HD 142527 and its companion was investigated by Close et al. (2014) and a value of $\sim$ 1 % was calculated.

5.1 Target

HD 142527 is a well studied Herbig Ae/Be star with a distance of 157.3 $\pm$ 1.2 pc (Gaia-Collaboration et al. 2018). Its temperature, mass and age are given by Mendigutía et al. (2014) as 6550 $\pm$ 100 K, 2.0 $\pm$ 0.3 M$_\odot$ and 5.0 $\pm$ 1.5 Myr respectively. HD 142527 was selected for study as it has a highly inclined disk (i $=$ 20° off face-on, Verhoeff et al. (2011)) and the large gap in it that extends from 30 - 90 au (Verhoeff et al. 2011). This provides a wide area to search for the planet formation thought to be the mechanism by which these gaps are cleared. The difference in size between HD 142527
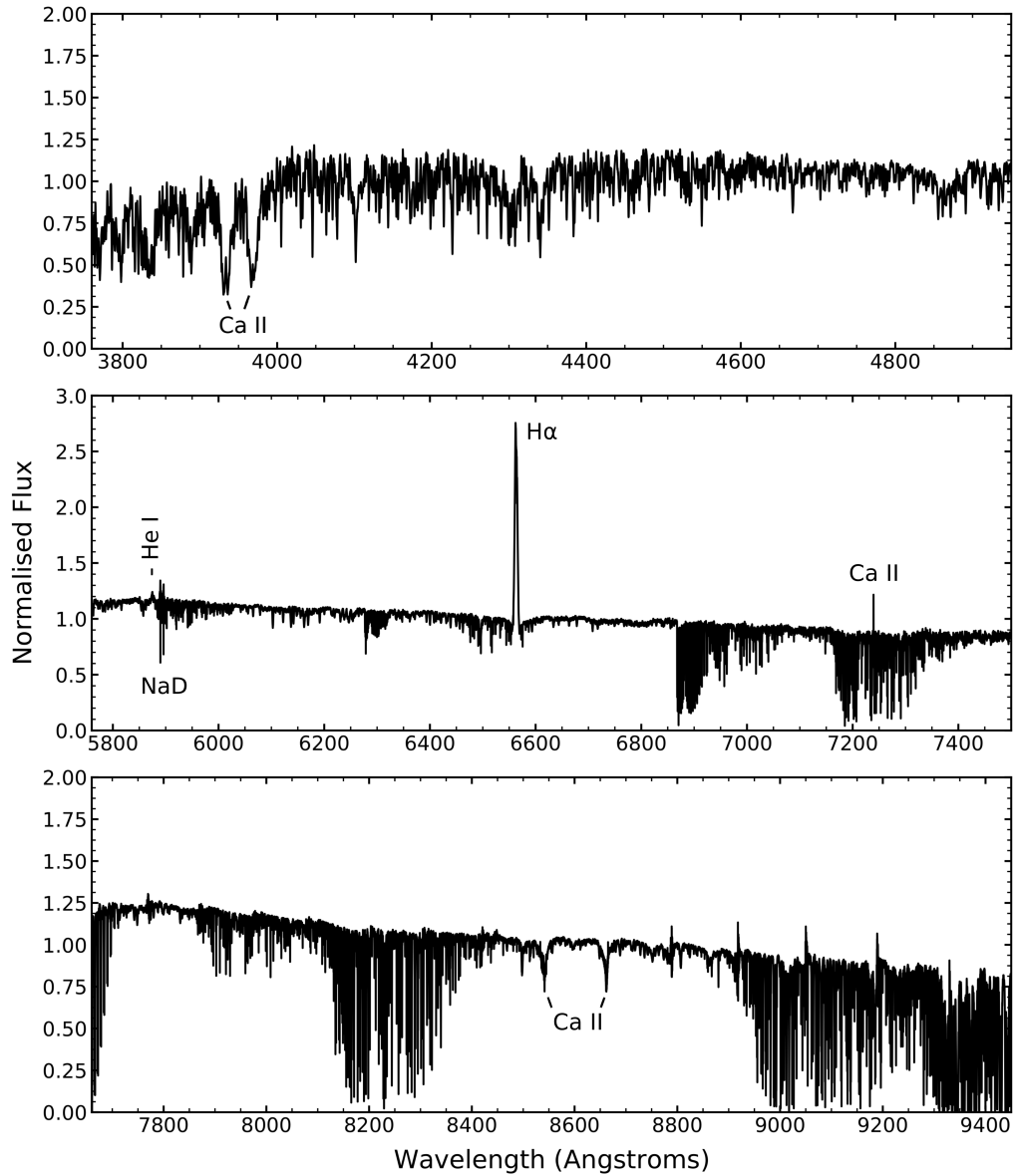
FIGURE 5.1: Figure of HD 142527 showing the wavelength ranges covered for the blue and red (lower and upper) optical paths with prominent lines labelled. This was taken with UVES on the VLT.

and HD 142527B also offers the chance to study the effect a very-low-mass companion has on a circumstellar disk.

In a study on the binarity of Herbig Ae/Be stars, Baines et al. (2006) also applied SA to HD 142527, and found centroid and FWHM signals in the wings of the Hα emission profile. The star was labelled a possible binary due to the lack of a major offset in the centroid, but having a noticeable change in the FWHM. An interesting point is that in their study, HD 142527 showed a P-Cygni Hα profile which is not seen in this dataset,
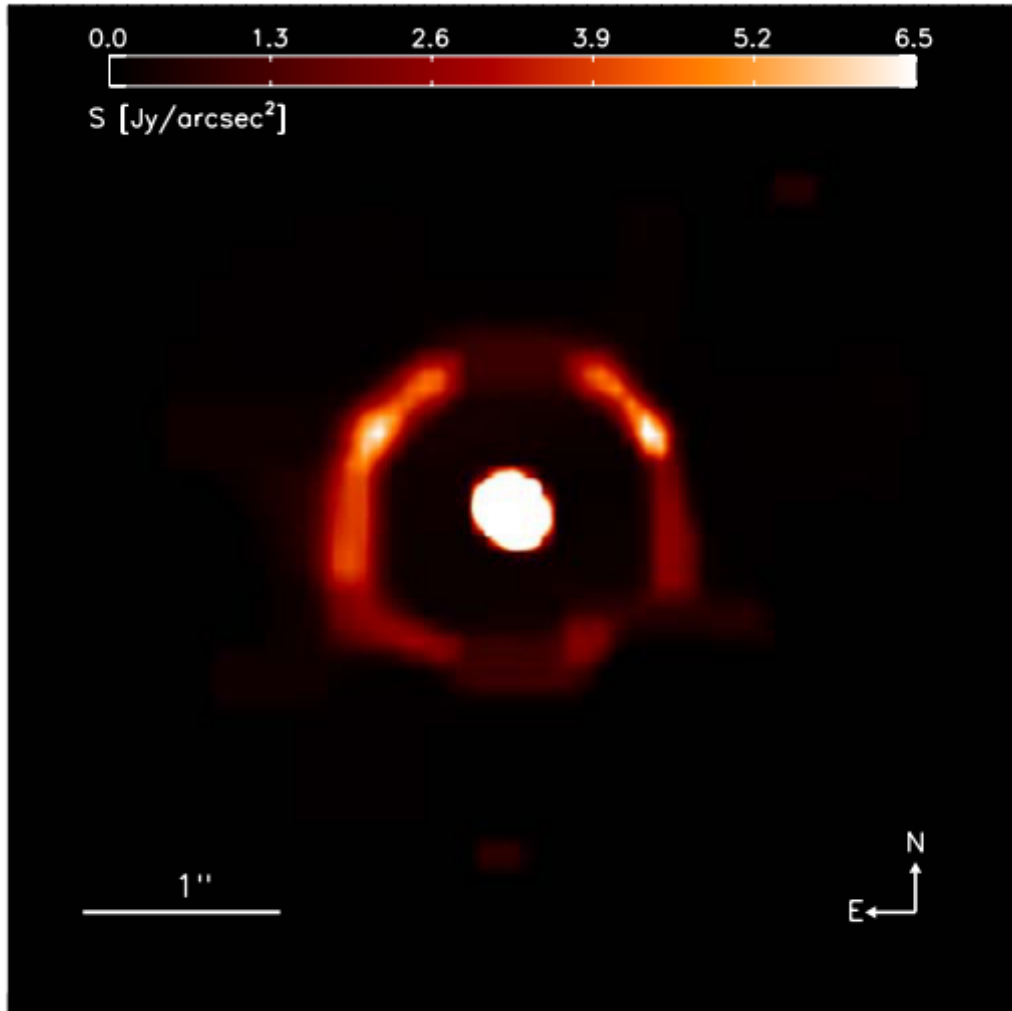
FIGURE 5.2: Deconvolved image of HD 142527 taken with VISIR on the VLT at 18.72μm. This image was taken from Verhoeff et al. (2011).

indicating some variability in the star. A comparison for these results is presented in Section 5.3.2.

Figure 5.1 shows the 3 different wavelength ranges captured during this observation run, and the prominent emission lines are highlighted. It is interesting to note the lack of emission lines present in the spectrum of HD 142527, with only Hα and the NaD lines present in large quantity. Mendigutía et al. (2014) used X-Shooter observations to conduct a study on the stellar parameters and accretion rates from several tracers, but as with the spectrum shown, there was a lack of emission features. For the wavelength range used in this project, only Hα and NaD showed up in the X-Shooter. Both the [O I]λ 6300 and 6363 lines were missing in the spectrum of HD 142527. The lack of [O I] emission indicates there are no outflows from the star.

Lacour et al. (2016) classified the companion, HD 142527B, as an M-dwarf star and constrained its stellar parameters as follows; $T = 3000 \pm 100$ K, $M = 0.13 \pm 0.03$ M$_\odot$ $R = 0.90 \pm 0.15$ R$_\odot$ with an age of ~ 1 Myr. It is cited as being approximately 12 au from the parent star.

5.2   HD 142527 Observations

The observations of HD 142527 all focus on the wavelength range of 3800 - 9000 Å, also using UVES. Both optical paths were used in this program. The blue arm covers the range of 3750 - 5000 Å, while the lower red arm covering 5750 - 7500 Å and the upper arm 7750 - 9500 Å. This observation run was not executed with spectro-astrometry in mind, and as such there are no different PAs to compare results. The slit was aligned with the parallactic angle during observation. Tentative results are put forward nonetheless in Chapter 5.

Obs no.	Optical path	Date	Time (UT)	Obs time (s)	Seeing (")
1	Blue	2010-02-01	08:06	240	1.02
1	Red lower	2010-02-01	08:06	240	1.02
1	Red upper	2010-02-01	08:06	240	1.02
2	Blue	2010-02-01	08:11	240	0.96
2	Red lower	2010-02-01	08:11	240	0.96
2	Red upper	2010-02-01	08:11	240	0.96
3	Blue	2010-02-01	08:16	240	1.12
3	Red lower	2010-02-01	08:16	240	1.12
3	Red upper	2010-02-01	08:16	240	1.12

TABLE 5.1: Details of the observations of HD 142527. The seeing values are corrected for airmass.

5.3   Results

Spectro-astrometric analysis was applied to all observations of HD 142527 listed in Table 5.1. This was performed in an attempt to resolve a signal from a companion that is larger than a protoplanet such as T Cha b, but still smaller than the mass of the main star by a factor of at least 10. The aim is to detect a definite spectro-astrometric signal in order to show the efficacy of spectro-astrometry at this size ratio. There are some factors besides mass ratio that come into play.

Figure 5.3, 5.4 and 5.5 show the normalised flux, centroid and FWHM of the Hα line. These observations were all taken on the same day, and as there is only one PA, it
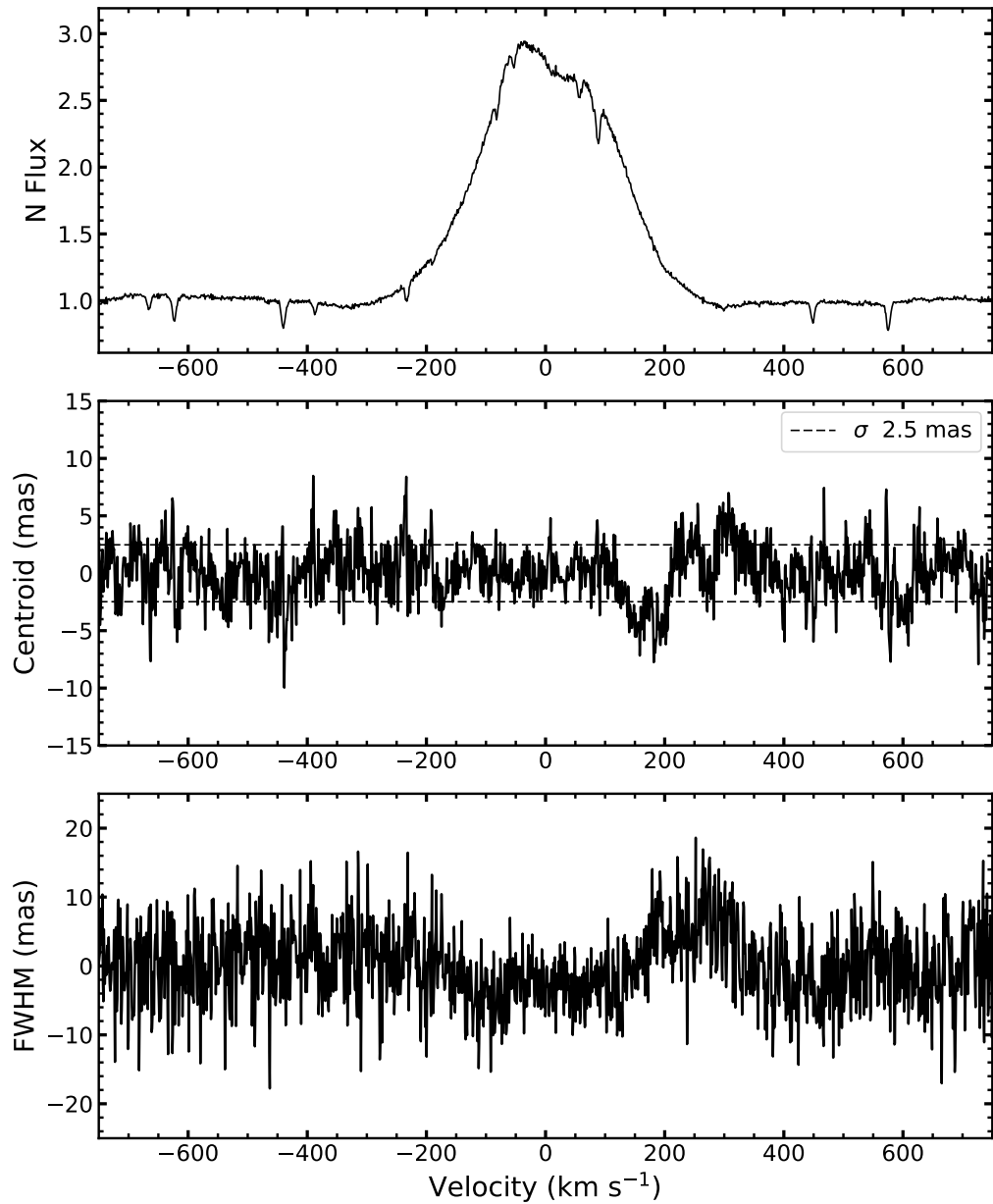
FIGURE 5.3: Figure showing the Hα normalised line profile, centroid and FWHM of the first observation of HD 142527. The black dashed line represents the 1σ deviation. The FWHM has been fitted around zero to highlight the offset. The spectrum has been corrected for heliocentric and radial velocity.

would normally be difficult to establish whether a signal is a result of telescope effects or an actual detection. The line profile in all three observations remains constant. Heavy veiling can be seen in the shallow photospheric absorption lines visible in the figures. A redshifted offset from the centroid position can be seen ranging from 125 - 375 km s^{-1} in all three figures, and a noisier offset in equal intensity can be seen around the photospheric lines, most prominently at $\sim$ -450 km s^{-1}. The FWHM shows
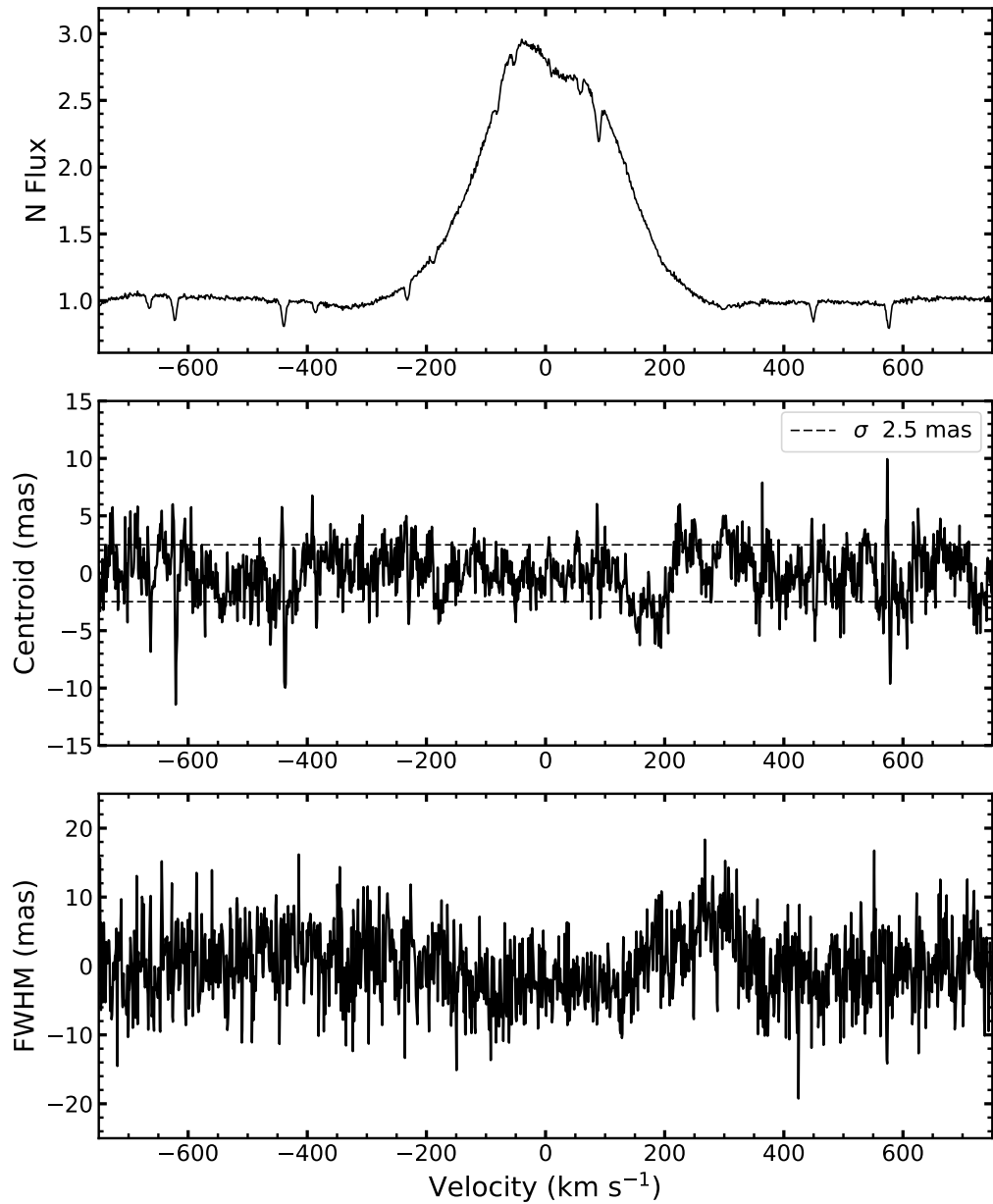
FIGURE 5.4: Figure showing the Hα normalised line profile, centroid and FWHM of the second observation of HD 142527. The black dashed line represents the 1σ deviation. The FWHM has been fitted around zero to highlight the offset. The spectrum has been corrected for heliocentric and radial velocity.

the most promising evidence for a real signal. Matching up with the centroid shift seen from 125 - 375 km s^{-1}, it shows a noticeable deviation from the zero-point.

Figure 5.6 shows a combination of each of the 3 observations from this dataset, and the combined data has had a bin of 40 set on the spectral channel (wavelength) and applied to the centroid and FWHM to increase signal to noise without covering up any signal. The bin choice comes from an expected Hα signal from a companion of between 100
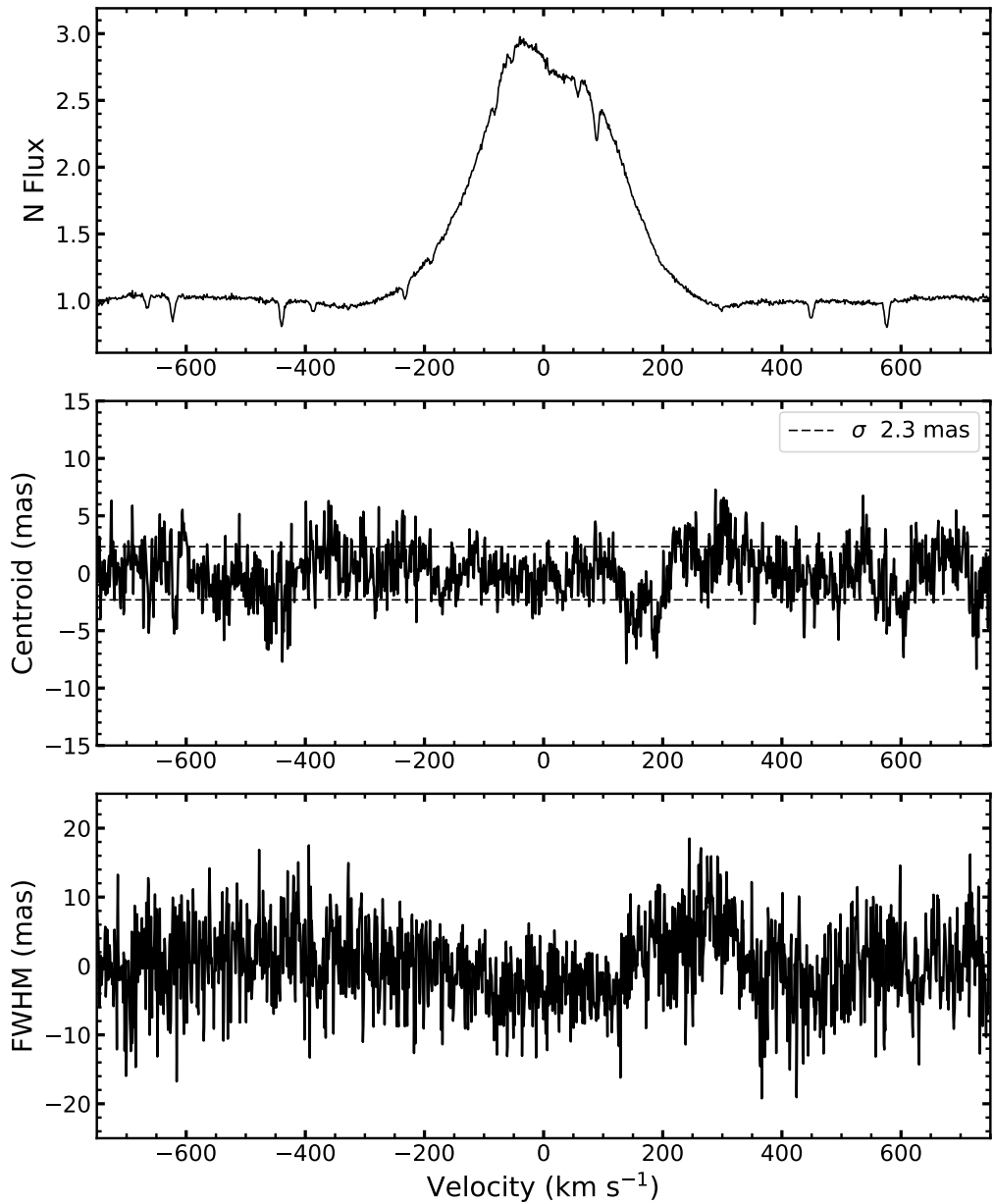
FIGURE 5.5: Figure showing the Hα normalised line profile, centroid and FWHM of the third observation of HD 142527. The black dashed line represents the 1σ deviation. The FWHM has been fitted around zero to highlight the offset. The spectrum has been corrected for heliocentric and radial velocity.

and 200 km s^{-1} as proposed by (Close et al. 2014). The UVES spectrograph provides a spectral sampling of ~ 1 km s^{-1} at the distance of 157.3 pc, and in order to recover any detection, it is recommended to have at least 5 points across the expected signal range. This more than halves the σ range, and the most likely signals centred at 125 - 375 km s^{-1} are just above the 3 σ detection limit.

Indication that the main star dominates the central Hα emission is present in both
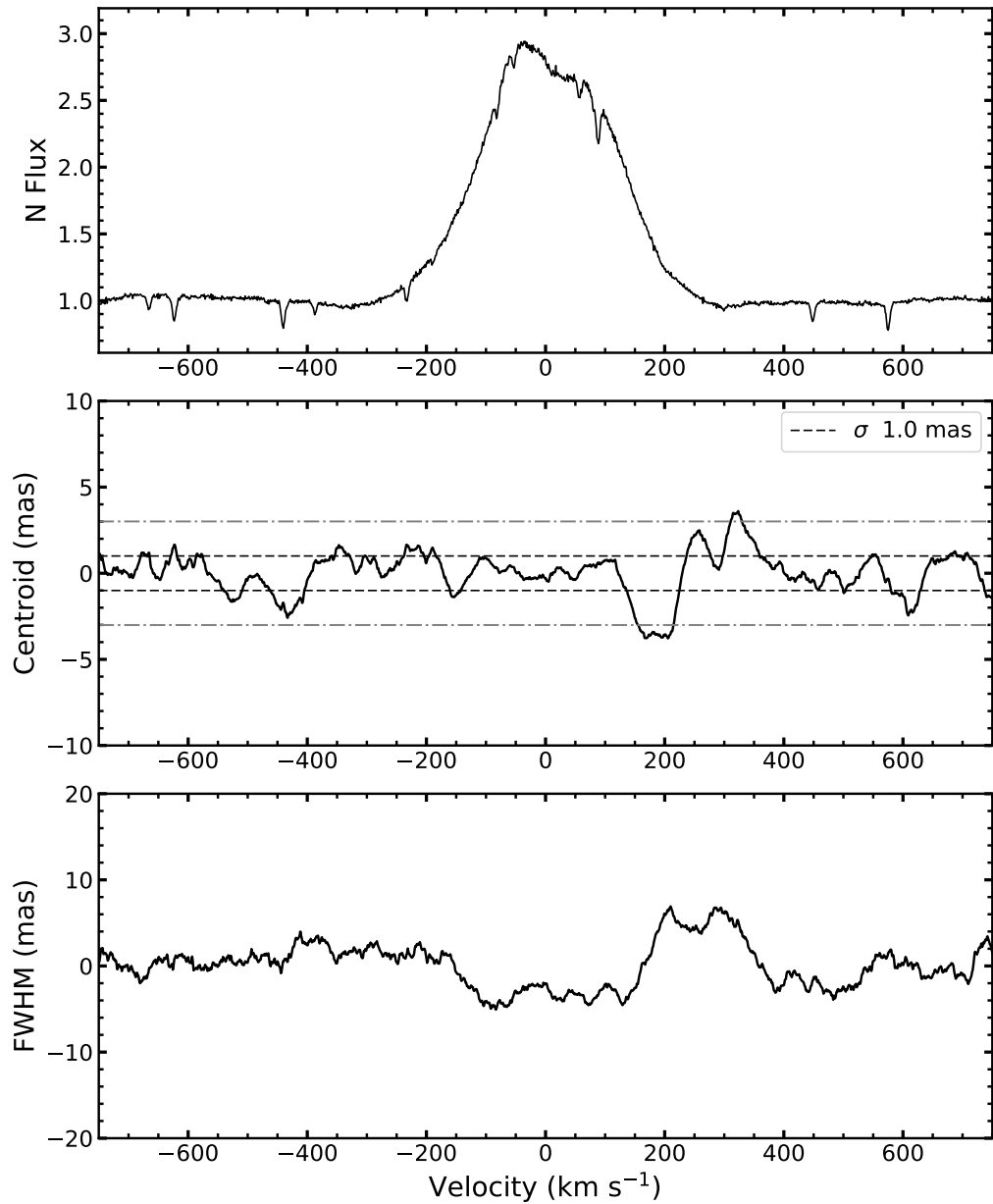
FIGURE 5.6: Figure showing the line profile of the combined observations, with the centroid and FWHM having been binned by a factor of 40. The 3σ deviation is also included as a grey dot-dashed line.

the centroid and FWHM. The centroid values between $\pm$ 100 km s^{-1} lie almost exactly on zero, with a much lower deviation than outside the emission profile. The FWHM also shows a decrease in average value, indicative of a higher intensity. The redshifted increase in FWHM is also visible in Figure 3 of Baines et al. (2006), although a blueshifted deviation was also seen in line with the P-Cygni absorption feature.

5.3.1   Continuum Subtraction

Following the spectro-astrometric analysis of HD 142527 and the detection of a likely signal, continuum subtraction was then applied to the spectra in order to remove any drag caused by the continuum itself. This is possible due to the Hα line being fully in emission for this target. Continuum subtraction should increase any real signal present in the observations (but only across the emission feature), as the method inherently precludes analysis of regions in which there is no emission. This is why there is only data from $\pm$ 200 km s^{-1} present in red in Figure 5.7.

The continuum subtraction highlights the shift away from the zero-point in all the position spectra. The enhanced view of the FWHM in this figure enhances the signal seen at $+$ 200 km s^{-1}. The subtraction of the continuum also allows the blueshifted signal at - 225 km s^{-1} to be seen, which was previously covered up by the strength of the continuum. As both shifts occur at the wings of the emission profile, it suggests a wider line profile for the companion star compared to its parent, which dominates the emission around $\pm$ 100 km s^{-1}.

5.3.2   Comparison to previous works

As mentioned previously, Baines et al. (2006) performed a spectro-astrometric study of a number of stars, including HD 142527. Figure 5.8 shows the results of that study. The star was designated a possible binary due to the lack of a strong centroid offset, despite the presence of a FWHM offset consistent with a binary. In the figure the shifts in the FWHM in both the north-south and east-west directions are clearly visible, but this alone was not sufficient cause for labelling a definite binary detection. As with the results presented in the figures shown in Section 5.3, the signal from Baines et al. (2006) is most evident at the wings of the Hα line profile. The centroid offsets seen in that figure are similar to what was seen in the SA results of this thesis, but the application of continuum subtraction enabled a much clearer centroid signal to be detected, seen in red in Figure 5.7.

5.4   Mass Accretion

The mass accretion rate of HD 142527 was calculated to be compared to previous results, look for variability and to see if it is reasonable to detect a spectro-astrometric
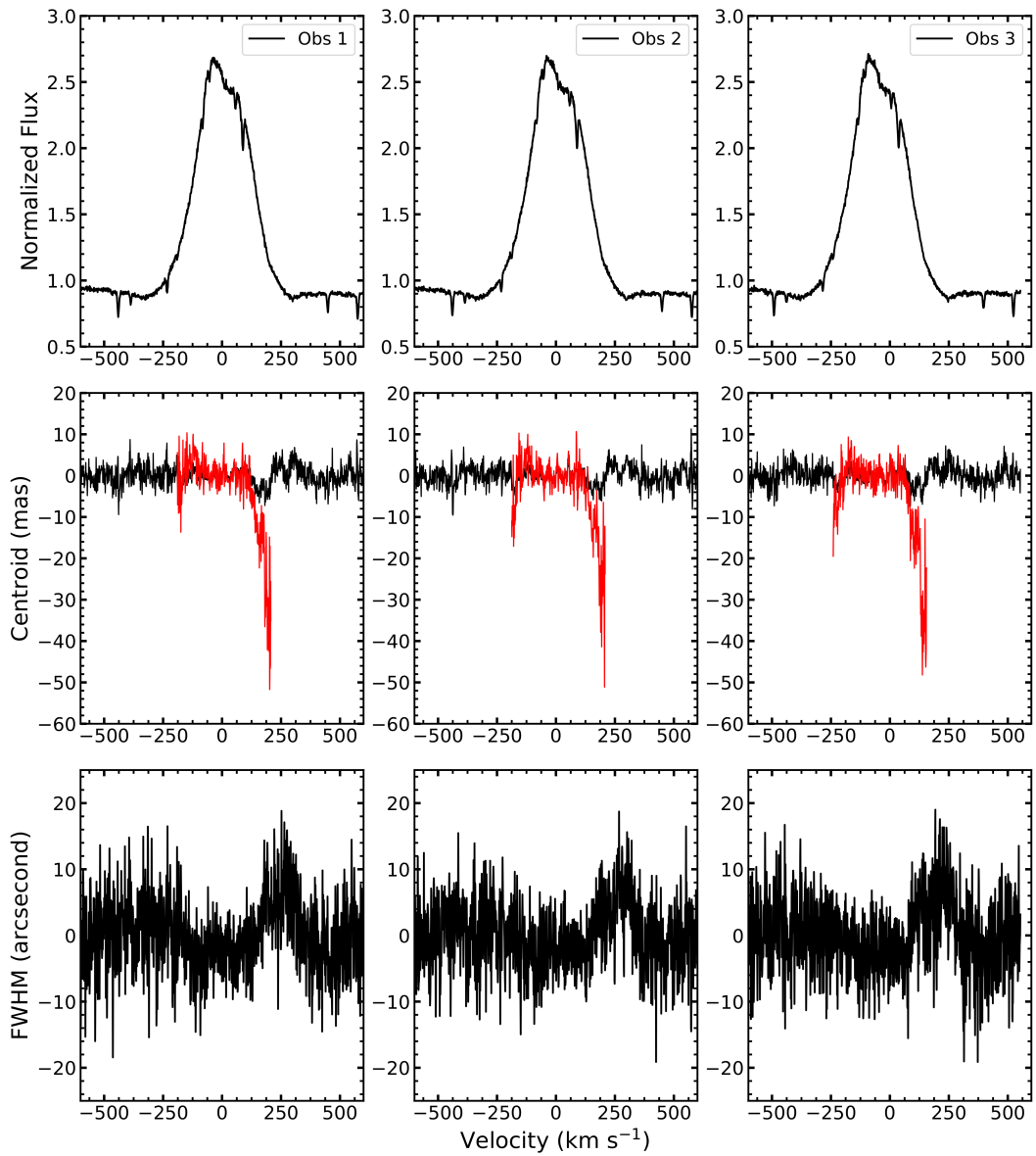
FIGURE 5.7: Figure showing the Hα normalised line profile, centroid and FWHM, with the continuum-subtracted centroid added in red. This value only extends across the emission profile as there is no continuum to measure beyond this point.

signal from HD 142527B. Table 5.2 shows results from the three available epochs. Close et al. (2014) state the value of $\log(\dot{M}_{acc})$ as -7 $M_{\odot}$ yr^{-1}, however there are different results depending on the values chosen for the parameters a (0.59 ± 0.04) and b (-4.13 ± 0.11) in Equation 4.3.

From the values in Table 5.2 the expected $\dot{M}_{acc}$ can be derived as was done for T Cha b. Using the relation in Equation 4.4 and a mass of 0.13 $M_{\odot}$, a value of -9.3 $M_{\odot}$ yr^{-1} is obtained for the $\log(\dot{M}_{acc})$. This implies a $L_{H\alpha}$ of 6.8 × 10^{-5} $L_{\odot}$. Using the
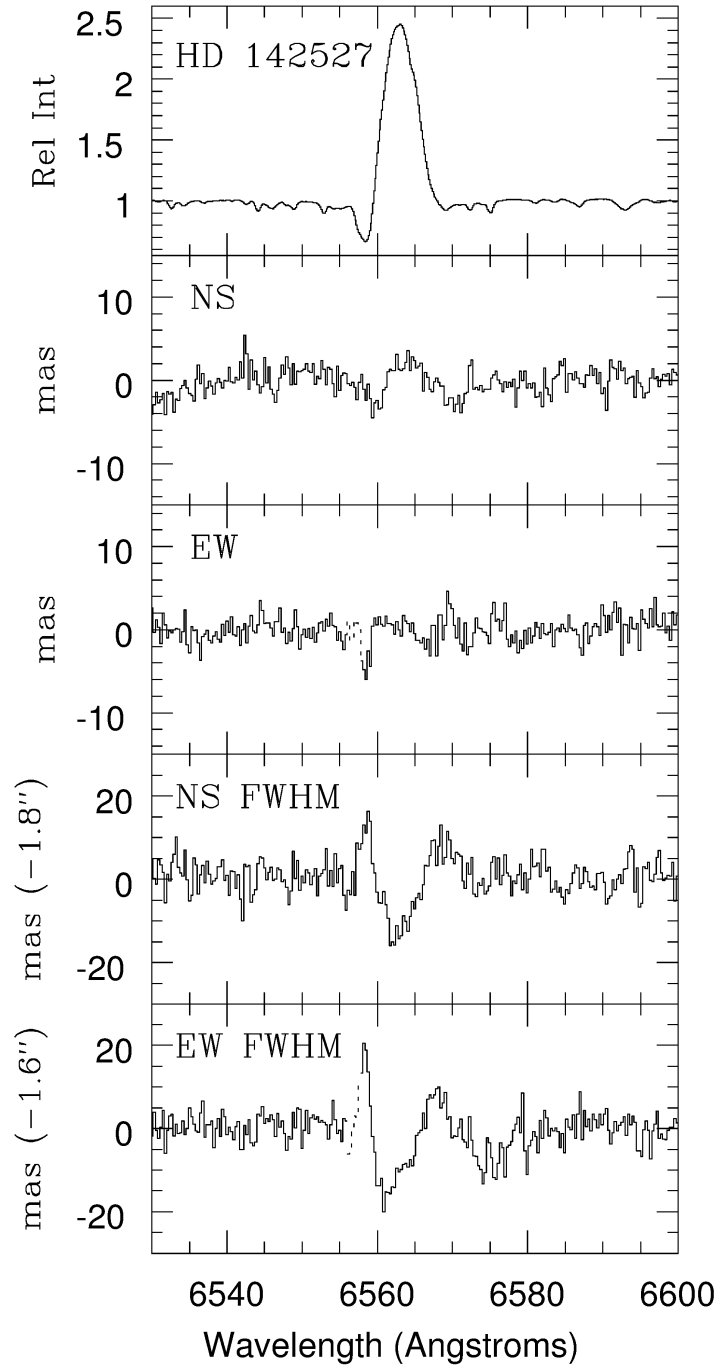
FIGURE 5.8: Spectro-astrometric analysis of the Hα emission of HD 142527 from Baines et al. (2006). The north-south and east-west results are produced by subtracting the anti-parallel PAs, and the FWHM and centroid zero-points have been adjusted to represent the continuum position.

average $L_{H\alpha}$ for HD 142527, the luminosity ratio is approximately 1.3×10^{-3} $L_\odot$. At a distance of 157.3 pc, the separation between parent and companion is ~ 76 mas. As

Epoch	Flux (erg/s/cm^2/Å)	$\mathbf{L}_{line}$ ($\mathbf{L}_\odot$)	$\mathbf{L}_{acc}$($\mathbf{L}_\odot$)	$\mathbf{Log(M}_{acc})[\mathbf{M}_\odot \ \mathbf{yr}^{-1}]$
Obs 1	6.63×10^{-11}	0.0511	1.91	-7.02
Obs 2	7.32×10^{-11}	0.0565	2.14	-6.97
Obs 3	6.61×10^{-11}	0.0509	1.90	-7.02

TABLE 5.2: Fluxes values, line and accretion luminosities and mass accretion rates for each of the 3 observations. The fluxes are extinction corrected and the parameters of Equation 4.3 are taken from Alcala et al. (2017) for consistency with T Cha (the Mass of HD 142527 also puts it on the border between TTS and Herbig Ae/Be stars).

before, the size of the offset measured using SA is the separation distance multiplied by the ratio of the strength of the Hα signal from the two stars. This gives an offset of 0.01 mas, indicating that it should not be possible to resolve the two stars when both are in emission. A reason for seeing signals at the wings of the emission profile in the spectro-astrometric figures is that the main star has a line profile which is much more intense, as given by the ratio calculated above, but narrower than its companion. Hence the signals are only seen in the wings, where the companions emission is not dominated by the parent star.

5.5 Discussion & Conclusion

The results presented here for both spectro-astrometric analysis and $\dot{M}_{acc}$ calculation agree well with previous works on HD 142527 and HD 142527B. They can be summarised as follows:

1. From the spectrum shown in Figure 5.1, one of the most interesting features is in the lack of emission profiles across lines where they would be expected. Even with the larger wavelength range afforded at this time, there were no more lines in emission than seen for T Cha. While there is a small emission peak for the [O I]λ 6300 line, there is no HVC component present. Both He I and NaD lines are present but only the Hα line is relevant to the spectro-astrometric analysis.

2. The agreement between the $\dot{M}_{acc}$ calculated in this work, for both HD 142527 and its companion, with values from previous studies acting as a validation for the methodology applied to both stars. While there are a large number of parameter values calculated for a and b in Equation 4.3, each of the calculated $\dot{M}_{acc}$ values lie within 1 order of magnitude of each other. For our results we have used the same values as used for T Cha (0.59 ± 0.04 and -4.13 ± 0.11 respectively), and the value of 1×10^{-7} M$_\odot$ yr^{-1} is in good agreement with most of the previous calculations (eg. Close et al. (2014) calculated a value of 7×10^{-8} M$_\odot$ yr^{-1} while Mendigutía et al. (2014) calculated a value of 1.3×10^{-7} M$_\odot$ yr^{-1}).

3. The SA analysis applied to the Hα line shows a centroid offset at + 200 km s^{-1}. The lack of orthogonal and/or anti-parallel PAs in this observation run prevent corroboration via PA subtraction, but it is clear that a signal is present in both the centroid and FWHM. The same signals are further highlighted when continuum subtraction is applied, and another signal is seen at - 200 km s^{-1} which was previously covered up by the continuum. This combination of both a centroid and FWHM displacement in the same position as seen in Baines et al. (2006) is enough evidence to acknowledge the detection of HD 142527B via SA, indicating the efficacy of this technique at detecting VLM stars.

It was shown that the spectro-astrometric offset is expected to be 0.01 mas when both stars are in full emission, which is 100 times smaller than the 1σ value of the binned results. This helps explain why a signal is only seen in Figure 5.7 at the wings of the Hα line profile, when the ratio of strengths is closer than at the central Hα wavelength. For mass accretion calculations, the fact that HD 142527 has a mass on the border between TTS and Herbig Ae/Be star allowed for the same relationship for T Cha to be used. We also used values for Herbig Ae/Be stars calculated by Mendigutía et al. (2011), and derived an average $\log(\dot{M}_{acc})$ of -6.4 M$_\odot$ yr^{-1}. This value is slightly higher than the value found by Mendigutía et al. (2014), indicating some variability in the star, as well as the new stellar parameters courtesy of Gaia DR2. The signals presented in both normal and continuum-subtracted results indicate spectro-astrometry does indeed have the capability of resolving Very Low-Mass (VLM) companions from their parents.

Chapter 6

Overall Conclusions and Future Work

As current exoplanet detection techniques become more efficient, the next step in completing the picture of how planets evolve becomes the detection of planets still in the process of forming. This introduces many complications for current techniques such as the intrinsic instability of YSOs and the difficulty of detecting an object still within a circumstellar disk. The disk itself can emit enough light to change the SED of its parent star and allow classification as a Class II PMS star. Gaps in the disk then affect the SED in such a way that we have the classification of TD objects, and these offer the best chance to detect an exoplanet in formation that is not completely hidden by the circumstellar environment. Direct imaging is currently the only technique that would allow detection of a planet in formation around a star, but it is most effective for wide-separation planets undergoing a large amount of accretion.

The aim of this project was first to investigate the use of SA in exoplanet detection around TTS, as in Whelan et al. (2015). It was determined that the spectro-astrometric offset was too small to be detected for T Cha and its hypothetical exoplanet, T Cha b. SA was then applied to HD 142527 with the aim of detecting a signal from its known VLM companion, HD 142527B, which was successful.

6.1   Mass accretion

One way in which an exoplanet can be resolved from its parent star is by focusing the search on tracers by which accretion can be detected. Accretion takes place both for the exoplanets and stars around which they orbit, inferred by the clearing of gaps that

define TD objects. This often occurs to a much larger degree than the ratio of masses between the objects themselves. Hα is often used as such an accretion tracer, and has been seen for a number of VLM stars and planetary mass objects (Close et al. 2014; Joergens et al. 2013; Sallum et al. 2015; Zhou et al. 2014).

Our work in Chapter 4 on the use of the [OI]λ 6300 line show that (at least for highly variable stars such as T Cha) it can offer a more stable measure of the $\dot{M}_{acc}$. In the study of T Cha by Schisano et al. (2009), it was determined that the variation in Hα line profile is a result of episodic accretion caused by clumps of gas and dust. The highly variable line profiles in Figure 4.9 illustrate how it is not always possible to use the Hα width at 10% intensity formula, and we found good agreement between the $\dot{M}_{acc}$ determined from the [O I]λ 6300 line (6.3×10^{-9} M$_\odot$ yr^{-1}) and previous results (4×10^{-9} M$_\odot$ yr^{-1} from Schisano et al. (2009)). The [O I]λ 6300 emission stems from a solar wind, which would not be blocked by the clumps of dust or gas close to the star, and so for systems with a significant amount of occultation, the [O I]λ 6300 line should be considered as an alternative method of $\dot{M}_{acc}$ calculation. HD 142527 does not show any major [O I]λ 6300 emission, with no HVC and only a very small LVC. For this reason Hα was used in the calculation of its $\dot{M}_{acc}$, and again good agreement was found with previous works, with our value of 1×10^{-7} M$_\odot$ yr^{-1} lying within one order of magnitude of both Close et al. (2014), who calculated a value of 7×10^{-8} M$_\odot$ yr^{-1} and Mendigutía et al. (2014), who calculated a value of 1.3×10^{-7} M$_\odot$ yr^{-1}).

6.2 Spectro-astrometry as a detection technique for exoplanets

SA has long been used as a technique for resolving close-binary star systems (Bailey 1998a; Baines et al. 2006; Takami et al. 2003). Following its success, the technique saw use in investigating stellar phenomena such as outflows and jets, as well as probing the circumstellar environment of YSOs (Blanco Cárdenas et al. 2014; Stern et al. 2015; Whelan et al. 2014b, 2015, 2006).

The two main conclusions drawn from the spectro-astrometric analysis performed in this project are as follows:
Firstly, Results for T Cha suggest that it would be difficult to routinely use SA to detect planets around TDs. The expected SA signal offset of around 0.1 mas for a 1 M$_{Jup}$ planet is smaller than can be achieved, even with binning to the highest factor of 40, resulting in the 0.5 mas accuracy achieved in this project. Applying this technique to systems with a parent star of lower mass than T Cha may increase the chances of

detection, by decreasing the ratio of Hα luminosities and so providing a larger spectro-astrometric offset. While no signal was detected for T Cha, we can still use the results from SA to place limits on the $\dot{M}_{acc}$ from the planet, as was done for LkCa 15b in Whelan et al. (2015), with an upper limit of 7.9×10^{-10} M$_\odot$ yr^{-1} being calculated in this project.

Secondly, we have determined that SA is capable of resolving VLM stars at close separation from the parent when the ratio of masses is $\geq$ 1:15. The detection of signals in both the centroid and FWHM of HD 142527 (in the same position as detected in Baines et al. (2006)) after continuum subtraction provide sufficient evidence to label it a success. The detection of the signals only at the wings of the Hα ELR is interesting, and gives evidence of two stars with differing Hα ELR widths. Further modelling of the effect of two line profiles with different widths would be needed to fully understand the expected offsets that should be seen in this situation.

The two main elements determining the expected SA offset (apart from telescopic factors) are distance and $L_{H\alpha}$ ratio. It is interesting to see that our calculations for T Cha b put its average $L_{H\alpha}$ of 3×10^{-5} L$_\odot$. This is only half the value calculated by the same method for HD 142527B, which was 6.8×10^{-5} L$_\odot$. This shows that despite T Cha b being $\sim$ 100 times smaller, it has a $\dot{M}_{acc}$ which is similar, possibly indicating a much broader association between mass and $\dot{M}_{acc}$ than is present for TTS, as shown in Figure 4.19. Future work in this area may yield a new model for the ratio of log($\dot{M}_{acc}$) vs log(M$_\odot$).

6.3   Final thoughts

Spectro-astrometry certainly excels at probing stellar phenomena, circumstellar environments and resolving close binaries, even being used to prove that brown dwarfs also emit stellar outflows (Whelan et al. 2006). Being able to probe the circumstellar environment while also looking for exoplanets or low-mass companions makes this technique very efficient at gathering stellar information, with the only condition being the need for observations with the four PAs for signal confirmation. For this case, observations from a more stable instrument are needed to resolve the small SA offset between an exoplanet and its parent. Despite the non-detection for T Cha, the discovery of a signal from a VLM star gives hope towards being able to use SA for exoplanet detection. Observations using modern AO, such as the system being developed for the ELT, can increase the resolution at which objects could theoretically be detected, lowering the noise that is present in the results from Chapter 4 and 5. While the technique itself removes the need for extreme spatial resolution, a reduction in spatial noise

via AO would reduces the standard deviation of the centroid profile, allowing smaller offsets to be detected. Future spectro-astrometric observations using AO may yield detections, and this is something worth investigating further, as it would allow older ground-based spectrographs that have been fitted with AO to participate in the hunt for exoplanets during formation. Another situation in which SA could prove viable is the search for exoplanets in formation around brown dwarfs. Regardless, further spectro-astrometric studies from ground-based telescopes are necessary to determine its capacity as an exoplanet technique.

Appendix A

Python program example

```python
## SA_example_script.py
## This program shows the type of scripts used to calculate the centroid and
## FWHM values used in this thesis. It will take any reduced 2d spectrum and
   output the results to a graph centered on the H alpha emission line
   wavelength.

import os     # Import os for filesave functionality
import numpy as np     # Import NumPy for array manipulation
from astropy.io import fits     # Import AstroPy for .fits file analysis
import matplotlib.pyplot as plt     # Imported for plotting
from matplotlib.ticker import AutoMinorLocator     # Auto locate ticker values
from lmfit.models import PseudoVoigtModel     # Import the PSF model for
   fitting
import pandas as pd     # Import Pandas for binning section

## Reads in the file name
filename = raw_input("Please enter the name of the fits file to be plotted: ")

## Determines the emission line under analysis, for velocity calculations
## In this example, it is H alpha.
wavecal = 6562.8


############################## File 1 ##################################


header_data1 = fits.getheader(filename, 0)     # Imports the header data into
   python
```

```python
## The following if else statement determines whether the spectrum is
    vertical or horizontal
if header_data1['NAXIS1'] > header_data1['NAXIS2']:
image_data1a = fits.getdata(filename, ext = 0)
image_data1b = np.transpose(image_data1a)
xpix1 = header_data1['CDELT1']    # Import the spectral increment
ypix1 = header_data1['CDELT2']    # Import the spatial increment
x1 = np.asarray(range(header_data1['NAXIS1']))    # create an array for the
    x-axis
y1 = np.asarray(range(header_data1['NAXIS2']))    # Create an array for the
    y-axis
increment1 = header_data1['CRVAL1'] + (abs(header_data1['CRPIX1']) * xpix1) +
    (x1 * xpix1)    # Create an array to be wavelegnth calibrated


else:
image_data1b = fits.getdata(filename, ext = 0)
image_data1a = np.transpose(image_data1b)
xpix1 = header_data1['CDELT2']
ypix1 = header_data1['CDELT1']
x1=np.asarray(range(header_data1['NAXIS2']))
y1=np.asarray(range(header_data1['NAXIS1']))
increment1=header_data1['CRVAL2'] + (abs(header_data1['CRPIX2']) * xpix1) +
    (x1 * xpix1)


## Determines the central aperture for fitting purposes
central_ap = int(len(y1) / 2)



## Centroid and FWHM calculation using the Pseudo Voigt function from lmfit
## The while loop iterates through the spectral axis
i = 0
centroid1 = []
fwhm1 = []
while i < len(image_data1b):
mod = PseudoVoigtModel()
pars1 = mod.guess(image_data1b[i], x = y1)    # Initial guess parameters
out1  = mod.fit(image_data1b[i], pars1, x = y1)    # Array for output values
fwhm1.append(out1.params['fwhm'].value)    # Append FWHM to list
centroid1.append(out1.params['center'].value)    # Append centroid to list
i += 1    # iteration


## Normalization of the flux line profile
```

```python
norm1a = np.asarray(image_data1a[central_ap+1])
norm1b = norm1a[1:1600]     # Need to normalise away from actual emission line
norm1c = (sum(norm1b) / len(norm1b))
norm1d = norm1a / norm1c


## Velocity calibration
lightspeed = 299792.458
velocity1 = (((increment1 - wavecal)/wavecal) * lightspeed)


## remove telescopic curvature, convert from pixel to arcseconds via 0.182
    and convert to milliarcseconds. therefore multiply by 180.
cenmas1a = (centroid1 - np.poly1d(np.polyfit(increment1, centroid1,
    20))(increment1)) * 182


## Convert FWHM values from pixel space to arcseconds
fwhm_arc1 = np.asarray(fwhm1) * 0.182


###### Binning Section ######
fluxbin = 1
cenbin = 1
fwhmbin = 1


fluxbin1 = pd.rolling_mean(norm1d, fluxbin)
cenbin1 = pd.rolling_mean(cenmas1a, cenbin)
fwhmbin1 = pd.rolling_mean(fwhm_arc1, fwhmbin)


##### Error Calcs #####
sig1a = np.asarray(cenbin1[cenbin:1250])

sigma1 = np.std(sig1a)     # Calculates the standard deviation of the centroid
    function
plotsig1 = np.full((len(cenbin1), 1), sigma1)     # extend std dev into an
    array for plotting
plotsigval1 = str(plotsig1[0])
Error1 = round(plotsig1[0], 2)     # Round off std dev for aesthetics
Error1a = str(Error1)     # Convert std dev to string for plot label




######################     Plotting section     ###########################
######################         FLUX             ###########################


fig = plt.figure(figsize = (8, 10))
```

```python
ax1a = fig.add_subplot(3,1,1)
plt.plot(velocity1, fluxbin1, c = 'k', label = filename)
plt.ylabel('Normalized Flux', fontsize = 18)
plt.xlim([-500, 500])
plt.legend(fontsize = 14, loc=1, ncol=2)
ax1a.tick_params(axis = 'both', direction = 'in', which = 'both', labelsize =
    14, length = 5, width = 2, right = True, top = True)
minorLocator1ax = AutoMinorLocator()
minorLocator1ay = AutoMinorLocator()
ax1a.xaxis.set_minor_locator(minorLocator1ax)
ax1a.yaxis.set_minor_locator(minorLocator1ay)
ax1a.tick_params(axis = 'both', which = 'minor', length = 3, width = 1.5)


###################### CENTROID ###########################

ax1b = plt.subplot(3,1,2)
plt.plot(velocity1, cenbin1, c = 'k')
plt.plot(velocity1, plotsig1, linestyle = '--', c='k', label = r'$\sigma$ ' +
    Error1a + ' mas')
plt.plot(velocity1, plotsig1 * -1, linestyle = '--', c = 'k')  # 1 sigma
plt.plot(velocity1, plotsig1 * 3, linestyle = '--', c = 'grey')
plt.plot(velocity1, plotsig1 * -3, linestyle = '--', c = 'grey')  #  3 sigma
plt.ylabel('Centroid (mas)', fontsize = 18)
plt.legend(fontsize = 14, loc = 1, ncol = 2)
plt.xlim([-500, 500])
ax1b.tick_params(axis = 'both', direction = 'in', which = 'both', labelsize =
    14, length = 5, width = 2, right = True, top = True)
minorLocator1bx = AutoMinorLocator()
minorLocator1by = AutoMinorLocator()
ax1b.xaxis.set_minor_locator(minorLocator1bx)
ax1b.yaxis.set_minor_locator(minorLocator1by)
ax1b.tick_params(axis = 'both', which = 'minor', length = 3, width = 1.5)


###################### FWHM ###########################

ax1c = plt.subplot(3,1,3)
plt.plot(velocity1, fwhmbin1, c = 'k')
plt.ylabel('FWHM (arcsec)', fontsize = 18)
plt.xlabel('Velocity (km s$^{-1}$)', fontsize = 18)
plt.xlim([-500, 500])
ax1c.tick_params(axis = 'both', direction = 'in', which = 'both', labelsize =
    14, length = 5, width = 2, right = True, top = True)
minorLocator1cx = AutoMinorLocator()
```

```python
minorLocator1cy = AutoMinorLocator()
ax1c.xaxis.set_minor_locator(minorLocator1cx)
ax1c.yaxis.set_minor_locator(minorLocator1cy)
ax1c.tick_params(axis = 'both', which = 'minor', length = 3, width = 1.5)
plt.grid(b = False)

## The following section is for graph visualization, adjusting subplots and
    graph axes.

plt.subplots_adjust(top = 0.96, bottom = 0.08, left = 0.12, right = 0.97,
    hspace = 0.16, wspace = 0.22)
for axis in ['top','bottom','left','right']:
ax1a.spines[axis].set_linewidth(1.5)
ax1a.spines[axis].set_color('k')
ax1b.spines[axis].set_linewidth(1.5)
ax1b.spines[axis].set_color('k')
ax1c.spines[axis].set_linewidth(1.5)
ax1c.spines[axis].set_color('k')

plt.show()

## Check to see if file is already present. Itf it is this section will
    delete it, and if not, saves it.
output_file = filename + '.pdf'

try: os.remove(output_file)
except: pass

plt.savefig(filename+".pdf", dpi = 500)

################################################################################
############################### End of program #############################
################################################################################
```

Bibliography

Alcala, J. M., Manara, C. F., Natta, A., et al. 2017, Astronomy & Astrophysics, 600, A20

Alcalá, J. M., Natta, A., Manara, C. F., et al. 2014, Astronomy & Astrophysics, 561, A2

Alencar, S. H. P. & Basri, G. 2000, The Astronomical Journal, 119, 1881

ALMA-Partnership, Brogan, C. L., Perez, L. M., et al. 2015 [[arXiv]1503.02649]

Andre, P. & Montmerle, T. 1994, The Astrophysical Journal, 420, 837

Andrews, S. M., Wilner, D. J., Zhu, Z., et al. 2016, The Astrophysical Journal Letters, Volume 820, Issue 2, article id. L40, 5 pp. (2016)., 820 [[arXiv]1603.09352]

Bailey, J. A. 1998a, Monthly Notices of the Royal Astronomical Society, 301, 161

Bailey, J. A. 1998bin , 932–939

Baines, D., Oudmaijer, R. D., Porter, J. M., & Pozzo, M. 2006, Mon. Not. R. Astron. Soc, 367, 737

Beckers, J. M. 1982, Optica Acta, 29, 361

Bergin, E. A. & Williams, J. P. 2018, The determination of protoplanetary disk masses, Tech. rep.

Beuther, H., Klessen, R. S., Dullemond, C. P., & Henning, T. 1985 (University of Arizona Press), 1

Biller, B., Lacour, S., Juhász, A., et al. 2012, Astrophysical Journal Letters, 753 [[arXiv]{1206.2654}]

Blanco Cárdenas, M. W., Käufl, H. U., Guerrero, M. A., Miranda, L. F., & Seifahrt, A. 2014, Astronomy & Astrophysics, 566, A133

Brannigan, E., Takami, M., Chrysostomou, A., & Bailey, J. 2005, Monthly Notices of the Royal Astronomical Society, 367, 315

Brittain, S. D., Najita, J. R., & Carr, J. S. 2015, American Astronomical Society, AAS Meeting #225, id.349.14, 225

Brittain, S. D., Rettig, T. W., Simon, T., et al. 2003, The Astrophysical Journal, 588, 535

Brown, L. R., Troutman, M. R., & Gibb, E. L. 2013, Astrophysical Journal Letters, 770, L14

Chauvin, G., Lagrange, A.-M., Dumas, C., et al. 2004, Astronomy & Astrophysics, 425, L29

Cheetham, A., Huélamo, N., Lacour, S., De Gregorio-Monsalvo, I., & Tuthill, P. 2015, Monthly Notices of the Royal Astronomical Society: Letters, 450, L1

Clausius, R. 1870, Paris : Gauthier-Villars, 1870; XIV, 141 p. ; in 8.; DCCC.4.398

Close, L. M., Follette, K. B., Males, J. R., et al. 2014, Astrophysical Journal Letters, 781, L30

Collins, G. W. 1978, ... Pachart Publishing House(Astronomy and Astrophysics ...

Covino, E., Alcala, J. M., Allain, S., et al. 1997, Astronomy and Astrophysics, v.328, p.187-202 (1997), 328, 187

Davis, C. J., Ray, T. P., Desroches, L., & Aspin, C. 2001, Monthly Notices of the Royal Astronomical Society, 326, 524

Davis, C. J., Whelan, E., Ray, T. P., & Chrysostomou, A. 2003, Astronomy & Astrophysics, 397, 693

Dekker, H., D'Odorico, S., Kaufer, A., Delabre, B., & Kotzlowski, H. 2000, in Proc. SPIE Vol. 4008, p. 534-545, Optical and IR Telescope Instrumentation and Detectors, Masanori Iye; Alan F. Moorwood; Eds., ed. M. Iye & A. F. M. Moorwood, Vol. 4008, 534

Ercolano, B. 2014, Astronomische Nachrichten, 335, 549

Ercolano, B. & Pascucci, I. 2017, Royal Society Open Science, 4, 170114

Espaillat, C., Muzerolle, J., Najita, J., et al. 2014, Protostars and Planets VI, Henrik Beuther, Ralf S. Klessen, Cornelis P. Dullemond, and Thomas Henning (eds.), University of Arizona Press, Tucson, 914 pp., p.497-520, 497

Fang, M., Boekel, R. V., Wang, W., Carmona, A., & Henning, T. 2009, Astronomy, 489, 461

Gaia-Collaboration, Mignard, F., Klioner, S. A., et al. 2018, Astronomy & Astrophysics, 616, A14

Garcia, P., Thiébaut, E., & Bacon, R. 2000, IAU Symposium, 346, 74P

Gnerucci, A., Marconi, A., Capetti, A., Axon, D. J., & Robinson, A. 2010, Astronomy and Astrophysics, 511, A19

Gullbring, E., Hartmann, L., Briceno, C., & Calvet, N. 1998, The Astrophysical Journal, 492, 323

Hartmann, L., Herczeg, G., & Calvet, N. 2016, Annual Review of Astronomy and Astrophysics, 54, 135

Hayashi, C. 1961, \Pasj, 13, 450

Hendler, N. P., Pinilla, P., Pascucci, I., et al. 2018, Monthly Notices of the Royal Astronomical Society: Letters, 475, L62

Henyey, L. G., Lelevier, R., & Levée, R. D. 1955, Publications of the Astronomical Society of the Pacific, 67, 154

Herczeg, G. J., Brown, J. M., van Dishoeck, E. F., & Pontoppidan, K. M. 2011, Astronomy & Astrophysics, Volume 533, id.A112, 26 pp., 533 [[arXiv]1106.5391]

Horne, K. 1986, Publications of the Astronomical Society of the Pacific, 98, 609

Huelamo, N., de Gregorio-Monsalvo, I., Macias, E., et al. 2015, aanda.org [[arXiv]1501.06483]

Huelamo, N., Lacour, S., Tuthill, P., et al. 2011, Astronomy & Astrophysics, 528, L7

Ida, S. & Nakazawa, K. 1989, 22. Symposium on Celestial Mechanics, p. 96 - 101, 96

Jayawardhana, R., Mohanty, S., & Basri, G. 2003, The Astrophysical Journal, Volume 592, Issue 1, pp. 282-287., 592, 282

Jeans, J. H. 1902, Philosophical Transactions of the Royal Society A: Mathematical, Physical and Engineering Sciences, 199, 1

Joergens, V., Bonnefoy, M., Liu, Y., et al. 2013, Astronomy & Astrophysics, 558, L7

Johansen, A., Blum, J., Tanaka, H., et al. 2014, Protostars and Planets VI, Henrik Beuther, Ralf S. Klessen, Cornelis P. Dullemond, and Thomas Henning (eds.), University of Arizona Press, Tucson, 914 pp., p.547-570, 547

Keppler, M., Benisty, M., Müller, A., et al. 2018, eprint arXiv:1806.11568 [[arXiv]1806.11568]

Kraus, A. L. & Ireland, M. J. 2012, Astrophysical Journal, 745, 5

Lacour, S., Biller, B., Cheetham, A., et al. 2016, Astronomy & Astrophysics, 590, A90

Lada, C. J. 1987, Star formation - From OB associations to protostars, Vol. 115 (Cambridge University Press), 1–17

Lissauer, J. J. 1993, Annual Review of Astronomy and Astrophysics, 31, 129

Manara, C. F., Fedele, D., Herczeg, G. J., & Teixeira, P. 2016, a&a, ?, ?

Manara, C. F., Rigliaco, E., Natta, A., et al. 2012, Astronomy & Astrophysics, 548, A56

Manara, C. F., Testi, L., Natta, A., et al. 2014, Astronomy & Astrophysics, 568, A18

Marsh, T. R. 1989, Publications of the Astronomical Society of the Pacific, 101, 1032

Mayor, M. & Queloz, D. 1995, Nature, 378, 355

Mendigutía, I., Calvet, N., Montesinos, B., et al. 2011, Astronomy & Astrophysics, 535, A99

Mendigutía, I., Fairlamb, J., Montesinos, B., et al. 2014, Astrophysical Journal, 790, 21

Mohanty, S., Basri, G., & Jayawardhana, R. 2005, Astronomische Nachrichten, 326, 891

Mouschovias, T. C. 1989, in The Physics and Chemistry of Interstellar Molecular Clouds: mm and Sub-mm Observations in Astrophysics (Berlin, Heidelberg: Springer Berlin Heidelberg), 297–312

Mukai, K. 1990, Publications of the Astronomical Society of the Pacific, 102, 183

Muzerolle, J., Hillenbrand, L., Calvet, N., Briceno, C., & Hartmann, L. 2003, The Astrophysical Journal, 592, 266

Natta, A., Testi, L., Muzerolle, J., et al. 2004, Astronomy and Astrophysics, 424, 603

Nisini, B., Antoniucci, S., Alcala', J. M., et al. 2017, Astronomy & Astrophysics, 609, A87

Nordstrom, B., Mayor, M., Andersen, J., et al. 2004, Astronomy & Astrophysics, 418, 989

Olivero, J. J. & Longbothum, R. L. 1977, Journal of Quantitative Spectroscopy and Radiative Transfer, 17, 233

Olofsson, J., Benisty, M., Le Bouquin, J.-B., et al. 2013, Astronomy & Astrophysics, 552, A4

Palca, J. 2013, For Sharpest Views, Scope The Sky With Quick-Change Mirrors

Palla, F. & Francesco. 2012, in FIRST STARS IV - FROM HAYASHI TO THE FU-TURE -. AIP Conference Proceedings, Volume 1480, pp. 22-29 (2012)., Vol. 1480, 22–29

Palmeirim, P., André, P., Kirk, J., et al. 2013, Astronomy & Astrophysics, 550, A38

Pascucci, I. & Sterzik, M. 2009, Astrophysical Journal, 702, 724

Pérez, L. M., Carpenter, J. M., Andrews, S. M., et al. 2016, Science, 353, 1519

Pohl, A., Sissa, E., Langlois, M., et al. 2017, Astronomy & Astrophysics, 605, A34

Pontoppidan, K. M., Blake, G. A., & Smette, A. 2011, Astrophysical Journal, 733, 84

Pontoppidan, K. M., Blake, G. A., van Dishoeck, E. F., et al. 2008, The Astrophysical Journal, 684, 1323

Rigliaco, E., Natta, A., Randich, S., et al. 2010, Astronomy & Astrophysics, 526, L6

Rigliaco, E., Natta, A., Testi, L., et al. 2012, Astronomy & Astrophysics, 548, A56

Sallum, S., Follette, K. B., Eisner, J. A., et al. 2015, Nature, 527, 342

Salyk, C., Blake, G. A., Boogert, A. C. A., & Brown, J. M. 2007, MOLECULAR GAS IN THE INNER 1 AU OF THE TW HYA AND GM AUR TRANSITIONAL DISKS, Tech. rep.

Santamaría-Miranda, A., Cáceres, C., Schreiber, M. R., et al. 2017, Monthly Notices of the Royal Astronomical Society, Volume 475, Issue 3, p.2994-3003, 475, 2994

Schisano, E., Covino, E., Alcalá, J. M., et al. 2009, Astronomy & Astrophysics, 501, 1013

Schmidt, T. O. B., Neuhäuser, R., Seifahrt, A., et al. 2008, Astronomy and Astrophysics, 491, 311

Shu, F. H., Adams, F. C., & Lizano, S. 1987, Annual Review of Astronomy and Astrophysics, 25, 23

Simon, M. N., Pascucci, I., Edwards, S., et al. 2016, The Astrophysical Journal, 831, 169

Stern, J., Hennawi, J. F., & Pott, J. U. 2015, Astrophysical Journal, 804, 57

Strom, K. M., Strom, S. E., Edwards, S., Cabrit, S., & Skrutskie, M. F. 1989, The Astronomical Journal, 97, 1451

Strom, S. E., Edwards, S., & Skrutskie, M. F. 1993, Protostars and Planets III, 837

Takami, M., Bailey, J., & Chrysostomou, A. 2003, Astronomy & Astrophysics, 397, 675

Takami, M., Bailey, J., Gledhill, T. M., Chrysostomou, A., & Hough, J. H. 2001, Monthly Notices of the Royal Astronomical Society, 323, 177

Torres, C. A. O., Quast, G. R., Melo, C. H. F., & Sterzik, M. F. 2008, in Handbook of Star Forming Regions, Volume II, ed. B. Reipurth, 757

Uyama, T., Tanigawa, T., Hashimoto, J., et al. 2017 [[arXiv]1707.06337]

van der Laan, H.; Perola, G. C. 1969, Astronomy and Astrophysics, 3, 468

van der Plas, G., van den Ancker, M. E., Fedele, D., et al. 2008, Astronomy and Astrophysics, 485, 487

Verhoeff, A. P., Min, M., Pantin, E., et al. 2011, Astronomy & Astrophysics, 528, A91

Vorobyov, E. I. & Basu, S. 2010, Proceedings of the International Astronomical Union, 6, 463

Ward-Thompson, D. & Whitworth, A. 2011, in An Introduction to Star Formation (Cambridge University Press), 65–94

Whelan, E. & Garcia, P. 2008, in Lecture Notes in Physics, Vol. 742 (Berlin, Heidelberg: Springer Berlin Heidelberg), 123–149

Whelan, E. T. 2014, Astronomische Nachrichten, 335, 537

Whelan, E. T., Alcalá, J. M., Bacciotti, F., et al. 2014a, Astronomy & Astrophysics, 570, A59

Whelan, E. T., Bonito, R., Antoniucci, S., et al. 2014b, Astronomy & Astrophysics, 565, A80

Whelan, E. T., Huelamo, N., Alcala, J. M., et al. 2015 [[arXiv]1504.04824]

Whelan, E. T., Ray, T. P., Bacciotti, F., & Jayawardhana, R. 2006, New Astronomy Reviews, 49, 582

Whelan, E. T., Ray, T. P., & Davis, C. J. 2004, Astronomy and Astrophysics, 417, 247

Winn, J. N. 2010, Exoplanets, ed. S. Seager (University of Arizona Press), 526

Wu, Y.-L., Close, L. M., Males, J. R., et al. 2015, The Astrophysical Journal, Volume 801, Issue 1, article id. 4, 6 pp. (2015)., 801 [[arXiv]1501.01396]

Xu, W.-w., hao Liao, X., hong Zhou, Y., & qing Xu, X. 2017, Chinese Astronomy and Astrophysics, 41, 381

Zhou, Y., Herczeg, G. J., Kraus, A. L., Metchev, S., & Cruz, K. L. 2014, Astrophysical Journal Letters, 783, L17

Zhu, Z. 2015, Astrophysical Journal, 799, 16